
Single-cycle Mid-infrared Pulse Generation via Nonlinear Optics

Bo-Han Chen



München 2019

Single-cycle Mid-infrared Pulse Generation via Nonlinear Optics

Bo-Han Chen

Dissertation
an der Fakultät für Physik
der Ludwig-Maximilians-Universität
München

vorgelegt von
Bo-Han Chen
aus Taichung city, Taiwan

München, den 22.10.2019

Erstgutachter: Prof. Dr. Ferenc Krausz

Zweitgutachter: Prof. Dr. Thomas Udem

Tag der mündlichen Prüfung: 13.12.2019

獻給一路走來幫助過我的所有人

Zusammenfassung

Physikalische und chemische Prozesse, die elektronische oder molekulare Dynamik beinhalten, bestimmen so ziemlich die Welt, die wir jeden Tag wahrnehmen. Diese ultraschnellen Bewegungen können entweder indirekt durch Spektroskopie gemessen oder direkt durch ultraschnelle Elektronenbeugung und Mikroskopie beobachtet oder sichtbar gemacht werden. Die Spektroskopie erfordert ein breitbandiges Mittelinfrarotspektrum. Von besonderem Interesse sind Frequenzen, die den Bereich des molekularen Fingerabdrucks ($2 \mu\text{m} - 20 \mu\text{m}$) abdecken, da sie mit vielen Schwingungsmoden der Grundmoleküle zusammenfallen. Ultraschnelle Elektronenbeugung und Mikroskopie erfordern kurze Elektronenimpulse mit einer Dauer im Bereich von Femtosekunden (10^{-15} s) oder sogar Attosekunden (10^{-18} s), μm Subzyklen-Zeitauflösung und atomare räumliche Auflösung gleichzeitig zu gewährleisten. Solche Elektronenimpulse können unter Verwendung der Technik der rein optischen Impulskompression erzeugt werden, die intensive Einzelzyklus-Terahertz- oder Mittelinfrarotimpulse erfordert. Daher werden Hochleistungsimpulse, Einzelzyklusimpulse und phasenstabile Mittelinfrarotimpulse sehr geschätzt.

Diese Arbeit zielt darauf ab, die gewünschten Impulse im mittleren Infrarot durch optisch parametrische Abwärtskonvertierung zu erzeugen. Erstens wird ein hybrides Schema zur spektralen Verbreiterung mittels massiver Fasern verwendet, um ultrakurze Impulse für die spätere Verwendung bei der Erzeugung von Intra-Impuls-Differenzfrequenzen (IPDFG) vorzubereiten. Ein Kompressionsfaktor von 33 wird erreicht und 30-fs-Impulse werden aus 1-ps-Impulsen mit einer durchschnittlichen Leistung von 4 W erzeugt.

Als Nächstes wird IPDFG mit den 30-fs-Ansteuerimpulsen in einem LiGaS₂ (LGS)-Kristall ausgeführt. Sorgfältig gesteuerte Eingangspolarisation führt zu einer effizienten

Erzeugung unter den Bedingungen der Phasenanpassung (Typ II). Inzwischen ist der Erzeugungsmechanismus durch Charakterisierung der Impulsform und des Spektrums der Treiberimpulse nach dem nichtlinearen Kristall gut verstanden. Das Gleichgewicht zwischen der spektraler Verbreiterung, der Dispersion und dem fortschreitenden Verlust des zeitlichen Überlapps der Impulse ist entscheidend für eine effiziente nichtlineare Frequenzumwandlung in einem dicken Kristall. Aus einem 4-mm-LGS-Kristall wird eine Strahlung im mittleren Infrarotbereich von 8–11 μm mit einer Impulsenergie von ~ 7 nJ erhalten.

Um die Leistung der Mittelinfrarotimpulse weiter zu verbessern, wird eine Inter-Impuls-Differenzfrequenz-Erzeugung (DFG) mit einem nicht-kollinearen optisch parametrischen Verstärkersystem (NOPA) verwendet. Durch gezielte Beeinflussung der Dispersion der Keimimpulse wird durch reine Festkörpermaterialien eine Impulskompression im mittleren Infrarotbereich möglich. Diese Anordnungen erlauben die Erzeugung von 1,4-Zyklus-Impulsen im mittleren Infrarot mit 7,5 μm Zentralwellenlänge und einer Impulsenergie von 220 nJ. Die Träger- Einhüllenden-Phase (CEP) wird ebenfalls durch elektro-optische Abtastung (EOS) gemessen und als stabil, mit Fluktuationen von weniger als 100 mrad über eine Stunde bestätigt.

Abschließend werden nichtlineare optische Prozesse, wie die Erzeugung der zweiten Harmonischen (SHG) und die Selbstphasenmodulation (SPM), durch die erfassten intensiven Nah-Einzelzyklus-Mittelinfrarotimpulse demonstriert. Das Konzept der Erweiterung nichtlinearer optischer Prozesse vom sichtbaren und nahen Infrarot zum mittleren Infrarot wird daher validiert. Diese energiereichen und breitbandigen Mittelinfrarotimpulse zeigen nicht nur ihre Eignung für Experimente bei hohen Feldstärken und Intensitäten im Mittelinfrarotbereich, sondern ermöglichen auch die Realisierung von Spektroskopie im Bereich des molekularen Fingerabdrucks. Ultraschnelle Elektronenbeugung und Mikroskopie zur Beobachtung von Licht-Materie-Wechselwirkungen mit revolutionärer zeitlicher und räumlicher Auflösung sind ebenfalls einsatzbereit und tragen zu einem besseren Verständnis der elementaren Materialien in unserem täglichen Leben bei.

Abstract

Physical and chemical processes that involve electronic or molecular dynamics pretty much establish the world we perceive every day. These ultrafast motions can be either indirectly measured by spectroscopy or directly observed or visualized by ultrafast electron diffraction and microscopy. Spectroscopy requires a broadband mid-infrared spectrum. In particular, frequencies covering the molecular fingerprint region ($2\ \mu\text{m}$ - $20\ \mu\text{m}$) are of interest because they coincide with many vibrational modes of the fundamental molecules. Ultrafast electron diffraction and microscopy demand short electron pulses with durations of femtosecond (10^{-15} s) or even attosecond (10^{-18} s), in order to provide sub-cycle temporal resolution and atomic spatial resolution at the same time. Such electron pulses can be prepared by using the all-optical pulse compression technique, which needs intense single-cycle terahertz or mid-infrared pulses. Therefore, high-power, single-cycle, and phase-stable mid-infrared pulses are highly appreciated.

This work aims to generate the desired mid-infrared pulses through optical parametric down-conversion. First, a hybrid bulk-fiber spectral broadening scheme is employed for preparing ultrashort pulses for later use in intra-pulse difference-frequency generation (IPDFG). A compression factor of 33 is achieved, and 30-fs pulses are generated from 1-ps pulses, with an average power of 4 W.

Next, IPDFG with the 30-fs driving pulses is carried out in a LiGaS_2 (LGS) crystal. Carefully-controlled input polarization leads to efficient generation under type II phase-matching condition. Meanwhile, the generation mechanism is well understood by characterizing the pulse shape and spectrum of the driving pulses after the nonlinear crystal. The balance between spectral broadening, dispersion, and pulse walk-off is found critical for efficient nonlinear frequency conversion in a thick crystal. Mid-infrared radi-

ation ranging from 8-11 μm with a pulse energy of ~ 7 nJ is obtained from a 4-mm LGS crystal.

In order to push the performance of the mid-infrared pulses further, inter-pulse difference-frequency generation (DFG) involving a non-collinear optical parametric amplifier (NOPA) system is utilized. By deliberately manipulating the dispersion of the seed pulses, mid-infrared pulse compression becomes possible with pure bulk materials. These arrangements allow the generation of 1.4-cycle, 7.5- μm mid-infrared pulses with a pulse energy of 220 nJ. The carrier-envelope phase (CEP) is also measured by electro-optic sampling (EOS) and confirmed to be stable with fluctuation of less than 100 mrad over an hour.

Finally, nonlinear optical processes such as second-harmonic generation (SHG) and self-phase modulation (SPM) are demonstrated by the acquired intense near single-cycle mid-infrared pulses. The concept of extending nonlinear optical processes from the visible and the near-infrared to the mid-infrared is therefore validated. These energetic and broadband mid-infrared pulses not only show their ability for high-field and high-intensity experiments at the mid-infrared range but also enable the realization of spectroscopy in the molecular fingerprint region. Ultrafast electron diffraction and microscopy for observing light-matter interactions with revolutionary temporal and spatial resolution are also ready to be put into practice, helping to gain more understandings into the elementary materials in our daily life.

List of publications

Y. Morimoto, Y. Shinohara, M. Tani, **B.-H. Chen**, K. L. Ishikawa and P. Baum, *Asymmetric single-cycle control of valence electron motion in polar chemical bonds*, Nature Photonics *submitted*.

G. Barbiero, H. Wang, J. Brones, **B.-H. Chen**, V. Pervak, and H. Fattahi, *Super-octave terahertz solid-state emitter driven by Yb:YAG thin-disk oscillator*, Journal of Physics B: Atomic, Molecular and Optical Physics *submitted*.

B.-H. Chen, C. Hofer, I. Pupeza, P. Baum, *Second-harmonic generation and self-phase modulation of few-cycle mid-infrared pulses*, Optics Letters **44**, 4079 (2019).

B.-H. Chen, E. Wittmann, Y. Morimoto, P. Baum, and E. Riedle, *Octave-spanning single-cycle middle-infrared generation through optical parametric amplification in LiGaS₂*, Optics Express **27**, 21306 (2019).

B.-H. Chen, T. Nagy, and P. Baum, *Efficient middle-infrared generation in LiGaS₂ by simultaneous spectral broadening and difference-frequency generation*, Optics Letters **43**, 2876 (2018).

B.-H. Chen, M. Kretschmar, D. Ehberger, A. Blumenstein, P. Simon, P. Baum, and T. Nagy, *Compression of picosecond pulses from a thin-disk laser to 30 fs at 4 W average power*, Optics Express **26**, 3861 (2018).

Contents

| | |
|---|-----------|
| Zusammenfassung | vi |
| Abstract | ix |
| List of publications | xi |
| 1 Introduction and the scope of this work | 1 |
| 2 From the visible to the mid-infrared | 7 |
| 2.1 Why mid-infrared pulses? | 7 |
| 2.2 Mid-infrared generation - Parametric frequency down-conversion | 12 |
| 2.2.1 Optical rectification and difference frequency generation | 12 |
| 2.2.2 Intra-pulse and inter-pulse DFG | 14 |
| 2.3 Practical challenges for working with mid-infrared pulses | 18 |
| 2.3.1 Detection | 19 |
| 2.3.2 Dispersion management | 22 |
| 2.3.3 Nonlinear optics with mid-infrared pulses | 24 |
| 2.4 Recent works on the generation of mid-infrared pulses | 24 |
| 3 Compression of picosecond pulses from a thin-disk laser to 30 fs at 4W average power | 27 |
| 3.1 Introduction | 31 |
| 3.2 Single-stage spectral broadening | 32 |
| 3.3 Simulation | 35 |

| | | |
|----------|--|-----------|
| 3.4 | Hybrid double-stage spectral broadening | 36 |
| 3.5 | Conclusion | 40 |
| 4 | Efficient middle-infrared generation in LiGaS₂ by simultaneous spectral broadening and difference-frequency generation | 43 |
| 5 | Octave-spanning single-cycle middle-infrared generation through optical parametric amplification in LiGaS₂ | 53 |
| 5.1 | Introduction | 57 |
| 5.2 | Experimental setup | 58 |
| 5.3 | Pulse compression and characterization | 62 |
| 5.3.1 | Dispersion estimation | 62 |
| 5.3.2 | Electro-optic sampling (EOS) | 64 |
| 5.4 | Beam quality | 66 |
| 5.5 | Power scalability and stability, CEP stability | 67 |
| 5.6 | Discussion and future aspects | 71 |
| 6 | Second-harmonic generation and self-phase modulation of few-cycle mid-infrared pulses | 73 |
| 7 | Conclusions and future aspects | 83 |
| | Data archiving | 85 |
| | Bibliography | 86 |
| | Acknowledgements | 109 |

Introduction and the scope of this work

Back in the 17th century, scientists have already learned that light perceived by human eyes could be decomposed into different colors (wavelength $\lambda \approx 400 \text{ nm}-700 \text{ nm}$) [1]. Later in 1800, W. Herschel discovered and demonstrated in his experiment that there exist “calorific ray” beyond the red part of the visible spectrum, which are now recognized as the “infrared” lights ($\lambda \approx 0.7 \mu\text{m}-1 \text{ mm}$) [2]. This invisible part of the light spectrum immediately found its way to various applications and research fields, notably infrared astronomy, which allows scientists to analyze the composition of certain celestial bodies and explore the universe by discovering new stars and planets [3, 4]. Later on, infrared imaging and tomography were also used to help researchers see more details in living samples without any invasive mean, owing to their deeper penetration depth than visible light. [5–7].

Within the infrared spectrum, mid-infrared ($3 \mu\text{m}-50 \mu\text{m}$) is of particular interest to biologists, chemists, and physicists for several reasons. First, many fundamental molecular motions (e.g. vibrations or other oscillatory normal modes) have such frequencies and absorb the corresponding spectral lines, which lie in what we called the “molecular fingerprint region” ($2 \mu\text{m}-20 \mu\text{m}$) [8–12]. Researchers could utilize these characteristic features to identify and distinguish different gases or materials [13, 14], and potentially apply mid-infrared spectroscopy for medical purposes such as early cancer detection [15, 16]. With the invention of the laser [17] and the development of high power, ultrashort pulse generation techniques [18–20], pulses containing one or even less than one oscillation period have been realized. Combining with peak electric field strength higher than the atomic Coulomb field ($> 1 \text{ GV/m}$), they make a perfect tool for scientists to study ultrafast

electronic dynamics and light-matter interaction in strong-field physics [21]. Thanks to the inverse scaling of the Keldysh parameter γ^1 with wavelength [26], pulses with longer center wavelength enable researchers to do such strong field experiments without having ambiguity between different processes. Moreover, the returning electrons during high-harmonic generation [27–30] would possess more ponderomotive energy when recombining with their parent ions due to quadratic wavelength scaling [27], leading to the emission of photons with shorter wavelengths. This not only helps to produce even shorter laser pulses with attosecond duration (1 as = 10^{-18} s) [31,32] and benefiting the research in attosecond science [33–35], but also equipping the semiconductor industry with the ability to shrink the size of transistors and thus increase the speed of modern electronics.

Another key significance of long-wavelength, few-cycle pulses is their use for manipulating electrons. For instance, laser-driven electron acceleration [36,37] may allow us to accelerate particles for studying fundamental physics and for medical applications on a table-top scale setup. Most important for our research group is all-optical electron beam control by the cycle of laser light [38–40], to advance ultrafast electron microscopy [41] and diffraction [42]. To achieve “atomic resolution”, electrons with energies of a few tens of keV are required, as their corresponding de Broglie wavelengths are much shorter than those of visible or ultraviolet light. Thus they could provide much better spatial resolution. Also, because the vacuum is dispersive to electrons, the duration of electron bunches get broader during propagation. By first reducing the number of electrons in a pulse down to one or less than single electron [43,44], space charge effect could be minimized and so the electron pulses could then be further compressed in time [45–47]. Then, with the help of near single cycle mid-infrared pulses, multi-stage electron pulse compression could be realized [48], leading to isolated attosecond electron pulses instead of a sequence of attosecond pulse train [46,49–51]. This would eventually pave a way to 4D electron microscopy of the fundamental electronic process in molecules and condensed matters with ultimate temporal and spatial resolution.

With the advantages mentioned above, it is crucial to have ultrashort, waveform-controlled, and carrier-envelope phase (CEP)² stable mid-infrared light sources at high

¹A parameter proposed by L. V. Keldysh in 1965, which is often used to describe different ionization processes. For $\gamma \gg 1$, the electron would mainly experience “multi-photon” ionization [22]. On the other hand for $\gamma \ll 1$, the ionization process would be dominated by “tunneling” [23–25].

²Carrier-envelope phase is defined as the phase difference between the peak of the intensity envelope and the nearest peak of the electric field (carrier).

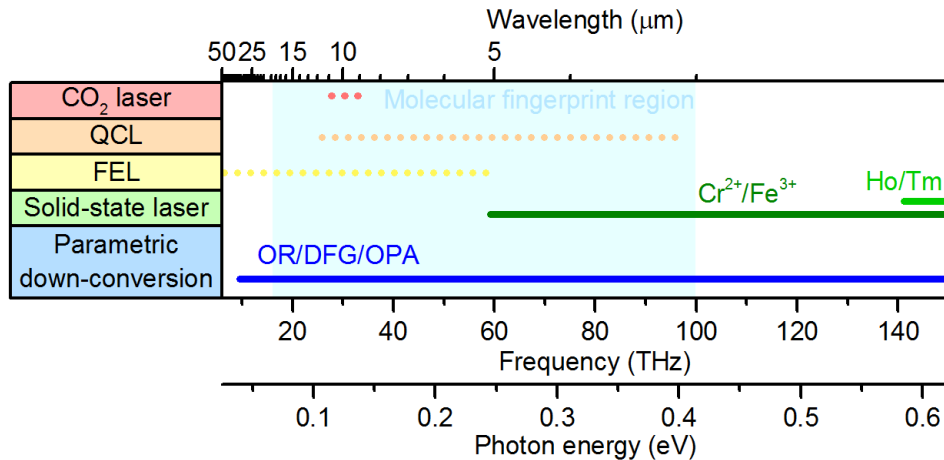


Figure 1.1: Mid-infrared sources and their spectral range. Dotted lines denote narrow-band sources and solid lines denote broadband sources. The light blue block shows the molecular fingerprint region. Figure inspired by [52]

power. In the past few decades there have been several developments, see Fig. 1.1 for a summary. CO₂ lasers radiate mid-infrared light directly and provide continuous wave (CW) or laser pulses with duration of sub-picoseconds ($1 \text{ ps} = 10^{-12} \text{ s}$) [53,54]. Quantum cascade laser (QCL) utilizes inter-sub-band transitions [55–57] that permit electrons to emit photons multiple times. With carefully designed and engineered thicknesses of the quantum wells, quantum cascade lasers can emit a wide range of narrowband mid-infrared light. Free electron lasers (FEL) [58, 59] could offer mid-infrared pulses with enormous power. By adjusting the period of the undulator³, they are capable of producing tunable wavelengths over a broad spectral range. Solid-state lasers also found their way from $0.8 \mu\text{m}$ (Ti:sapphire-based) or $1.03 \mu\text{m}$ (Yb-based) to mid-infrared spectral range. Ho/Tm-based sources provide pulses with bandwidth ranging from 1.9 to $2.1 \mu\text{m}$ [60,61], and Cr²⁺/Fe²⁺ doped lasers could emit light with spectrum covering 2 to $5 \mu\text{m}$ [62, 63]. These mid-infrared sources are without question suitable for several of the applications mentioned above, but there are also substantial obstacles. CO₂ lasers can only deliver pulses with rather long pulse duration. Quantum cascade lasers rely on precise temperature control, and therefore only a few of them can be operated at

³An undulator is an array of periodically arranged magnets whose polarity is alternating, that makes the electrons wiggle when propagating through the undulator. The wiggling electrons would then emit light with a wavelength related to the undulator’s period.

room temperature. Free electron lasers are usually building-size facilities that are not easily accessible and only deliver long pulses with durations of ns or longer. Solid-state lasers with different gain medium require proper pumping laser in order to have high enough conversion efficiency. The alternative to getting over these difficulties and the topic of this thesis is nonlinear frequency conversion of near-IR femtosecond laser pulses, such as optical rectification (OR), optical parametric amplification (OPA) or difference frequency generation (DFG). With the aid of suitable nonlinear crystals, ultrashort coherent mid-infrared pulses at almost any center wavelength could in principle be realized, given certain prerequisites such as phase-matching and transparency. Besides, nonlinear frequency conversion also provides scalable output power as long as the focusing condition is well controlled to avoid crystal damage. This concept offers us a versatile way to generate powerful, broadband, tunable mid-infrared light sources for the applications discussed above.

Structure of this thesis

This work aims, in particular, to generate near single-cycle mid-infrared laser pulses with high field strength, for applying them to the ultrafast electron diffraction (UED) beamline in our laboratory [64]. The thesis is written in a cumulative way, with four original publications [65–68] reprinted in chapter 3-6. In these chapters, a brief background is given before each published article. A summary of this thesis and what has been achieved, together with an outlook are discussed in the end.

Chapter 2 gives an overview of the mid-infrared spectral range. The principle of mid-infrared generation and the relation between the above mentioned nonlinear optical process (OR and DFG) will be discussed. The importance of moving from visible to near-infrared and further to mid-infrared will be pointed out. Differences between these spectral regimes will also be discussed, either in linear or nonlinear optics. Challenges encountered when switching to mid-infrared will also be explored. Lastly, we introduce some recent works on table-top mid-infrared sources and compare them with the present.

Chapter 3 is a reprint of the original publication “Compression of picosecond pulses from a thin-disk laser to 30 fs at 4W average power” [65]. We demonstrate the generation of desired short pulses from a 1-ps Yb:YAG laser for subsequent intra-pulse difference frequency generation. A hybrid spectral broadening scheme with a first stage bulk material broadening and hollow-core fiber broadening is applied. The generated pulses are employed in the mid-infrared generation, as is described later in chapter 4.

Chapter 4 bases on a reprint of the original publication “Efficient middle-infrared generation in LiGaS_2 by simultaneous spectral broadening and difference-frequency generation” [66]. We show the results of the mid-infrared generation in LiGaS_2 (LGS) crystal. A phenomenon of pumping power-dependent spectral shift in the mid-infrared spectrum is observed, and we discuss the physics behind in detail. These results also provide a new approach that, by balancing the dispersion, walk-off, and spectral broadening in a nonlinear crystal, broadband mid-infrared radiation could be produced even with thick crystal.

Chapter 5 is a reprint of the original publication “Octave-spanning single-cycle middle-infrared generation through optical parametric amplification in LiGaS_2 ” [67]. We present another way to produce mid-infrared radiation. Unlike intra-pulse difference-frequency generation, inter-pulse difference frequency generation utilizes the whole spectra of in-coming pump and seed, thus gives rise to higher conversion efficiency. The dispersion of the whole setup is well designed such that the generated mid-infrared pulses could be easily compressed to the single-cycle regime with few millimeters of Germanium (Ge). We also characterized the mid-infrared field transient by electro-optic sampling (EOS).

Chapter 6 contains the results that have been published in Optics Letters with the title “Second-harmonic generation and self-phase modulation of few-cycle mid-infrared pulses” [68]. We report the first application with the mid-infrared source generated in chapter 5, which are second-harmonic generation in GaSe crystal and self-phase modulation in various materials. The experiments not only show that nonlinear processes maintain their properties also in the mid-infrared regime, but also suggest that mid-infrared spectrum could be further broadened and compressed down to sub-cycle regime, which is beneficial in many aspects, as mentioned earlier.

Chapter 7 summarizes the entire work toward near single-cycle mid-infrared pulse generation. Potential further improvement of the system is discussed, and possible applications are also proposed, which could lead to the realization of ultimate resolution for ultrafast electron diffraction/microscopy, both in time and space.

From the visible to the mid-infrared

In this chapter, the significance of obtaining ultrafast mid-infrared pulses is substantiated with more details. Then we proceed to discuss the widely used technique for mid-infrared generation - optical parametric frequency down-conversion. Here, direct laser emission is avoided by employing coherent pulses at conventional wavelengths in the visible and near-infrared, and then convert them to mid-infrared pulses by the non-linear optical process. The confusing ambiguity between the two useful and often-applied $\chi^{(2)}$ processes, *optical rectification (OR)* and *difference frequency generation (DFG)*, is clarified. We will also investigate more on the two categories of DFG, intra-pulse DFG, and inter-pulse DFG, and point out their advantages and disadvantages. The practical obstacles encountered when using mid-infrared pulses for applications such as spectroscopy and electron control are also addressed in this chapter. In the end, we conclude with a comprehensive survey on recent works on mid-infrared light sources, including the results presented in the next chapters of this thesis.

2.1 Why mid-infrared pulses?

As mentioned earlier, molecules have very specific vibrational or rotational motions, and each of them has their particular frequency, oscillator strength, nonlinearity, and anharmonic coupling. These frequencies, especially the vibrational motions, lie mostly within the mid-infrared range of the electromagnetic spectrum¹. For example, the CO

¹Rotational motions are usually slower than vibrational motions and have frequencies that lie in the microwave range.

molecule has groups of vibrational modes at frequencies around 136 THz ($2.2 \mu\text{m}$) and 64 THz ($4.7 \mu\text{m}$) and the CO_2 molecule has an asymmetric stretching vibration at frequencies around 70 THz ($4.3 \mu\text{m}$) [9]. When electromagnetic waves with those specific frequencies shine on the molecules, these motions would be excited and absorb the corresponding energy of those radiations. Hence, we could utilize this feature to identify the composition of an unknown substance of interest. With broadband mid-infrared pulses, it is even possible to identify multiple features at the same time and apply them for example to air pollution or cancer detection [16], making mid-infrared pulses vital to both life science and the industry.

Aside from exciting molecular motions, mid-infrared radiation can also be used to drive coherent phonon modes² in complex compounds or crystals. Upon phonon excitation, some insulators could change their electronic properties and become conductive [69]. For some superconductors, they could even be operated above their critical temperature when illuminated by mid-infrared pulses [70]. These insulator-metal transitions induced by phonon excitation opens up a way to manipulate transition between insulator and conductor in an ultrafast fashion and furthermore, make superconductor potentially usable at room temperature [71].

One key point that makes mid-infrared radiation indispensable is its much-lower photon energy compared to visible light (see also Fig. 2.1, red dots). For most nonlinear optical processes or high-field experiments, the main issue is to avoid crystal/material damage while still preserving enough peak field strength for the desired high-field effects. If the driving laser wavelength enters the mid-infrared regime, the photon energies are lower than 1 eV, which is much lower than the bandgap of typical nonlinear crystals. Such property allows us to apply more intense pulses for studying extreme nonlinear processes and light-matter interaction [21] without causing two- or multi-photon absorption and inducing thermal damage. Another benefit of having mid-infrared lasers for high-field physics, for example, high-harmonic generation [28], is the quadratic scaling of ponderomotive energy³ with the driving wavelength [22]. As seen from Fig. 2.1, when moving from 800 nm to $7.5 \mu\text{m}$ ⁴, the ponderomotive energy increases by a factor of > 80 . Therefore, in the process of high-harmonic generation driven by mid-infrared

²A collective motion of the lattice in a crystal when excited by the acoustic or optical wave.

³The time-averaged energy gained by a charged particle, for example, electron, in an electromagnetic field. The longer the wavelength is, the longer time the charged particle would spend in the oscillating field, and as a result, more energy would be acquired.

⁴In chapter 4 and 5, we will demonstrate the generation of mid-infrared pulses at $7.5 \mu\text{m}$.

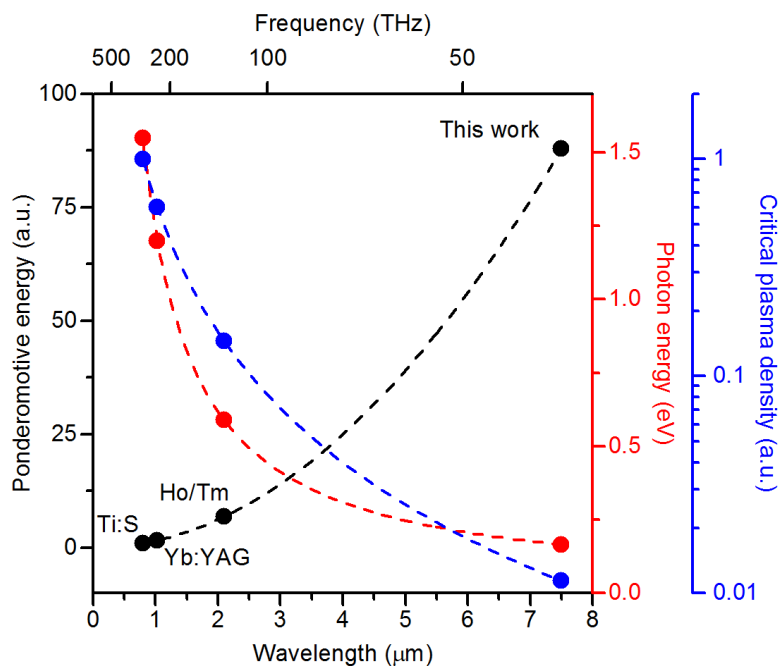


Figure 2.1: Scaling of photon energy (red), ponderomotive energy (black) and critical plasma density (blue) with wavelength. All points are plotted by assuming the same intensity. Left axis represents the ponderomotive energy normalized to the one at wavelength of 800 nm. Common laser sources are compared here: Ti:S, titanium-sapphire lasers (800 nm); Yb:YAG, ytterbium-doped yttrium aluminium garnet lasers (1030nm); Ho/Tm; holmium and thulium doped lasers (2.1 μm); this work (7.5 μm).

pulses, the electrons could gain much more energy during the acceleration stage [28]⁵. When these electrons return and re-combine with their parent ions, photons with much higher energy, such as extreme ultraviolet (EUV, 10 - 100 eV), would be emitted. Such short-wavelength radiation could lead to isolated attosecond laser pulses, which provide unprecedented time resolution in attosecond science. On the other hand, owing to their extremely short wavelength, such XUV pulses are also a powerful tool for photolithography in the semiconductor fabrication process. Electronics with circuit line-width smaller than tens of nanometers and beyond may become possible to produce in this way.

The ability to control electrons for electron microscopy, diffraction, and particle acceleration makes mid-infrared pulses even more attractive. Ultrashort mid-infrared

⁵High-harmonic generation could be described by a simplified three-step model: (1) tunneling ionization, (2) acceleration, and (3) recombination.

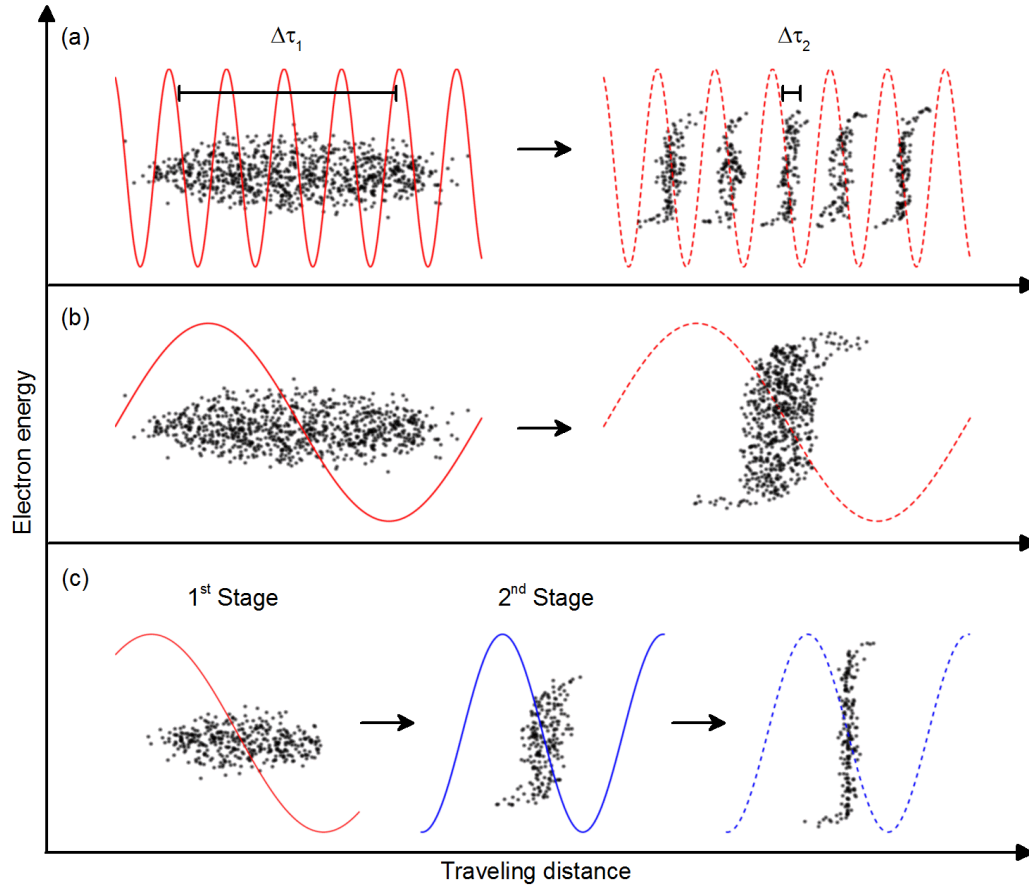


Figure 2.2: Schematic of electron pulse shortening via optical field. (a) Electron pulse compression with light field period much shorter than the pulse duration. $\Delta\tau_1$ stands for the electron pulse duration before compression and $\Delta\tau_2$ represents the duration after compression. (b) Electron pulse compression with light field period comparable to the pulse duration. (c) Concept of 2 stage compression with single-cycle THz (red) and mid-infrared (blue) pulses.

pulses offer a way to accelerate electrons up to MeV energy within just a few centimeters of interaction length. By sending a short and powerful laser pulse into a cloud of atoms (for example, hydrogen gas [37]), the pulses would ionize the atoms and create plasma. Moreover, the pulses push the plasma electrons away from their original position by ponderomotive force. An area of positive ions is created just behind the driving laser pulse and moves with the laser pulse, which is known as the “wakefield”. If an electron is sent together with the laser pulse, this electron will be trapped inside the wakefield and experience acceleration during the propagation. With laser pulses at longer wavelengths,

the plasma density needed to achieve such acceleration, also known as the critical plasma density, becomes lower. As shown in Fig. 2.1, the critical plasma density for a 7.5- μm driving wavelength is almost 100 times less than the one for 800 nm. Such long-wavelength pulses would make the experimental condition much less difficult to be fulfilled.

Last but not least, short mid-infrared bursts are also vital for the use of electron pulse compression in time-resolved microscopy and diffraction. In order to boost the temporal resolution of electron microscopy and time-resolved electron diffraction, electron bunches with a duration of femtoseconds or even shorter are desired. Conventionally, it was achieved by synchronizing the electron pulses with a microwave cavity [72], and pulses with sub-phonon resolution were demonstrated [73]. However, this method suffers from timing jitter between the electron pulses and the electronic signals in the microwave generation that blurs the measurement, and therefore, a sophisticated, active compensation and stabilization are needed [74]. On the other hand, electron pulse compression with optical field cycles is immune to such problem [45]. As the electron pulses and the optical wave originate from the same laser source, they are passively synchronized with sub-light cycle precision. This approach has been demonstrated with terahertz pulses [45] and near-infrared pulses [46, 50]. In these latter cases, however, the period of the field cycle is much shorter than the incoming electron pulse duration. As a result, the electron pulses are partly compressed in every light cycle, leading to a train or sequence of ultrashort pulses (see Fig. 2.2(a)) instead of an isolated, single-electron pulse. In order to generate genuinely isolated electron pulses, optical pulses with longer field cycles (period longer than twice the electron pulse duration) are therefore needed [45, 47], as shown in Fig. 2.2(b). Isolated electron pulses with attosecond duration can be obtained by multiple-stage compression [48], and this is where intense, single-cycle mid-infrared pulses come into place. As depicted in Fig. 2.2(c), the few-hundred-femtosecond electron pulses from a photoemission source could be first compressed down to tens of femtoseconds by a first THz compression stage [45], as mentioned above. Then a second compression stage employing few-cycle mid-infrared pulses can further compress the electron bunches down to sub-ten femtosecond or even attosecond duration. This compression technique will certainly advance ultrafast electron diffraction and microscopy to sub-cycle resolution while maintaining their sub-atomic resolution in space.

Given these advantageous scaling laws and future practical applications, there is a high demand for broadband, single-cycle, and intense mid-infrared pulses, which is the scope of this thesis. In the following sections, we will see how mid-infrared pulses are

generated through different schemes of nonlinear optical processes and their comparison, followed by some obstacles when dealing with short mid-infrared pulses, critical discussion, and an overview of recent works on short mid-infrared pulse generation.

2.2 Mid-infrared generation - Parametric frequency down-conversion

In Fig. 1.1, we have listed several approaches to generating mid-infrared sources. Among them, it is clear that nonlinear frequency conversion offers the broadest tunability and mid-infrared coverage. In this section, we will briefly walk through the physical principles of parametric down-conversion. We will also discuss the connections and differences between different generation schemes. Then we will proceed to demonstrate some of the properties of the generation schemes in the experiment and finally compare their pros and cons.

2.2.1 Optical rectification and difference frequency generation

Ever since second-harmonic generation was demonstrated in 1961 [75], nonlinear optical processes have been studied extensively, and their behavior could be well described by *nonlinear polarization* $P^{NL}(t)$ [76], which is usually expressed as a series of Taylor expansion⁶. Among all these higher-order terms, the second-order term contains the governing mechanism of MIR generation that will be discussed in this section. In principle, with two interacting light frequencies ω_1 and ω_2 ($\omega_1 > \omega_2$), there are four possible $\chi^{(2)}$ frequency-mixing combinations [76]. Only two of them would give rise to lower frequencies, which are *optical rectification* (*OR*, $\omega_1 - \omega_1$ or $\omega_2 - \omega_2$) and *difference frequency generation* (*DFG*, $\omega_1 - \omega_2$).

These two processes are, in fact, closely related. For optical rectification, the electrons' motion inside the material follows the slowly-varying input pulse envelope shape and equivalently create a slowly changing DC polarization that emits terahertz or mid-

⁶Nonlinear polarization $P^{NL}(t)$ is usually expressed as $P^{NL}(t) = \epsilon_0(\chi^{(1)}E(t) + \chi^{(2)}E^2(t) + \chi^{(3)}E^3(t) + \dots)$, where ϵ_0 is the electric permittivity of free space, χ^n is the n^{th} order susceptibility and $E(t)$ is the externally applied electric field.

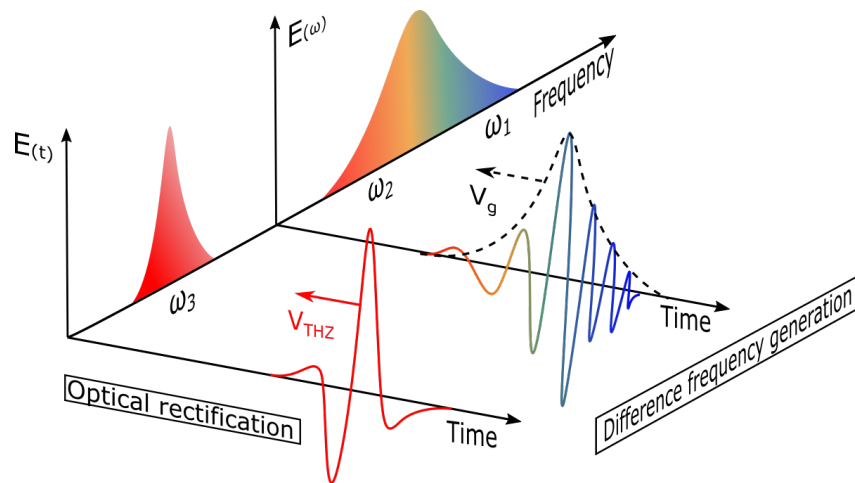


Figure 2.3: Different pictures of optical rectification (OR) and difference frequency generation (DFG). The process of optical rectification could be understood in the time domain. The emitted long-wavelength transient follows the derivative of the driving pulse intensity profile. On the other hand, difference frequency generation is easier to be understood in the frequency domain. Any pair of high frequency component (ω_1) and low frequency component (ω_2) in the input spectrum could generate their own difference frequency (ω_3).

infrared radiation. As long as the phase-matching condition⁷ is satisfied, the amplitude of the newly generated low-frequency radiation could be built up, resulting in high conversion efficiency. However, this picture does not seem to hold when the input pulse becomes shorter - the electrons now see a fast-changing envelope. In this case, one could view the whole process in the frequency domain. As the pulse gets shorter in duration, the corresponding spectrum becomes broader. All the frequency components, including the lowest and highest frequency parts, are confined in a short amount of time, within the pulse duration. As a consequence, they interfere with each other and form beating frequencies. The lower one, which is the difference of the frequency components ($\omega_1 - \omega_2$), therefore produce terahertz or mid-infrared radiation. This process is essentially the same as the other well-known $\chi^{(2)}$ process - difference frequency generation. The two pictures are summarized in Fig. 2.3. One could also see the connection to the phase-

⁷For efficient optical rectification, the driving pulse should travel at the same speed as the newly generated frequency (group velocity of the driving pulse equals the phase velocity of the new frequency). Thus the phase-matching condition is $n_{group}^{input} = n_{phase}^{THz}$

matching condition. For the simplest case $\omega_p - \omega_s \rightarrow \omega_i$, where the subscripts p, s and i stands for pump, signal and idler, respectively, the phase-matching condition is

$$n_p \omega_p - n_s \omega_s = n_i \omega_i. \quad (2.1)$$

Since $\omega_p = \omega_s + \omega_i$, Eq. 2.1 can be rewritten as

$$n_p + \frac{(n_p - n_s)}{\omega_i} \omega_s = n_i. \quad (2.2)$$

Now if ω_p and ω_s are getting closer ($\omega_p - \omega_s \rightarrow d\omega$), as if the spectrum becomes much narrower and the corresponding temporal pulse duration becomes longer, the phase-matching condition would become

$$n_p + \frac{dn}{d\omega} \omega_s = n_i, \quad (2.3)$$

where the left-hand side of the equation equals to the group refractive index

$$n_g^p = n_i. \quad (2.4)$$

Equation 2.4 is very similar to the phase-matching condition for optical rectification: the input driving pulse (pump) and the newly generated terahertz or mid-infrared (idler) should travel at the same speed.

2.2.2 Intra-pulse and inter-pulse DFG

We have now seen the connection between optical rectification and difference frequency generation. As described in the previous section, only one pulse is needed for such processes, although the use of separate beams can also be advantageous. The one-pulse driven difference frequency generation is also often referred to as intra-pulse difference frequency generation (IPDFG) because all the interacting frequencies are coming from the same optical pulse. There is another category of difference frequency generation that the interacting frequencies ω_1 and ω_2 are from two separate pulses, and it is usually named inter-pulse difference generation or simply difference frequency generation (DFG). The main difference is illustrated in Fig. 2.4. Both schemes have been widely used to generate mid-infrared radiation, as will be shown at the end of this chapter. Here, we compare these two approaches and discuss their advantages and disadvantages for short mid-infrared pulse generation and practical applications.

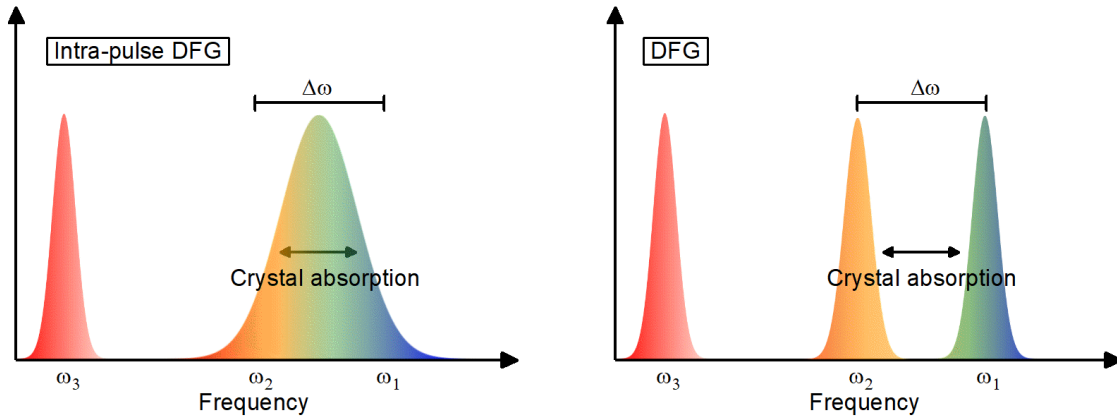


Figure 2.4: Comparison between intra-pulse difference frequency generation (IPDFG) and inter-pulse difference frequency generation (DFG). For IPDFG, the pump (ω_1) and seed (ω_2) come from the same pulse, and their difference $\Delta\omega$ is the newly generated frequency ω_3 . For DFG, the interacting pump and seed come from separate pulses with relatively narrower spectrum comparing to the case of IPDFG. The left-right arrow denotes the cut-off frequency of the transparency range. Frequencies that are lower than the cut-off frequency would be absorbed.

Experimentally, IPDFG is, without a doubt superior to DFG in terms of beam alignment. Because there is only one pulse used in IPDFG, any beam pointing fluctuation would not affect the generation process too much, because the beam is completely overlapping with itself. Consequently, the carrier-envelope phase (CEP) is passively stabilized as long as the pump and seed originate from the same source [77] and as long as the chirp in the pulses remains constant over time⁸. On the other hand, for DFG, slight beam misalignments between the pump and seed would not only lead to lower generation efficiency but also cause angular dispersion in the idler beam. Moreover, any tiny instability in the experimental setup would induce timing jitter between the pump pulse and the seed pulse, therefore directly introduce CEP fluctuations.

Despite the disadvantages as mentioned earlier, DFG has many advantages over IPDFG as well. First of all, Fig. 2.4 clearly shows that for IPDFG, the whole process only utilizes the wings of the input spectrum, while for DFG the full pump and seed spectrum could be exploited. Therefore, the usage of two separate spectra not only

⁸Carrier-envelope phase plays an important role when the laser pulse becomes shorter and contains one or less-than one field cycle. For example, for two single-cycle pulses with CEP equals 0 (cosine pulse) and CEP equals $\pi/2$ (sine pulse), their peak field strength would differ by a 0.8 times or more, which could drastically change the results of field-sensitive measurements such as high-harmonic generation.

makes the generation more efficient, as we will see in chapter 4 and 5, but also provides a chance to apply high pump power while still avoiding crystal damage. Another fact that we could see from Fig. 2.4 is that, one needs a spectrum that is broad enough to support the desired difference frequency for IPDFG, which adds more complexities to the experimental setup such as extra stages for spectral broadening and post pulse compression, leading to lower overall conversion efficiency.

As will be reported in chapter 5, the seed pulses DFG are usually generated through an optical parametric amplification (OPA) process, which offers a wide tunability. Such OPA stage allows fine-tuning the seed's center frequency and spectrum to obtain the desired mid-infrared pulses. Meanwhile, the CEP of the generated mid-infrared could be controlled by fine-tuning the relative time delay between the pump and the seed pulses. The ability to control the CEP ensures us to perform CEP dependent measurements without altering the beam quality or pulse duration, which is rather tricky for IPDFG because there is no tunable delay. Dispersive materials providing third-order dispersion (TOD) are often required in the beam path to adjust the relative delay between the red part and the blue part of the spectrum within the pulse [78].

Power controllability is another issue that is often overlooked when comparing these two schemes. As mentioned earlier, most IPDFG experiments [79, 66, 80] first generate ultrashort pulses via spectral broadening (e.g., photonic crystal fibers), compress the pulse to near Fourier limit (e.g., with chirped mirrors) and then send the pulses directly into nonlinear crystals for IPDFG. This scheme imposes some challenges for changing the power of the mid-infrared pulses. Achromatic waveplates and broadband polarizers could be used for power adjustment, but such components are usually not available and require unique coating design. Alternatively, conventional waveplates and polarizers could be adopted for adjusting the power before spectral broadening, but it would change the overall broadened spectrum and as a result, alter the final mid-infrared spectrum.

However, this is not the case for DFG. Here, we experimentally demonstrate the beneficial properties of DFG⁹ and show that DFG does not share the downsides of IPDFG. The results are shown in Fig. 2.5. First of all, because there are two interacting pulses, and the pump pulse has a narrow-band spectrum, the pump power can be easily adjusted by the conventional half-wave plate and polarizer. Such power adjustment allows us to change the power of the mid-infrared pulses while keeping the generated mid-infrared spectrum unaffected, as could be seen in Fig. 2.5(a). As we increase the pump

⁹This demonstration uses the same experimental setup as described in chapter 5. The spectrum and the CEP of the generated mid-infrared pulses are measured as a function of the input pump power.

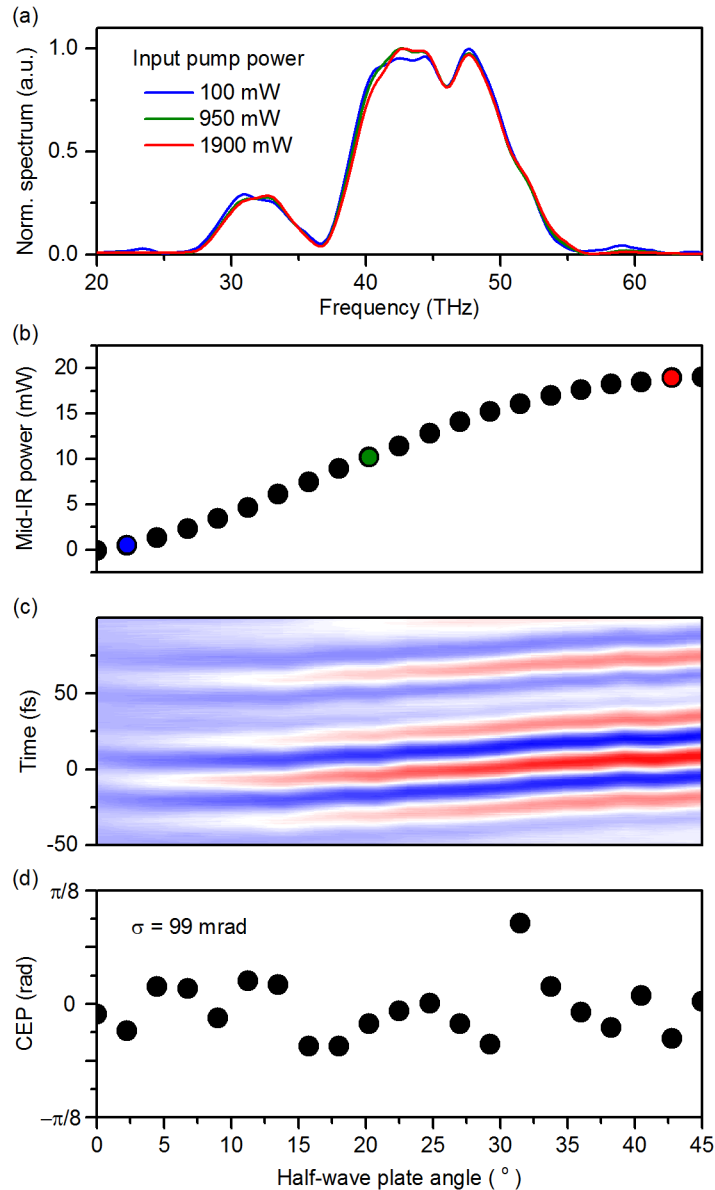


Figure 2.5: Mid-infrared power controllability and CEP preservation through DFG scheme. (a) Generated mid-infrared spectrum with different input pump power. (b) Controlling the power of mid-infrared pulses by rotating the half-wave plate for pump power adjustment. The blue, green and red dots correspond to the spectra in Fig. 2.5(a). (c) Mid-infrared field transient measured by electro-optic sampling (EOS), as a function of input pump power. (d) Carrier-envelope phase extracted from the measurement shown in Fig. 2.5(c). The fluctuation of 99 mrad clearly indicates that the CEP of the mid-infrared pulses remains almost constant for different input pump power.

power from 100 mW (blue curve) to almost 2 W (red curve), the generated mid-infrared spectra do not show any substantial change in spectral shape or bandwidth. Also, we measure the field transient of the mid-infrared pulses with electro-optic sampling (EOS), as a function of input pump power. We find that, as predicted in theory [81], the CEP of the mid-infrared pulses is independent of the pump power. Fig. 2.5(c) and (d) show the results of the measurement. Again, no significant change in the CEP is observed, and the fluctuation of 99 mrad is within the stability range of the system (see Fig. 5.11). The shift in EOS trace observed in Fig. 2.5(c) is an overall group delay effect, which is probably caused by the thermal expansion of the nonlinear crystal and does not affect the CEP. These properties of DFG enable us to perform power- or intensity-dependent measurements with fixed field transient.

Table 2.1 summarizes the advantages and disadvantages of the two DFG schemes that have been discussed in this section. Both approaches have their benefits, depending on the application of interest. For our research group, the main purpose of having mid-infrared is for electron pulse compression and sample excitation for ultrafast electron diffraction and microscopy. Therefore, high field-strength, near single-cycle mid-infrared pulses are desired. In chapter 4 we will first demonstrate mid-infrared generation via IPDFG, and then in chapter 5, DFG will be employed. The advantages and disadvantages discussed in this section could be observed in and investigated by these experiments.

2.3 Practical challenges for working with mid-infrared pulses

Knowing how to generate mid-infrared pulses is just a first step toward their application in spectroscopy, high-field experiments, and electron control. A lot of practical challenges will be encountered when dealing with mid-infrared pulses. Developing techniques to cope with this exclusive spectral range is, therefore, a primary task, which is the main topic of this section.

Table 2.1: Comparison between IPDFG and DFG.

| Property | IPDFG | DFG |
|--------------------------------|-------|-----|
| Beam alignment | O | X |
| CEP stability | O | X |
| Power controllability | X | O |
| Efficiency | X | O |
| Frequency tunability | X | O |
| System simplicity ^a | X | O |

^aNo extra spectral broadening stage or laser pulse compression is required.

2.3.1 Detection

The first practical challenge after generating ultrafast mid-infrared pulses is how to detect them. Unlike the visible or near-infrared light, mid-infrared radiation is not detected by standard Si-, InGaAs- or GaP-based detectors because the photon energy is lower than the bandgap (see also Fig. 2.1). Even with narrow-bandwidth semiconductors such as HgCdTe, the detectable range is still limited to below $\sim 40 \mu\text{m}$ [82]. Furthermore, these detectors often need to be cooled to a cryogenic temperature in order to provide the necessary sensitivity, which complicates the measurement process.

In general, gas-filled Golay cells [83] and pyroelectric devices are commonly used to sense the mid-infrared radiation. A Golay cell comprises several main parts: an infrared-absorber, a gas-filled cavity, a thin membrane, and an optical read-out system (see also [84]). When being irradiated by the mid-infrared pulses, the infrared-absorber inside the Golay cell absorbs the light, causing the gas to expand. The tiny expansion in volume deforms the flexible thin membrane and therefore changes the optical signal reflected from the membrane, causing a difference in the read-out. Such difference can be very subtle, which makes the detection extremely sensitive and enables us to detect spectral components extending from the mid-infrared to the terahertz regime. With the help of the lock-in amplifier, measuring powers as low as nW becomes possible. On the other

hand, because the expansion of the thin membrane determines the detection process, it also limits the measurable power up to a few tens of μW .

Pyroelectric devices utilize the pyroelectric current that is created in some crystals when there is a temperature gradient [85]. Such current is very susceptible to temperature changes and is exploited as a measure of power or beam profile. Powers up to hundreds of mW could be measured with the pyroelectric detectors because the detection process does not include any mechanical moving parts as the Golay cells do. Unfortunately, due to technical reasons, these cameras can only be manufactured with pixel sizes of tens of μm , which is much larger than standard CMOS based sensors for the visible range ($<10 \mu\text{m}$). In our work, we use the pyroelectric detector for mid-infrared power detection (chapter 4) because of their higher detectable range. Also, the pyroelectric detectors could be operated at room temperature, which greatly reduces the measurement complexity.

Once we measured the power, the second task is to measure the spectrum. However, as mentioned above, the lack of proper detector makes it difficult to build a spectrometer. In addition, depending on the coating, gratings for the mid-infrared range are either narrow-band or not efficient, limiting the measurable spectral bandwidth. Also, because the mid-infrared light is invisible to the human eye, aligning the beam into a fiber or a spectrometer would be extremely time consuming.

Nowadays, two methods have been widely used for measuring the spectrum - *Fourier-transform infrared (FTIR)* spectrometer and *electro-optic sampling (EOS)*. FTIR is a linear measurement. It is a Michelson interferometer, in which the pulses to be measured are separated into two parts, with one delayed, and then re-combined together onto a detector (see section 2.3.1). By moving the delay, the two re-combining beams would constructively or destructively interfere with each other, by which the spectral components are encoded and can be retrieved by Fourier transformation. In principle, FTIR gives us unlimited measurement bandwidth and resolution - longer measurement delays give rise to better spectral resolution, and finer delay steps lead to broader detection bandwidth. However in practice, the measurement is still limited by (1) the detector's sensitivity and (2) the bandwidth of the beam splitter used in the interferometer. A broadband mid-infrared beam splitter that covers the molecular fingerprint region is so far not yet available. Reflective optics for beam separation are thus often used to overcome this problem.

On the other hand, EOS is a nonlinear measurement, which can provide us the phase information. The working principle can be understood in the following two ways.

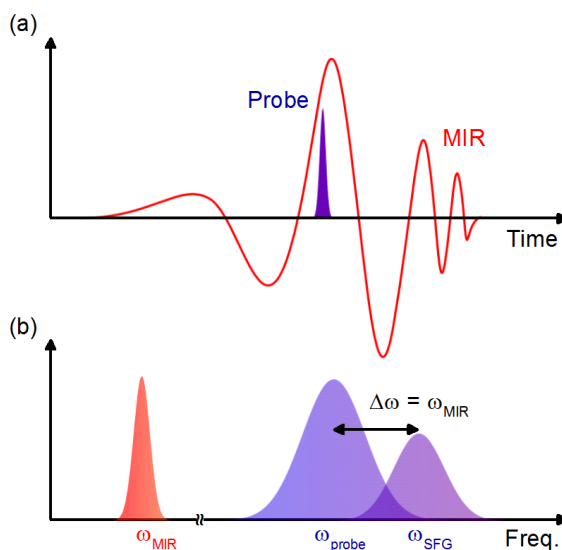


Figure 2.6: Temporal and spectral point of views of the working principle of electro-optic sampling. (a) Temporal picture. An ultrashort pulse delays and overlaps with the unknown mid-infrared (MIR) field in time. The local field strength of the mid-infrared pulse induces Pockels effect, which rotates the polarization of the probe pulse. The mid-infrared field transient could then be deduced from the polarization change. (b) Spectral picture. When the probe pulse is delayed and temporally overlapped with the mid-infrared field, they generate a new, shifted spectrum through sum frequency generation (SFG). This newly generated spectrum overlaps and interferes with the original probe spectrum. By measuring the spectral interference of the overlapped part, the mid-infrared field transient could be obtained.

From the temporal aspect, the electric field of the mid-infrared pulse induces a local Pockels effect and rotates the polarization of the probe pulse when they overlap inside an electro-optic crystal. Such a change in the polarization state can be recorded as a function of the relative delay between the two pulses, from which the mid-infrared field transient can be retrieved. From the spectral aspect, a new spectrum, which is generated through sum-frequency generation (SFG) of the mid-infrared pulse and the probe pulse, interferes with the probe spectrum. Such interference is also measured as a function of the relative delay between the two pulses, and the full phase information can, therefore, be reconstructed. Fig. 2.6 summarizes the working principle of EOS (see also [86, 87]). With this approach, the demands on the proper detector could be relaxed, because the probing pulses used in EOS are often in the visible or near-infrared range. The detection bandwidth is still restricted. The probing pulse duration limits the temporal resolution

and thus the measurable spectral bandwidth at high frequencies. The transmission range and the phase-matching bandwidth of the nonlinear EOS crystal also set a limit to the detection range, typically at the low frequencies. Ultrashort probe pulses and thin EOS crystals are therefore required to increase the detection bandwidth (see chapter 5). In our work, we employ EOS to characterize the CEP and the pulse duration of the mid-infrared pulses. FTIR is also utilized to not only measure the mid-infrared spectrum but also act as a tool for confirming the reliability of the EOS measurement, making the results more credible.

2.3.2 Dispersion management

In order to obtain ultrashort pulses, a broadband spectrum is not enough. Proper dispersion management aiming for a flat spectral phase across the spectrum is necessary¹⁰. For pulses with carrier frequencies in the visible or near-infrared range, dispersion control is often achieved with grating compressors, prism compressors or chirp mirrors. These techniques, however, cannot easily be extended to the mid-infrared range. Besides the above-mentioned drawbacks of gratings for the mid-infrared, the alignment of grating or prism is also complicated and tricky, because the beam to be aligned has a huge beam diameter and is invisible. The transmission range of bulk materials is another concern when constructing a prism compressor because only a few optical materials can transmit mid-infrared wavelength above 20 μm while being dispersive enough for pulse compression [88].

Chirped mirrors are another widely used alternative for post pulse compression, especially for fiber broadening systems (see also chapter 3) [65]. By precisely arranging the coating layers, chirped mirrors can in principle compress pulses with arbitrary phases, given that the phase to be compensated is known. Several difficulties are encountered when designing chirped mirrors for mid-infrared range. First, the coating material's transparency range must cover the spectrum of the pulse to be compressed. Secondly, for typical chirped mirror designs, two different materials with high and low refractive index are required [89]. Also, the functional material properties such as adhesiveness and stiffness need to be taken into account. Such materials that are appropriate for mid-infrared are unfortunately rare. Lastly, because of the longer wavelength in the

¹⁰A perfectly flat phase is not practical. For most of the time, the goal is to minimize the higher-order dispersion terms such as group delay dispersion (GDD) and third-order dispersion (TOD) in order to compress the laser pulses as short as possible.

mid-infrared spectral range, the thickness of the coating layers also increases a lot compared to coatings for visible or near-infrared light. Thicker layers impose substantial difficulties for manufacturing and introduce more fabrication imprecision. In order to reduce the thickness error, the total number of layers is therefore restricted. As a result, the amount of GDD compensated per reflection is limited.

The sign of the dispersion also needs to be taken into account. Most materials that are transparent to the mid-infrared are anomalously dispersive in the mid-infrared regime¹¹. At the same time, they possess vast values of third-order dispersion (TOD) (see table 2.2), which would unfavorably distort the mid-infrared pulses and make post-pulse compression more challenging. Fortunately, due to the phase-subtraction nature of the difference-frequency generation process, the generated mid-infrared pulses will have the opposite sign to the phase of seed pulses. Hence, dispersion management of the driving seed pulses before mid-infrared generation is useful for mid-infrared pulse compression. In chapter 5, we will show that by deliberately controlling the dispersion of the seed pulse before DFG to be positively chirped, the phase of the generated mid-infrared could be manipulated to be negative. Post-compression down to near single-cycle pulse duration is then possible by simply adding bulk material such as Germanium plates (see table 2.2). For electron-control experiments, a window such as ZnSe must be installed in order to couple the mid-infrared pulses into the vacuum chamber. The thickness and the resulting dispersion will also have to be taken into account, and then the chirp of the seed pulses need to be modified accordingly.

Table 2.2: Group delay dispersion (GDD) and third order dispersion (TOD) of some commonly used mid-infrared transparent materials.

| Material | Ge | ZnSe | ZnS | GaAs | AgCl |
|------------------------|------|------|-------|------|------|
| GDD (fs ²) | 501 | -406 | -1030 | -190 | -330 |
| TOD (fs ³) | 2400 | 5950 | 13850 | 6220 | 4100 |

¹¹For pulses in the visible or near-infrared range, they experience normal dispersion when propagating through the materials, meaning that the red part travels faster than the blue part.

2.3.3 Nonlinear optics with mid-infrared pulses

Nonlinear optical effects have been studied for more than half a century [75], but so far mostly with visible or near-infrared light sources. It is therefore fair to ask how the well-known nonlinear processes such as second-harmonic generation (SHG) and self-phase modulation (SPM) would behave in the mid-infrared range, where so far not much experimental evidence is reported. The nonlinearity or efficiency scaling of such conversions with wavelength is still not yet clear by experiments. Also, in order to obtain the full molecular fingerprint spectral range ($2\ \mu\text{m}$ - $20\ \mu\text{m}$) and fill the spectral gaps between mid-infrared and terahertz, nonlinear frequency conversion with mid-infrared is without a doubt necessary. Thus, more experiments on mid-infrared nonlinear processes are strongly desired. Only very recently, a few reports on nonlinear optical processes such as second harmonic generation [90], self-phase modulation [91] and supercontinuum generation in fibers [92] have been demonstrated. In chapter 6, we will report, based on the intense, few-cycle mid-infrared pulses obtained from chapter 5, second harmonic generation and self-phase modulation in various bulk materials, providing key results to the extension of the nonlinear process to the mid-infrared.

2.4 Recent works on the generation of mid-infrared pulses

So far, we have seen the benefits and the importance of applying mid-infrared pulses in various fields. Despite the difficulties and obstacles mentioned in the previous section, the interest of obtaining high-energy, few-cycle mid-infrared pulses is still growing. A comprehensive survey of state-of-art ultrashort mid-infrared light sources is shown in figure 2.7. Pulse energy and the number of cycles within the full-width-at-half-maximum (FWHM) pulse duration are plotted for comparison, including the results presented in this thesis.

Several tendencies can be observed. First of all, there is a gap at around $15\ \mu\text{m}$, where only a few reports generate mid-infrared pulses with center wavelengths beyond $15\ \mu\text{m}$ [93–95]. The lack of mid-infrared pulses with longer wavelengths reflects the fact that a suitable nonlinear optical crystal with broad mid-infrared transparency range, such as GaSe, is rare. Next, for generations by IPDFG (triangles), the generated center wavelengths sit within a narrow range around $10\ \mu\text{m}$, while for OPA or DFG (circles), the

generated mid-infrared wavelengths extend from $\sim 3 \mu\text{m}$ to $\sim 22 \mu\text{m}$. Such distribution shows the superiority of frequency tunability of DFG over IPDFG (section 2.2.2). Also, the pulse energy of mid-infrared pulses generated by IPDFG mostly scales at around tens of nJ, while the ones from DFG are more energetic, scaling at around hundreds of nJ or even μJ . The process of DFG certainly shows a better energy scalability, as discussed in section 2.2.2 and summarized in table 2.1. Finally, works that produce near single-cycle mid-infrared pulses are scarce (Fig. 2.7(b)), which emphasizes the difficulty of mid-infrared pulse compression down to near the single-cycle regime (section 2.3.2). Special approaches such as four-wave mixing with filament in gas [96], extra spectral broadening [97] or light field synthesizer [98] need to be taken to obtain sub-cycle mid-infrared pulses. Sources of intense, near single-cycle mid-infrared pulses are still rare. Hence, developing efficient mid-infrared generation schemes is of the highest priority, which brings to the scope of this thesis. In chapter 4 and 5, IPDFG and DFG are demonstrated respectively. There, we will also show the improvement in both the spectral bandwidth and the pulse energy, leading to the desired energetic, near single-cycle mid-infrared pulses.

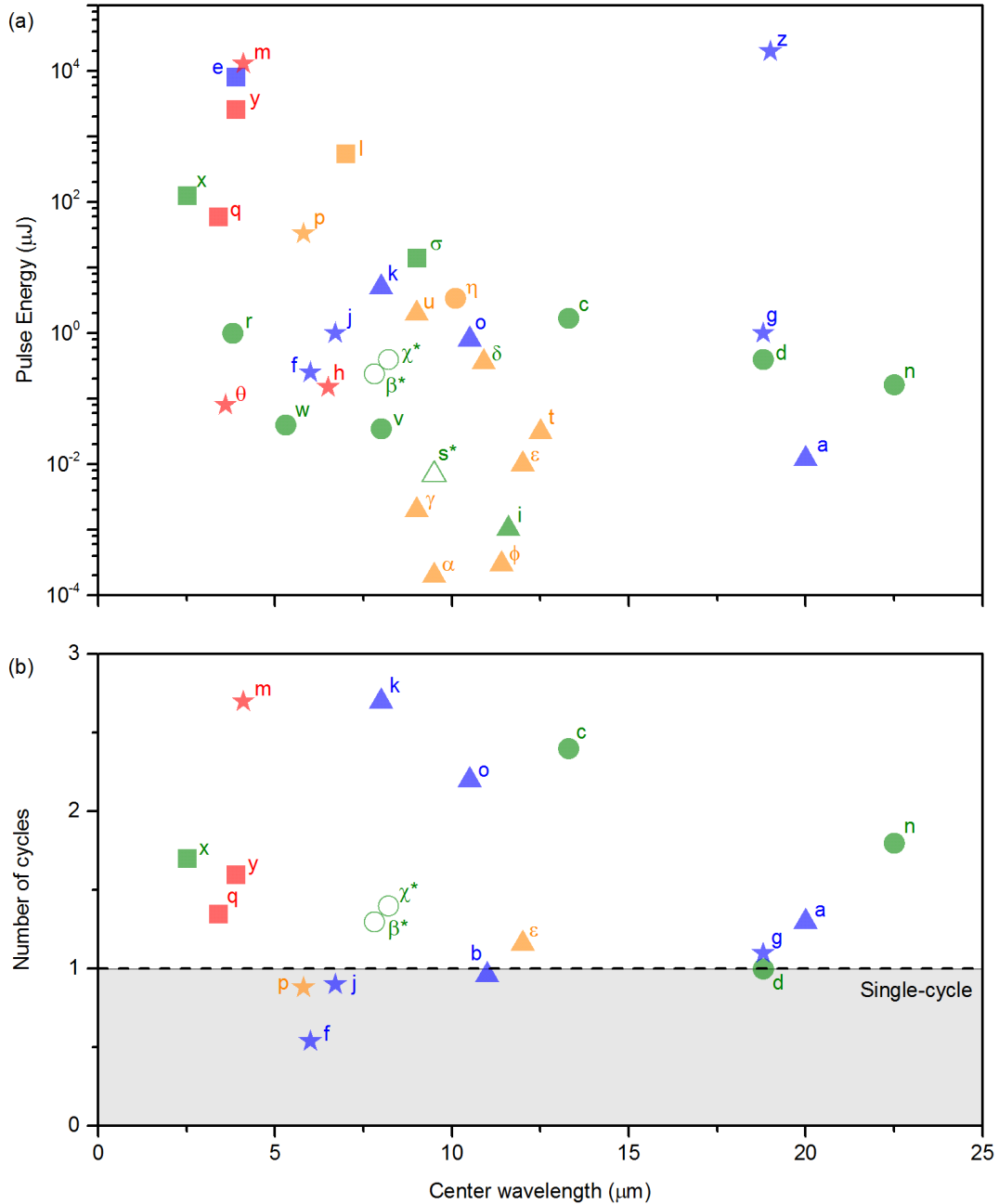


Figure 2.7: Survey on recent works on the generation of mid-infrared pulses. (a) Comparison of pulse energy. (b) Comparison of number of cycles within full-width at half maximum (FWHM) pulse width. The scattered shapes denote different generation schemes: circle, OPA/DFG; triangle, IPDFG; square, OPCPA; star, other method. The colors denote different pumping wavelengths: blue, $0.8 \mu\text{m}$; green, $\sim 1 \mu\text{m}$; orange, $\sim 2 \mu\text{m}$; red, $> 2 \mu\text{m}$. Empty scattered points: results reported in this thesis. References: a [93], b [99], c [100], d [94], e [101], f [96], g [102], h [103], i [79], j [97], k [78], l [104], m [105], n [95], o [106], p [98], q [107], r [108], s (chapter 4) [66], t [109], u [110], v [111], w [112], x [113], y [114], z [115], α [116], β^* (chapter 5) [67], χ^* (chapter 6) [68], δ [117], ε [80], ϕ [118], γ [119], η [120], σ , [121], θ , [68].

Compression of picosecond pulses from a thin-disk laser to 30 fs at 4W average power

Low frequency, single-cycle terahertz pulses had already been generated in our research group via optical rectification with 1 ps driving pulses in LiNbO₃ [122] and used for electron pulse compression [45]. One key question rose that whether we could utilize and extend the concept to further compress the electron pulses? To do so, a second compression stage would be desired [48], where a single-cycle field with higher oscillation frequency is required. This calls for pulses shorter than 1 ps, because the nonlinear polarization of optical rectification follows the evolution of the pulse envelope, and shorter driving pulse would give rise to radiation with higher frequencies. Figure 3.1 plots the rule of thumb relation between the generated low frequency and the driving pulse duration. In view of intra-pulse difference-frequency generation (IPDFG), well-compressed to near Fourier-limit pulses with a broad input spectrum are essential, because the frequency components at the spectral wings could overlap in time and interact with each other, producing the preferred single-cycle, high frequency radiation. In any case, short driving pulses are required.

Various nonlinear optical processes have been widely used for spectral broadening and pulse shortening, such as self-phase modulation in bulk materials [123] or gas-filled hollow-core fibers [124], and supercontinuum generation through filamentation in the gas [125]. In general, bulk materials possess higher nonlinearities and consequently lead to stronger broadening effect, while fiber broadening provides better power scaling and is commonly applied to high-power, high repetition-rate laser systems. However, each

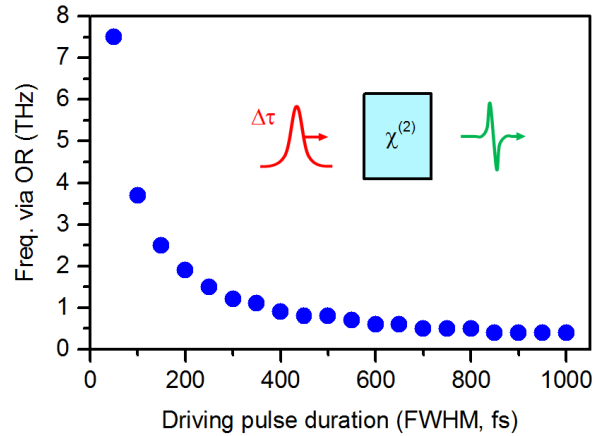


Figure 3.1: Terahertz frequency scaling with input driving pulse duration via optical rectification. $\Delta\tau$ stands for the full width at half maximum pulse duration. $\chi^{(2)}$ is the 2nd order susceptibility of a noncentrosymmetric material.

approach also has its limits: for broadening in bulk materials, the damage threshold, and the critical power¹ restrict the applicable input peak power, and for broadening in the fibers, input beam coupling is often an issue which leads to power fluctuation. In order to achieve higher broadening factor, multiple-stage broadening is usually employed, for example, spectral broadening in multiple thin-plates [126] or with cascaded hollow-core fibers [127]. It is therefore interesting to see whether the broadening concept can be extended to a mixture of spectral broadening in bulk material and fiber, taking advantage of their beneficial properties while overcoming the limits mentioned above.

This chapter demonstrate the results of a two-stage hybrid spectral broadening, which consists of a 1st stage cascaded χ^2 broadening in a beta-barium borate crystal (BBO) and a 2nd stage hollow-core fiber broadening, and post pulse compression by chirped mirrors. Pulses with full-width-at-half-maximum (FWHM) duration of 30 fs are generated. The content in the following pages (page 29-43) is also published in Optics

¹Critical power is defined as the peak power required to induce beam self-focusing in a material. Such focusing effect can cause the input beam to collapse, and the resulting laser intensity exceeds the damage threshold of the material, which eventually leads to catastrophic damage.

Express [65]²

²Author contribution: The original idea of cascaded BBO and fiber spectral broadening comes from PB. BC has contributed to the construction of 1st stage BBO broadening and built the following fiber setup with DE and TN. MK, AB, and TN conducted fiber preparation and broadening simulation. BC, TN, and MK characterized the pulses. All authors have contributed to the manuscript.

Compression of picosecond pulses from a thin-disk laser to 30 fs at 4W average power

Bo-Han Chen, Martin Kretschmar, Dominik Ehberger, Andreas Blumenstein, Peter Simon, Peter Baum, and Tamas Nagy

Abstract: We investigate two approaches for the spectral broadening and compression of 1-ps long pulses of a thin-disk laser amplifier running at 50 kHz repetition rate at 1030 nm wavelength. We find that with a single, 2.66-m long stretched flexible hollow fiber filled with xenon gas, Fourier transform limited output pulse duration of 66 fs can be directly reached. For larger pulse shortening, we applied a hybrid cascaded approach involving a BBO-based pre-compressor and a long hollow fiber. We could achieve 33-times temporal shortening of 1-ps pulses down to a duration of 30 fs at an overall efficiency of 29% with an output power level of 3.7 W. These results demonstrate the potential of stretched flexible fibers with their free length scalability for shortening laser pulses of moderate peak power.

<https://doi.org/10.1364/OE.26.003861>

© 2018 Optical Society of America under the terms of the OSA Open Access Publishing Agreement

3.1 Introduction

There is a growing demand for high-average-power, high-repetition-rate, sub-30 fs laser sources for a broad range of applications, e.g. terahertz technology, coincidence analysis in attosecond pump-probe measurements or ultrashort electron pulse generation. The laser systems for such applications are increasingly based on ytterbium-doped solid-state materials, which can be very efficiently pumped by high-power laser diodes and have low heat generation thanks to their small quantum defect. In order to achieve high average power levels, the thermal management of the active material plays a central role. Therefore, mainly three geometries have been established in this segment, which provide especially efficient cooling: thin-disk [128, 129], slab [130, 131] and fiber [132]. Although very recently direct diode-pumping has become available also for broadband Ti:Sapphire systems, due to some obstacles such as large quantum defect and sub-optimally matched pump diodes, this technology still needs to evolve [133]. Besides the many advantageous properties of ytterbium-based gain media, they exhibit on the down side a somewhat narrow bandwidth, which prohibits the direct generation of sub-30 fs pulses. Therefore, in order to reach this regime, additional pulse broadening and compression techniques need to be applied [134].

Currently, great effort is therefore being invested in the compression of few-100 μJ fiber laser pulses at high average power levels by conventional 1-m long hollow-core fibers (HCF) [135, 124, 136, 137]. For example, sub-300 fs pulses could be shortened to the duration of sub-two optical cycles at 216 W average power by using a cascaded HCF arrangement [127, 138]. Great results with cascaded arrangements were also achieved at lower pulse energies (μJ) by using photonic crystal fiber compressors [139].

For gas-filled fibers, the recent introduction of stretched flexible hollow fibers (SF-HCF) opened up new opportunities because the length of nonlinear interaction is now freely scalable [140]. This concept allows spectral broadening by up to 20-30 times, well beyond the possibilities of traditional rigid HCFs [141]. The SF-HCF technology therefore promises an appealing opportunity for directly compressing the ps, sub-ps pulses of diode-pumped solid-state (DPSS) or fiber lasers to sub-30 fs duration. We need such pulses for the efficient generation of THz radiation by optical rectification or via a non-collinear optical parametric amplifier [142], in order to compress electron pulses in time [45] for sub-cycle waveform electron microscopy [64] or for driving atomic-scale electron dynamics in condensed matter [143]. For these purposes 30 fs pulse duration is optimal in order to achieve high signal-to-noise ratio but no sample damage.

In this work we investigate how far this concept is applicable to normal laboratory-scale lasers with moderate average power levels. We introduce a new approach of cascading spectral broadening due to cascaded second-order nonlinearity in a BBO crystal and in a long SF-HCF. In this way we generate for the first time 30 fs pulses directly from picosecond pulses of a Yb:YAG thin-disk amplifier. We achieve 4 W power level at 30 fs pulse duration and at a useful, intermediate repetition rate of 50 kHz. Beyond that such pulses are attractive for applications, the results also reveal the further perspective of our approach.

3.2 Single-stage spectral broadening

A thin-disk Yb:YAG amplifier [144] delivers linearly polarized, slightly positively chirped 1-ps pulses centered at 1030 nm wavelength with an average power of 15 W at a repetition rate of 50 kHz. The somewhat unfavorable combination of rather long output pulse duration together with the pulse energy of only 300 μJ in this particular laser system, which suffered from reduced power due to Pockels cell crystal degradation, makes large spectral broadening challenging, because the peak power of 0.28 GW is rather low for HCFs.

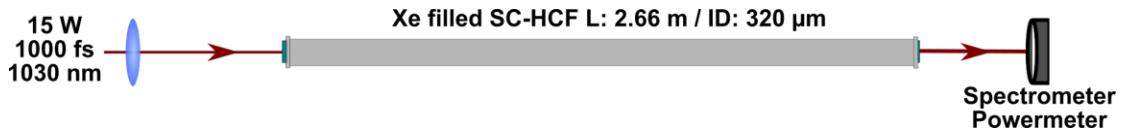


Figure 3.2: Hollow fiber compressor. ID denotes inner diameter.

As depicted in Fig. 3.2, the pulses are focused by a lens into a 2.66 m long SF-HCF with an inner diameter (ID) of 320 μm to undergo self-phase modulation. The length of the waveguide was limited by the available laboratory space, while the ID was a trade-off between waveguide transmission and achievable spectral broadening. The SF-HCF is filled with xenon at variable static pressures up to 10 bar to achieve sufficient spectral broadening during propagation. In order to estimate the performance of the experimental approach, the spectrally broadened pulses are recorded by a spectrometer as well as a power meter in order to evaluate the extent of spectral broadening and at the same time the efficiency, which are the two key parameters for applications.

Three experimental spectra, recorded at 3, 4 and 5 bar of xenon, are shown in Fig. 3.3(a). A regular spectral broadening due to self-phase modulation (SPM) is ob-

served. The spectral width increases with the accumulated nonlinear phase, that is, the B-integral which is proportional to the applied pressure:

$$B = \frac{2\pi}{\lambda_0} \int_0^L p \kappa_2 I(z) dz \quad (3.1)$$

where p is the gas pressure, κ_2 is the nonlinear refractive index of 1-bar gas having a unit of $\text{cm}^2/(\text{W}\cdot\text{bar})$, $I(z)$ is the peak intensity along the propagation and L denotes the length of the nonlinear interaction.

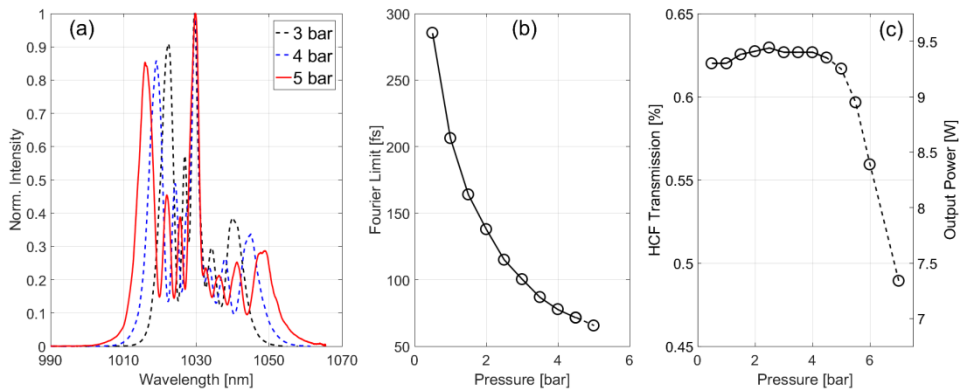


Figure 3.3: Experimental results of the SF-HCF stage. (a) Typical spectra recorded after propagation through a 2.66-m long SF-HCF filled with 3, 4 and 5 bar of xenon (black, blue, red, respectively). (b) Transform-limited pulse duration in dependence of the pressure. (c) Pressure-dependent transmission through the SF-HCF. A sharp decline of the transmission can be observed around 4.5 bar and above. This figure is slightly modify from [65]

The evolution of the corresponding Fourier-limited full-width at half maximum (FWHM) pulse duration is presented in Fig. 3.3(b). Increasing the xenon pressure inside the SF-HCF results in an increased B-integral, hence stronger self-phase modulation. The output spectrum supported a Fourier transform limited pulse duration as short as 65.6 fs at a pressure of 5 bar, which means a compression factor of 15 at a B-integral of 22.5. At this condition the maximum achievable peak power corresponds to 2.4 GW. A further increase of the pressure in the SF-HCF setup did not prove to be beneficial, because the transmission of the SF-HCF started dropping (as shown in Fig. 3.3(c)), and the output pulse energy became fluctuating. At the same time a series of weak distinct spectral features appeared on both sides of the spectrum. These fluctuations amount to roughly 10% rms, which exceeds the 1.5% rms level, which our application can tol-

erate. At 5 bar gas pressure, the transmission is 62% and the peak power (assuming compressed pulses) increased by a factor of 9.4. Nevertheless, our target pulse duration of 30 fs, which is essential for our purpose of generating multi-THz radiation by optical rectification, could not be reached.

In order to put our findings into context, Table 3.1 shows the performances of state-of-the-art single-stage HCF compressors applied to Yb-laser pulses at 1030 nm.

Table 3.1: Performance comparison for single HCF stage

| | Pulse duration [fs] | | Compression factor | HCF Transmission |
|------------------------|---------------------|---------------------|--------------------|------------------|
| | Input | Output ^a | | |
| Current work | 1000 | 66 | 15.2 | 62% |
| Rothhardt et al. [135] | 700 | 66 | 10.6 | 52% |
| Hädrich et al. [124] | 340 | 26 ^b | 13.1 | ~54% |
| Lavenu et al. [138] | 130 | 12.6 | 10.3 | 53% |
| Didenko et al. [137] | 260 | 17 ^c | 15.3 | 51% |

^aFourier transform limit of the output spectrum

^bretrieved from simulations or

^cfrom autocorrelation measurements

Here, we compare the performances of the HCF itself in the various setups, therefore either the Fourier transform limit of the output spectrum or if it is not available the pulse duration derived from simulations or from autocorrelation measurements are given. The transmission values accounts for only the waveguides without the chirp management setups. In most of previous research Yb:Glass systems were utilized as a seed source prior to spectral broadening, resulting in 300 fs long initial pulses. Our results appear to be the first report on efficient pulse compression in a HCF starting from picosecond pulse duration. Due to the advantageous geometry of our SF-HCF [141] we achieved one of the highest compression factors so far at the highest transmission level among the measurements. The performance of single-stage HCF setups will be analyzed further theoretically in the upcoming section.

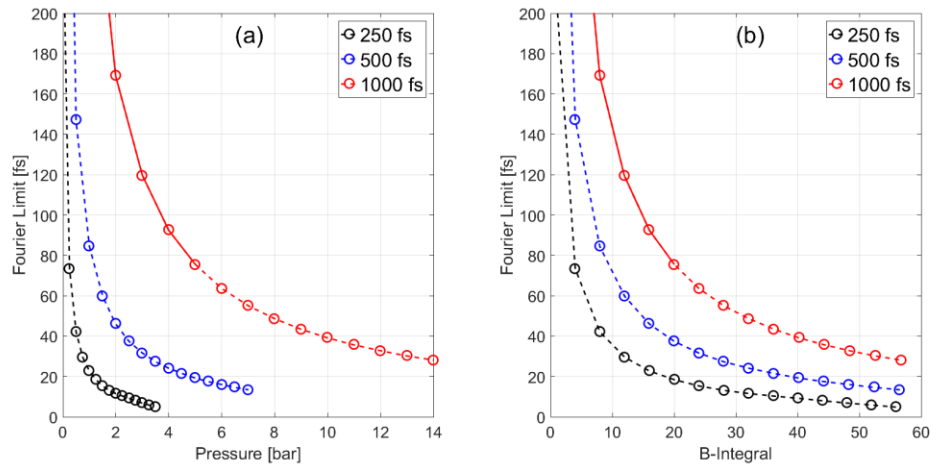


Figure 3.4: Numerical simulations. (a) Transform-limited pulse duration after propagating 0.2-mJ pulses of different durations centered at 1030-nm wavelength through a 2.66-m long HCF at various xenon pressures. (b) Same data in dependence of the B-Integral.

3.3 Simulation

In order to find out the most promising way to go down to 30 fs duration, we simulated the propagation along the HCF by applying a symmetrized split-step propagation code which solves the nonlinear Schrödinger equation taking self-phase modulation, self-steepening, linear losses and full dispersion of the gas-filled hollow waveguide into account. In the calculations, transform-limited input pulses of 1 ps, 500 fs and 250 fs duration were assumed. The spectrum at the output of the fiber was simulated for each input pulse at various gas pressures up to the critical pressure of self-focusing, in order to find the optimum. Figure 3.4(a) depicts the results, namely the transform-limited pulse durations obtained in the simulations. In Fig. 3.4(b) the same data is replotted as a function of the B-integral, which is more directly related to the general physics of the spectral broadening. According to Eq. 3.1, one can scale the B-integral either by changing the pressure or applying a longer waveguide. The red curve in Figs. 3.4(a) and 3.4(b) corresponds to the experimental case, where the solid line marks the regime of stable operation. Theoretically, one would expect to reach a B-integral of up to 55 before self-focusing sets on. This value would correspond to 30-fs transform limited pulses. However, in the experiment, we only achieved a maximum B-integral of 23 without cre-

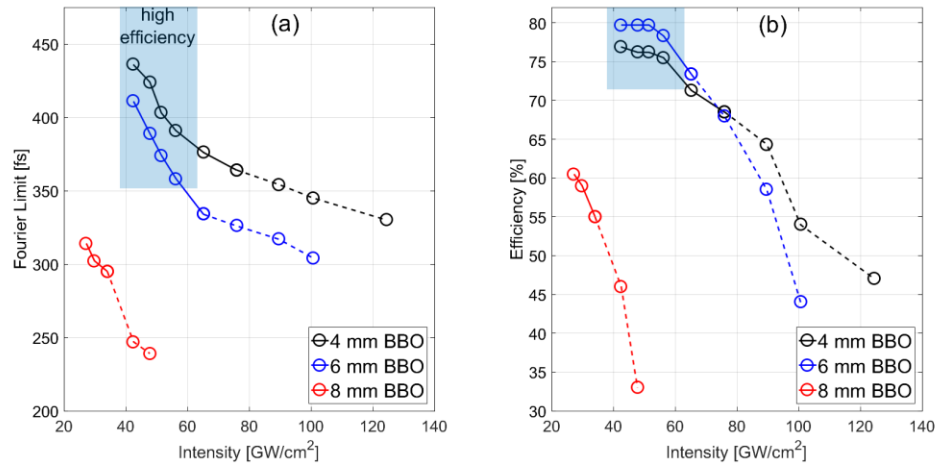


Figure 3.5: Performance of the BBO-based spectral broadening stage. (a) Fourier limit dependent on the crystal thickness. (b) Conversion efficiency as a function of pump intensity.

ating imperfect operation conditions. Nevertheless, the corresponding spectrum had 8 peaks, which is comparable to the largest spectral broadening achieved to date by a hollow-core fiber arrangement [141]. The blue and black circles in Fig. 3.4(a) and (b) suggest that starting with slightly shorter pulses can substantially help with generating shorter pulses. This prediction is tested experimentally in the next section.

3.4 Hybrid double-stage spectral broadening

According to the simulations of Fig. 3.4(a) we need to feed roughly 400-fs pulses into the SF-HCF compressor in order to reach the 30-fs regime. A straightforward way would be to use two cascaded HCFs [145] with an intermediate pulse compressor, which can dramatically improve the achievable spectral broadening, but on the other hand increases the footprint and complexity of the setup. For our proof-of-principle experiment we chose a novel approach: a hybrid two-stage arrangement, where the first stage is based on cascaded second-order nonlinearity in a beta-barium borate crystal (BBO) [146,147], not the least to obtain practical experience with this approach. In order to characterize the performance of the BBO-based spectral broadening stage, we recorded the spectrum and its transform-limited pulse duration, which was calculated for three different thicknesses

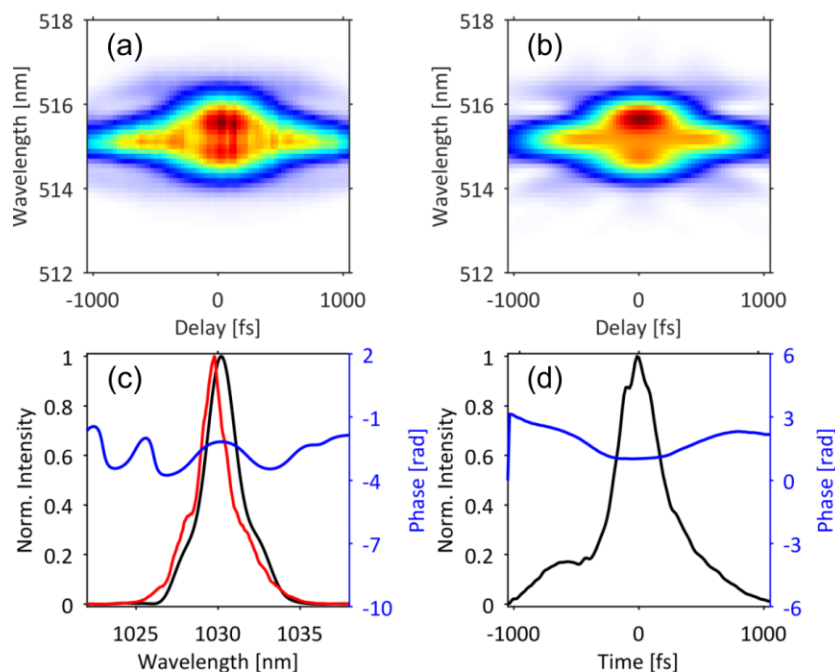


Figure 3.6: Measured pulse shape after the first compression stage. (a) Measured and (b) retrieved FROG traces. (0.82% FROG error on a 512x512 grid) (c) Evaluated spectrum and spectral phase. (d) Retrieved pulse shape with temporal phase. The pulse duration is 409 fs.

of the BBO crystal, while gradually increasing the pump intensity. Figure 3.5 summarizes the results. As expected, higher intensities result in more spectral broadening and shorter Fourier limits.

The entirely stable operation regime is again indicated by solid lines. The thicker the applied crystal, the lower was the achievable pulse duration, but also the efficiency. The lower efficiency of thicker crystals is due to the larger conversion efficiency to second harmonic, which acts as a loss for our purposes and is filtered out. We find a sweet point by using a 6 mm crystal at 50-55 GW/cm², which produced the required pulse duration at conveniently high efficiency of 75-80% and stable operation. The spectrally broadened pulses from the BBO stage optimized for 15 W input power (0.3 mJ) were compressed by a grating pair (1000 lines/mm) and subsequently characterized by a second-harmonic-generation frequency-resolved optical-gating setup (SHG-FROG), incorporating an 80- μ m thick BBO crystal for SHG generation and a wavelength-calibrated spectrometer. Figure 3.6 shows the results, indicating 409-fs pulses after the BBO stage.

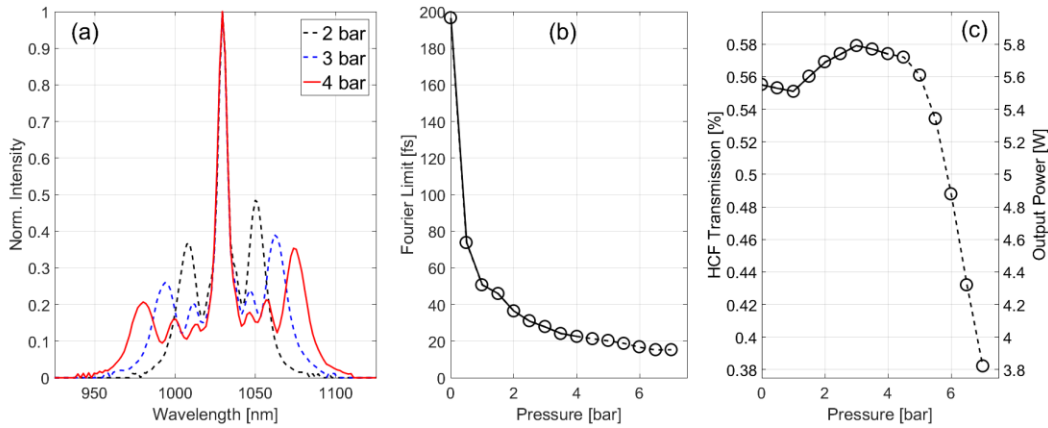


Figure 3.7: Pulse characteristics after cascaded pulse shortening in BBO and SF-HCF. (a) Typical output spectra for 2, 3 and 4 bar of xenon. (b) Fourier-limited pulse durations in dependence of the pressure, breaking into the sub-30 fs. (c) Pressure-dependent transmission through the SF-HCF. Solid lines between the data points indicate the regime of stable operation.

Finally, the compressed pulses at 10 W average power level (0.2 mJ) from the BBO stage were launched into the 2.66-m long SF-HCF of 320- μm inner diameter filled with xenon gas. The output spectrum was measured by a sensitivity-calibrated spectrometer (NIR512, Ocean Optics). Figure 6(a) shows three typical spectra recorded at 2, 3 and 4 bar pressure, respectively. Figure 3.7(b) and (c) show the corresponding Fourier-limited pulse durations (FWHM) and the efficiency of the SF-HCF in dependence of the pressure. At 4-bar pressure the transform-limited pulse duration is 22.5 fs at stable operation over the full day. The corresponding peak power reaches 4.4 GW, which is a factor of 1.8 times higher than in the single HCF stage. We compressed the output of the hybrid arrangement by a set of chirped mirrors (PC1611, Ultrafast Innovations GmbH) and characterized the final pulse shape by using the same SHG-FROG setup as described above. The full experimental arrangement is shown in Fig. 3.8.

Figure 3.9 shows a FROG measurement of the pulses compressed by the cascaded arrangement. The displayed measurement was carried out at an input power level of 12.8 W before the BBO stage, resulting in 8.5 W at the entrance of the HCF and 3.7 W average power of the compressed pulses. This corresponds to 74 μJ pulse energy and 1.5 GW peak power, which was determined by dividing the measured pulse energy by the integral of the retrieved pulse shape on ± 1.5 ps time window. The obtained pulses are well suited for further non-linear optical conversions or direct applications. The SF-HCF

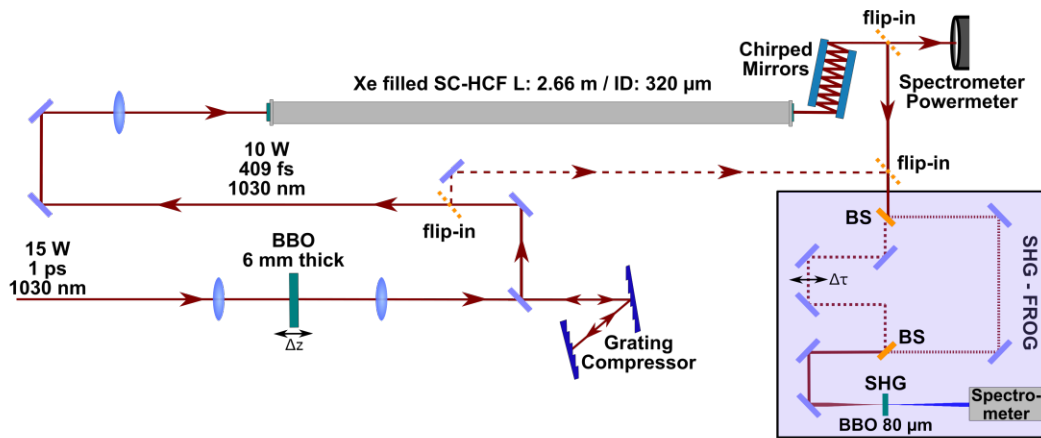


Figure 3.8: Experimental setup utilizing cascaded spectral broadening in BBO and a SF-HCF for two-stage compression of 1-ps pulses down to 30-fs duration. BS denotes beam splitter, $\Delta\tau$ time delay.

was filled with 4 bar of xenon. The FROG data reveals a 29.8-fs pulse duration very close to the transform limit of the retrieved spectrum (27.1 fs). The main peak contains 67% of the full pulse energy. We note, that the retrieved spectrum reveals a fast oscillation around the carrier wavelength of 1030 nm, which is the result of the interference of low-level pedestals of the compressed pulse after the BBO stage. This modulation has been resolved by the FROG measurement due to its large measured delay range of 2049 fs, but could not be resolved by our spectrometers (see the single peak at 1030 nm of the reference spectrum in Fig. 3.9(c) and also in Fig. 3.7(a)).

The cascaded scheme's overall compression factor is >30 in terms of pulse duration, as shown in Table 3.2. Interestingly, if considering the physics of the second stage alone, we achieved a compression factor of 13.6 in the hollow fiber, similar to the uncompressed case shown in Sect. 2. The SF-HCF's efficiency was only slightly lower than in the uncompressed case, which is attributed to the slightly lower beam quality after the BBO stage.

As it is shown in Table 3.2 our novel approach utilizing a hybrid $\chi^{(2)}$ – SF-HCF setup, shows a comparable performance to former cascaded pulse shortening results for Yb-based sources at a much reduced complexity. Again, our experiments appear to be the first reports of cascaded shortening starting with picosecond pulse durations.

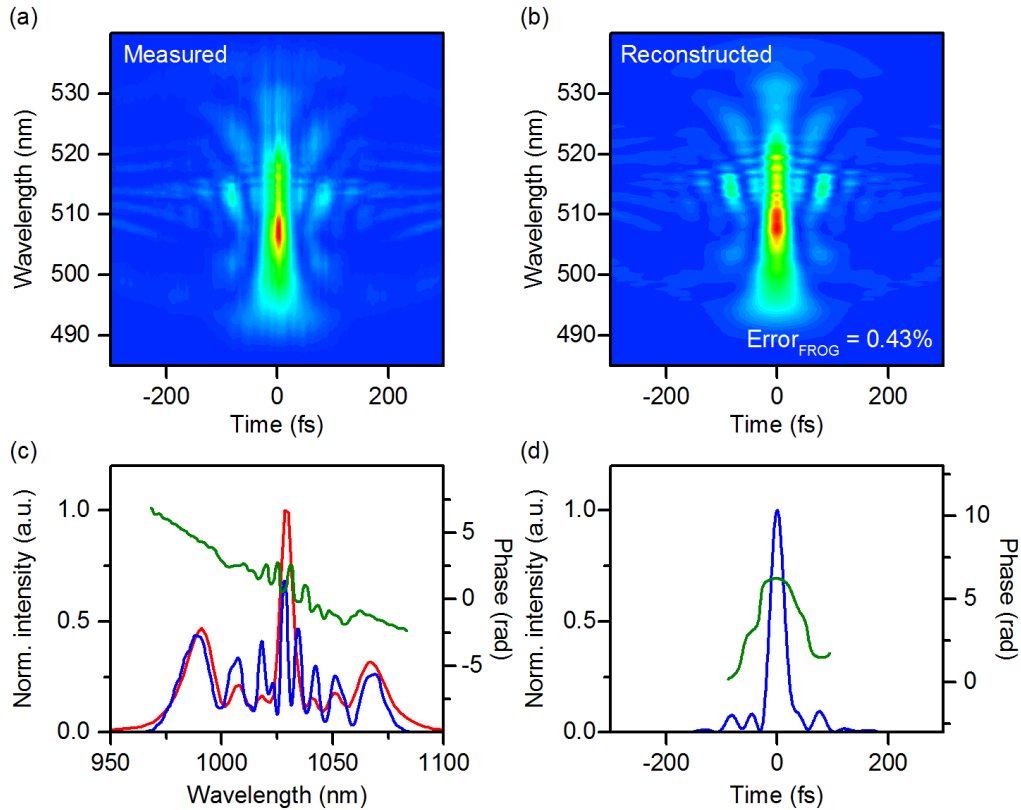


Figure 3.9: SHG-FROG measurement of the output pulses after compression by the two-stage arrangement. (a) Measured and (b) retrieved FROG traces. (0.43% FROG error on a 1024x1024 grid) (c) Evaluated spectrum and spectral phase. (d) Retrieved pulse shape with temporal phase. The pulse duration is 29.8 fs.

3.5 Conclusion

In conclusion, we investigated two approaches for the compression of 1 ps long pulses of a thin-disk amplifier running at 50 kHz repetition rate, centered at 1030 nm. We find that a single, 2.66-meter long stretched flexible hollow fiber setup can produce a substantial spectral broadening despite the unfavorably low peak power of the input pulses. It shows a good overall efficiency of 62% clearly over-performing the traditional rigid HCFs (see Table 3.1) but becomes unstable for xenon pressures above 5 bar. We introduced a hybrid cascaded approach involving a BBO-based pre-compressor and a long SF-HCF. With this novel arrangement we could achieve 33-times temporal shortening

Table 3.2: Performance comparison for cascaded compressor setups

| | Method | Pulse duration [fs] | | Compression factor | HCF Transmission |
|------------------------|----------------------|---------------------|--------|--------------------|------------------|
| | | Input | Output | | |
| Current work | $\chi^{(2)}$ /SF-HCF | 1000 | 29.8 | 33.5 | 29% |
| Rothhardt et al. [136] | HCF/HCF | 210 | 7.8 | 26.9 | 35% |
| Hädrich et al. [127] | HCF/HCF | 240 | 6.3 | 38.1 | 53% |
| Mak et al. [139] | PCF/PCF | 250 | 9.1 | 27.5 | 36% |

of 1 ps pulses down to a duration of 30 fs, which is very convenient for further experiments and applications. Although the cascaded scheme suffers from overall losses, it is capable of generating ultrashort pulses with 1.8-times higher peak power as compared to a single SF-HCF. For our purposes to generate 30 fs pulses, we find this solution as a good compromise, because the first BBO stage does not increase the complexity of handling and alignment requirements, like two-HCF setups would do. If even shorter pulses are required, one can sacrifice the simplicity and switch to SF-HCF / SF-HCF cascading having the potential for sub-2-cycle pulse compression. The compressed 30 fs pulses have been successfully applied for the generation of THz radiation [66].

Acknowledgment

We thank Ferenc Krausz for general support.

Efficient middle-infrared generation in LiGaS₂ by simultaneous spectral broadening and difference-frequency generation

In the last chapter, we demonstrate the generation of 30-fs pulses via a hybrid 2-stage spectral broadening approach. With such pumping pulse duration, the bandwidth of the corresponding spectrum supports a frequency difference of around 30 THz, and therefore the generation of mid-infrared pulses at around 30 THz can be expected through intrapulse difference-frequency generation (IPDFG). Finding an appropriate nonlinear optical crystal becomes critical. Several factors need to be considered: (1) the crystal must be transparent for the spectral range of interest. (2) the phase-matching condition must be fulfilled and, (3) the bandgap of the nonlinear crystal should be larger than twice of the input photon energy so that thermal damage caused by two-photon absorption (TPA) can be avoided.

A figure of merit, defined as d^2/n^3 (pm^2/V^2) where n is the refractive index (unitless) and d is the averaged nonlinearity (pm/V), is often used to describe the conversion efficiency of a particular crystal. In the work of V. Petrov [148], Fig. 2 shows a collection of various nonlinear crystals with their figure of merit and transparency range. Among them, LiGaS₂ (LGS) exhibits one of the lowest figure of merit. Nonetheless, it satisfies all the requirements mentioned above: the transparency range covers from 0.32 μm to 11.6 μm , the phase-matching condition can be fulfilled (roughly 7.5-10 μm , see Fig. 4.1) when pumped by 1.03 μm laser and the bandgap (4.15 eV) is more than three times

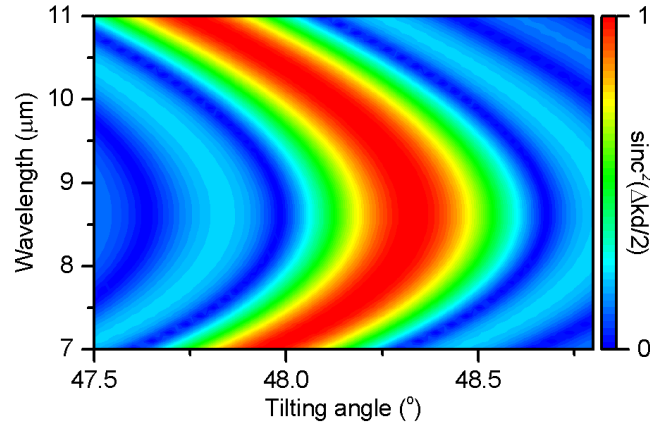


Figure 4.1: Phase-matching map for a 4-mm LGS crystal pumped by 1.03 μm laser. At an angle of 48.2°, the phase-matching function is flat and broad, ranging from 7.5 μm to 10 μm . Δk , phase-mismatch between pump, seed and idler; d , crystal thickness (4 mm)

larger than the photon energy of 1.03 μm (1.2 eV). Therefore the LGS crystal makes a suitable candidate for generating mid-infrared pulses at the desired wavelength (10 μm).

In this chapter, we directly apply the 30-fs pulses (chapter 3) and use the LGS crystal as the nonlinear medium to demonstrate mid-infrared generation by IPDFG. Also, the mechanism behind type II phase-matched¹ IPDFG in a long crystal is discussed and also revealed experimentally. The interplay between spectral broadening (self-phase modulation, SPM), pulse walk-off and dispersion makes it useful for generating high power, broadband mid-infrared spectrum. The results shown in this chapter (page 48-57) are also published in Optics Letters [66].²

¹Depending on the crystal birefringence and the polarization states of the interacting pulses, the phase-matching condition can be categorized into two classes: type I (o-pol. + o-pol. \rightarrow e-pol., or e-pol, + e-pol. \rightarrow o-pol.) and type II (o-pol. + e-pol. \rightarrow o-pol., or o-pol, + e-pol. \rightarrow e-pol.)

²Author contribution: BC and TN have dedicated to the ultrashort pulse generation with fiber and chirp mirrors. BC has performed all measurements under the supervision of PB. The physical mechanism behind the whole process was discussed and proposed by BC and PB. All authors have contributed to part of the writing of the manuscript.

Efficient middle-infrared generation in LiGaS₂ by simultaneous spectral broadening and difference-frequency generation

Bo-Han Chen, Tamas Nagy and Peter Baum

Abstract: We report a surprisingly broadband and efficient mid-infrared pulse generation in LiGaS₂ (LGS) by invoking a simultaneous interplay of intra-pulse difference frequency generation, self-phase-modulation and dispersion. This cascaded mechanism expands the output bandwidth and output power at the same time. With 30-fs driving pulses centered at 1030 nm wavelength we obtain a broadband middle-infrared (MIR) spectrum of 8-11 μm with an LGS crystal as thick as 4 mm, which is 8 times longer than the walk-off length.

<https://doi.org/10.1364/OL.43.001742>

© 2018 Optical Society of America

Short and broadband optical pulses at midinfrared (MIR) or multiterahertz (THz) frequencies have a key importance in various research fields. They are, for example, essential for molecular fingerprint spectroscopy [8, 9, 149], all-optical electron pulse compression [45], and high-field experiments in condensed matter [29, 30, 150]. A common way to produce MIR few-cycle pulses is intrapulse difference-frequency generation (DFG) [79, 78, 95, 106] in a nonlinear crystal. This nonlinear optical mechanism is related to optical rectification and produces broadband, low-frequency electromagnetic radiation at a center frequency that is approximately given by the available spectral width of the pump pulses.

In practice, however, there are not many optical materials with high nonlinear coefficients in the relevant spectral ranges, and often there is also velocity mismatch between the MIR radiation and driving optical pulses. One of the more favorable materials is LiGaS₂ (LGS). Although its effective nonlinearity is rather low ($d_{\text{eff}} = 5.8 \text{ pm/V}$), the material has on the other hand a wide transparency range (about 0.32 to 11.6 μm), a high damage threshold, and a particularly weak two-photon absorption when excited with femtosecond pulses at $>600 \text{ nm}$ wavelength (bandgap 4.15 eV). However, temporal walk-off between the two required driving polarizations along the ordinary (o) and extraordinary (e) axes limits the overall efficiency and spectral bandwidth of the MIR output. For example, for 30-fs driving pulses at 1030 nm wavelength, there is less than 0.45 mm of LGS crystal that will be efficient. The conversion efficiency suffers accordingly.

To our surprise, we found in experiments with the setup depicted in Fig. 4.2 that even with an eight times longer crystal than the walk-off length, MIR generation is still highly efficient and particularly broadband. In this Letter, we argue that the temporal walk-off is continuously compensated by nonlinear spectral broadening and dispersion of the driving pulses during propagation, in such a way that the high-frequency components of the extraordinary/faster part of the pump pulse and the low-frequency component of the ordinary/slower part of the pump pulse have a continuous overlap all the time.

This mechanism (depicted in the lower part of Fig. 4.2) allows using substantially longer crystals than expected, for example 4 mm instead of 0.45 mm at our experimental conditions, in order to simultaneously achieve higher MIR frequencies and more output power. The following data shall support this interpretation and establish the concept for future applications.

In the experiment (see Fig. 4.2), 1.0-ps pulses from a regenerative thin-disk laser [144] (1030 nm wavelength, 330 μJ pulse energy, 50 kHz repetition rate, 16.5 W output average power) are first compressed via cascaded $\chi^{(2)}$ broadening [146, 147, 151, 152] in a β -barium-borate (BBO) crystal and a grating compressor (1000 lines/mm) to a pulse duration of 400 fs. In a second stage, these 400-fs pulses are coupled into a 2.7-m long stretched flexible hollow fiber [140, 141] with 320 μm inner diameter filled with 4 bar xenon; these results are reported in more detail elsewhere [19]. The spectrally broadened output pulses are compressed by 20 bounces on double-angled chirped mirrors down to 30-fs pulse duration. Results of second-harmonic generation frequency-resolved optical gating (SHG-FROG, error 0.65%) are reported in Fig. 2 and reveal 30-fs pulses with low pedestals in time. More than 60 μJ of pulse energy or 3W of average power was

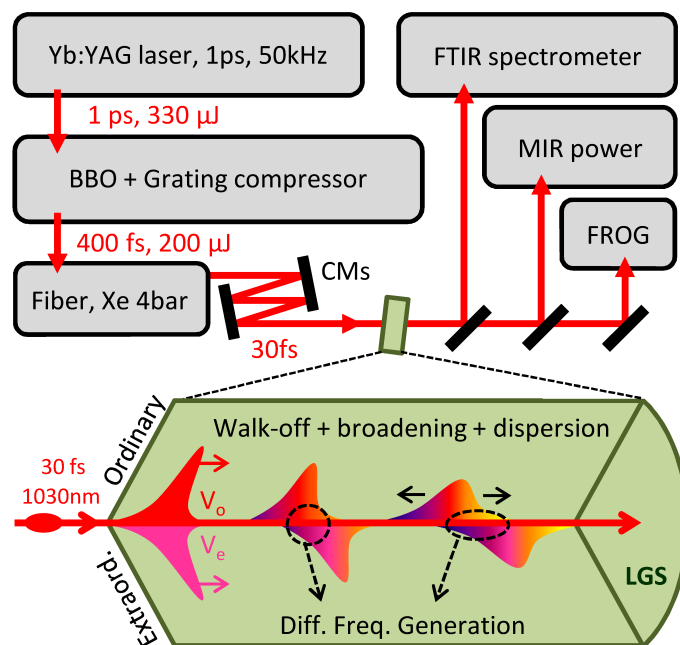


Figure 4.2: Experimental setup and concept for simultaneous, cascaded spectral broadening and intrapulse DFG. Yb:YAG, ytterbium-doped yttrium aluminum garnet; FTIR, Fourier-transform infrared spectroscopy.

available in this way. A maximum pulse energy of $20 \mu\text{J}$ is used in all the measurements described in order to avoid crystal damage. These 30-fs pulses have a spectrum from 970 to 1095 nm at 1% level. Difference frequency generation between these extreme components should allow producing MIR pulses with a spectrum extending down to $8.5 \mu\text{m}$.

We begin our report on the physics within LGS by measuring the output MIR spectrum by a Fourier-transform spectrometer (L-FTS, LASNIX GmbH) in dependence of the input power with a 4-mm long LGS crystal ($\theta = 90^\circ$, $\phi = 38.5^\circ$, Ascut Ltd.). In order to satisfy type II phase matching ($e + o \rightarrow e$), the crystal is rotated around the beam axis by 45° in such a way that the input p-polarization sees the two crystal axes (e and o) with equal contribution. According to the linear-optical walk-off between the two active crystal axes, about 67.4 fs/mm , this crystal is eight times longer than useful for our 30-fs pump pulses (see Fig. 4.3).

Figure 4.4(a) shows the MIR spectrum generated in the 4-mm LGS crystal as a function of increasing input power. While there is the expected increase of output power,

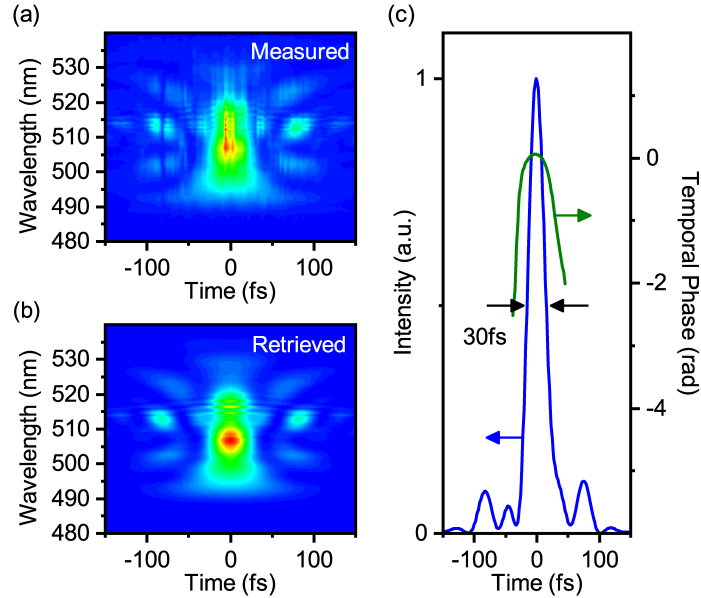


Figure 4.3: SHG-FROG of the driving 30-fs laser pulse from a hollowcore fiber. (a) Measured FROG trace. (b) Retrieved FROG trace. (c) Retrieved temporal pulse shape. FROG error, 0.65%.

the striking observation is a substantial reshaping of the output spectrum. The intensity increase in the short-wavelength region (7–8.6 μm) is much stronger than in the longer-wavelength part [Fig. 4.4(a), black arrows]. This is a first strong indication that more nonlinear processes than only DFG or optical rectification are at work.

More direct evidence for the above-mentioned mechanism is reported in Fig. 4.4(b). We measured the spectrum of the 30-fs pump pulses after propagation through four different thicknesses of LGS crystal at otherwise identical conditions (1 W, 130 GW / cm²). The spectrum of the transmitted pulses becomes symmetrically broader on both sides for longer crystals. This excludes substantial influences from cascaded difference frequency mixing [153] and rather indicates the presence of self phase modulation [154, 155]. The broadening starts to saturate at around 4 mm thickness [compare in Fig. 4.4(b) the magenta and green traces], because the dispersion of the optical pulses (300 fs² / mm) eventually lowers their intensity.

Having a broadened pump spectrum is still not yet enough to explain the unusually broadband MIR spectra of Fig. 4.4(a); the new components also need to overlap in time. Figure 4.5 shows the results of SHG-FROG measurements of the pump pulse shapes after passage through the 4-mm LGS crystal. The FROG device is based on

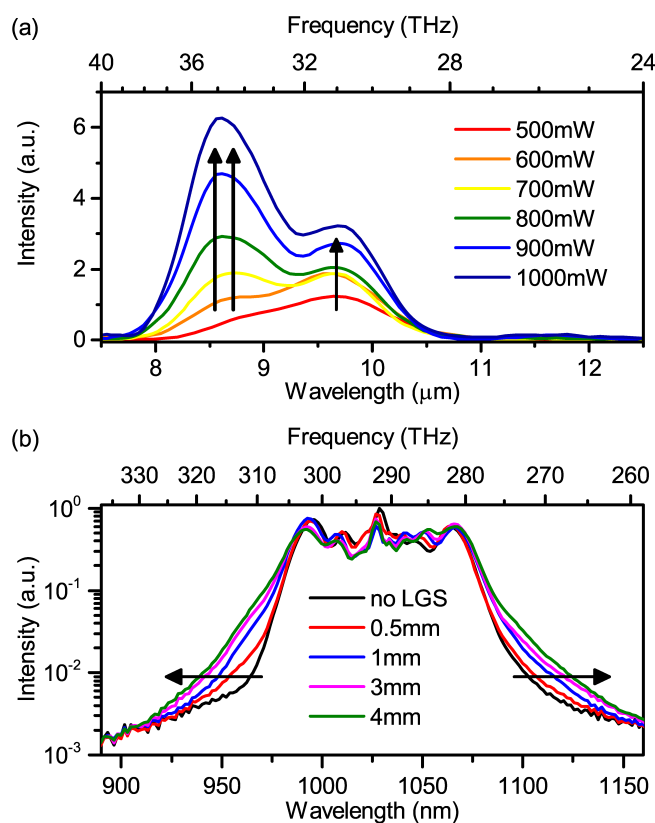


Figure 4.4: Evidence in the spectral domain. (a) MIR spectra with different input power. (b) Optical spectrum for different thicknesses of the LGS crystal.

a 80- μm -thick BBO crystal that is oriented such that the projection of both output polarizations of the LGS crystal are measured (optical axis at 45° to the LGS axis) simultaneously. Figure 4.5(a) shows a measurement at very low input power (10 mW), where no spectral broadening can occur. We see that the pump pulses split in time into two distinct envelopes, due to the expected walk-off in birefringent LGS, as explained previously. The measured walk-off is about 300 fs for our crystal (black arrow). The two polarizations are fully separated after the LGS, and at the later part of the crystal there is no possibility for DFG. Figure 4.5(a) also reveals directly in the time domain the expected linear-optical dispersion of each crystal axis, which transforms the double-lobed 30-fs pump pulse spectrum [compare Fig. 4.4(b)] into the measured double-lobed time structures.

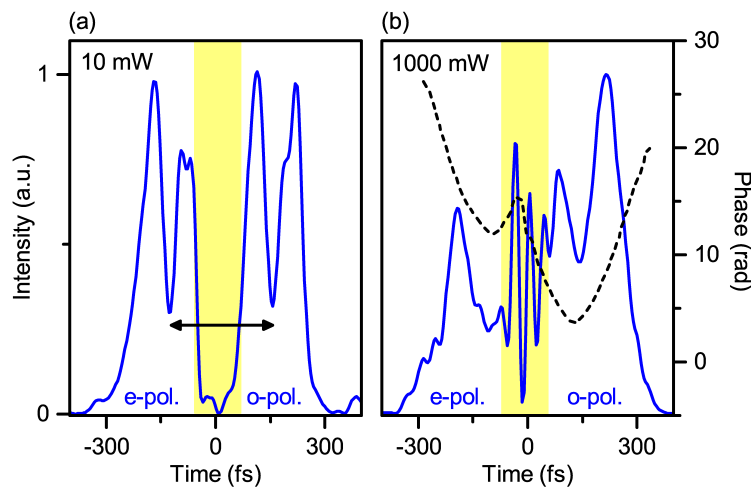


Figure 4.5: Evidence in the temporal domain. Retrieved FROG pulse shape with an input power of (a) 10 mW and (b) 1000 mW. Yellow, region around time zero. Dashed line, retrieved phase.

In contrast, when a higher input power of 1 W, 130 GW/cm² is applied [see Fig. 4.5(b)], the mechanism of Fig. 4.2 kicks in and the two parts of the pump pulses suffer broadening and more dispersion in the crystal. As seen in Fig. 4.5(b), both polarizations become longer in time. Intriguingly, there is now still temporal overlap, even interference, after passage through the crystal. The two polarizations from the two LGS axes are still interacting with each other even after 4 mm of LGS. Because of the positive dispersion experienced by the optical pulse, the blue part of the e-polarized pulse overlaps with the red part of the o-polarized pulse in a very beneficial way for high-frequency MIR generation. The FROG's beamsplitter had different transmission for e- and o-polarization, and this effect was corrected in Fig. 4.5. The period (peak to peak) of the oscillation in the overlapping region (yellow) is roughly 30 fs and shows the coherence between the different polarization components after 45° selection.

In a final measurement, we compared the overall performance of 1-mm and a 4-mm LGS crystals. Figure 4.6(a) shows the power dependence of these two crystals. These data were obtained by measuring the power after an uncoated germanium (Ge) near-infrared filter and corrected by taking Fresnel losses into account (40% transmission for normal incidence). As one would expect from a $\chi^{(2)}$ process, a quadratic-like power dependence is measured, but the 4-mm crystal performs substantially better (0.037% power conversion, 0.32% quantum efficiency). This conversion efficiency is five times lower than previously reported at three times higher peak intensity [79]. Therefore, if

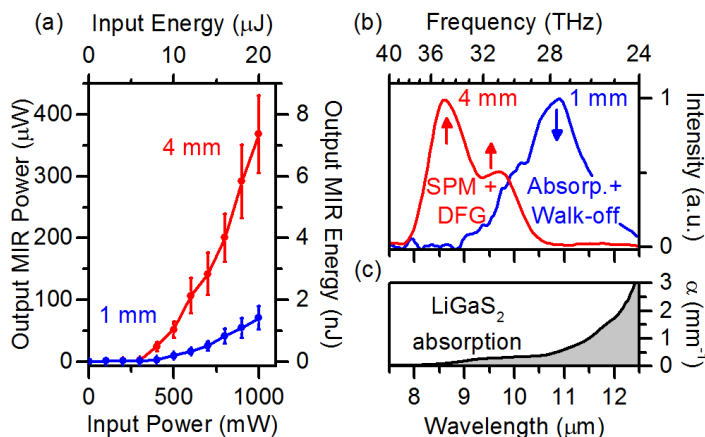


Figure 4.6: Overall performance. (a) Output power with a 1-mm (blue) and a 4-mm (red) LGS crystal. (b) MIR spectrum generated from a 1-mm (blue) and a 4-mm (red) LGS crystal. (c) Measured linear absorption curve of our LGS material.

assuming a quadratic intensity dependence of the overall cascaded mechanism, our 4-mm crystal performs better. We did not want to apply the audacious 350 GW/cm^2 of [79] to our crystals, in order to avoid damage. Nanojoule pulse energies and MV/m E-fields, as now available at $7.5\text{--}11 \mu\text{m}$, are sufficient for our intended applications in femtosecond and attosecond electron microscopy [45, 46, 64], but also for many other applications.

Figure 4.6(b) shows the two MIR spectra at 1W pump power. For the 1-mm LGS crystal, there are no high-frequency components below $9 \mu\text{m}$ wavelength and the strongest output is around $10.5 \mu\text{m}$. In contrast, for the 4-mm LGS, there are substantially more high-frequency components at wavelengths down to $7.5 \mu\text{m}$. Figure 4.6(c) shows our LGS crystals' absorption curve, measured with a FTS (Bruker Corp.). The crystals have a substantial absorption above $11 \mu\text{m}$, explaining the reduction of low-frequency components in case of the 4-mm crystal.

Overall, there emerges the picture that was outlined above (see Fig. 4.2, lower part). At the beginning of the crystal, the pump pulses decompose into two orthogonally polarized parts along the two LGS axes. Both parts are stretching in time and also temporally walk away from each other due to dispersion and group velocity mismatch. In the first $0.5\text{--}1 \text{ mm}$, nonlinear spectral broadening and absorption are not yet substantial. The resulting MIR spectrum is shown as the blue curve in Fig. 4.6(b). As the pump pulses propagate further into the 4-mm crystal, self-phase modulation leads to broader

spectra and the dispersion together with walk-off keep the bluest and reddest parts in continuous overlap. Consequently, more MIR power is produced and the shortest MIR wavelengths are created preferentially, while wavelengths beyond 11 μm are gradually absorbed.

We conclude with three remarks. First, in a way, our reported combination of nonlinear-optical self-phase modulation with nonlinear-optical difference-frequency mixing is one more example of cascaded or multiprocess nonlinear optics [156–158]. Second, it seems clear now why somewhat broader MIR spectra than expected have been reported before [79]. Third, there should be other optical materials for which this picture also applies, namely whenever self-phase modulation and dispersion create enough temporal effects to compete with walk-off. Novel optical applications might be ahead.

Octave-spanning single-cycle middle-infrared generation through optical parametric amplification in LiGaS₂

Previously, we have seen mid-infrared radiation generated through IPDFG in an LGS crystal. However, despite generating a broadband mid-infrared spectrum (7.5-11 μm), the output energy does not support the necessary field strength for driving high-field experiments. As pointed out in chapter 2.2.2, IPDFG process only utilizes the spectral wings of the driving pulse (see Fig. 5.1). Hence the majority of the input power is not in use and might even cause thermal damage to the crystal, and power scaling is limited. In order to achieve higher power and broader mid-infrared spectrum, an even shorter driving pulse with high power is required, which will add more complexity to the experiment, leading to lower efficiency and occupying more space.

In this chapter, we show another approach, namely DFG, to produce high power, near single-cycle mid-infrared pulse. For the seed pulse generation, we employ non-collinear optical parametric amplification (NOPA) to have full control of the seed pulse: (1) by adding different amount of glasses, we are able to manipulate the bandwidth of the seed spectrum and thus the final mid-infrared spectrum, as depicted in Fig. 5.2(a)-(c), and (2) by selecting the spectral region to be amplified in the NOPA, we can also flip the sign of dispersion of the seed pulse (see Fig. 5.2(d) and (e)), and as a consequence change the sign of dispersion of the mid-infrared pulse. Combining these two advantageous features, we can equivalently engineer the dispersion of the mid-infrared pulse. This

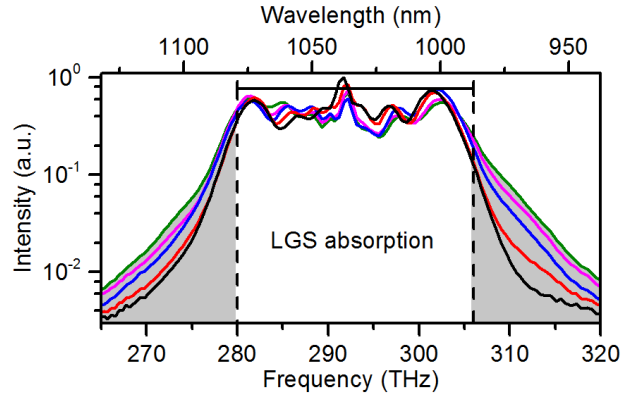


Figure 5.1: Spectral components that are in use for IPDFG. The gray area shows the useful part in the driving spectrum, while the white part generates mid-infrared that enters the absorption region of the LGS crystal. This figure contains the same data as in Fig. 4.4.

approach considerably reduces the difficulties of mid-infrared pulse compression and makes it possible to be achieved by only bulk materials. The content shown in this chapter (page 62-82) is also published in Optics Express [67].¹

¹ER and PB proposed the original idea and design of the experiment. EW and BC built NOPA system and the setup of ultrashort gating pulse for electro-optic sampling (EOS). YM and BC did both the design and construction of EOS setup and finalizing the post-retrieval algorithm. Also, the improvement of output power and overall stability were made by YM and BC under PB's guidance. All measurement performed in the publication were carried out by EW, YM, and BC. All authors have devoted to the discussion and the writing of the manuscript.

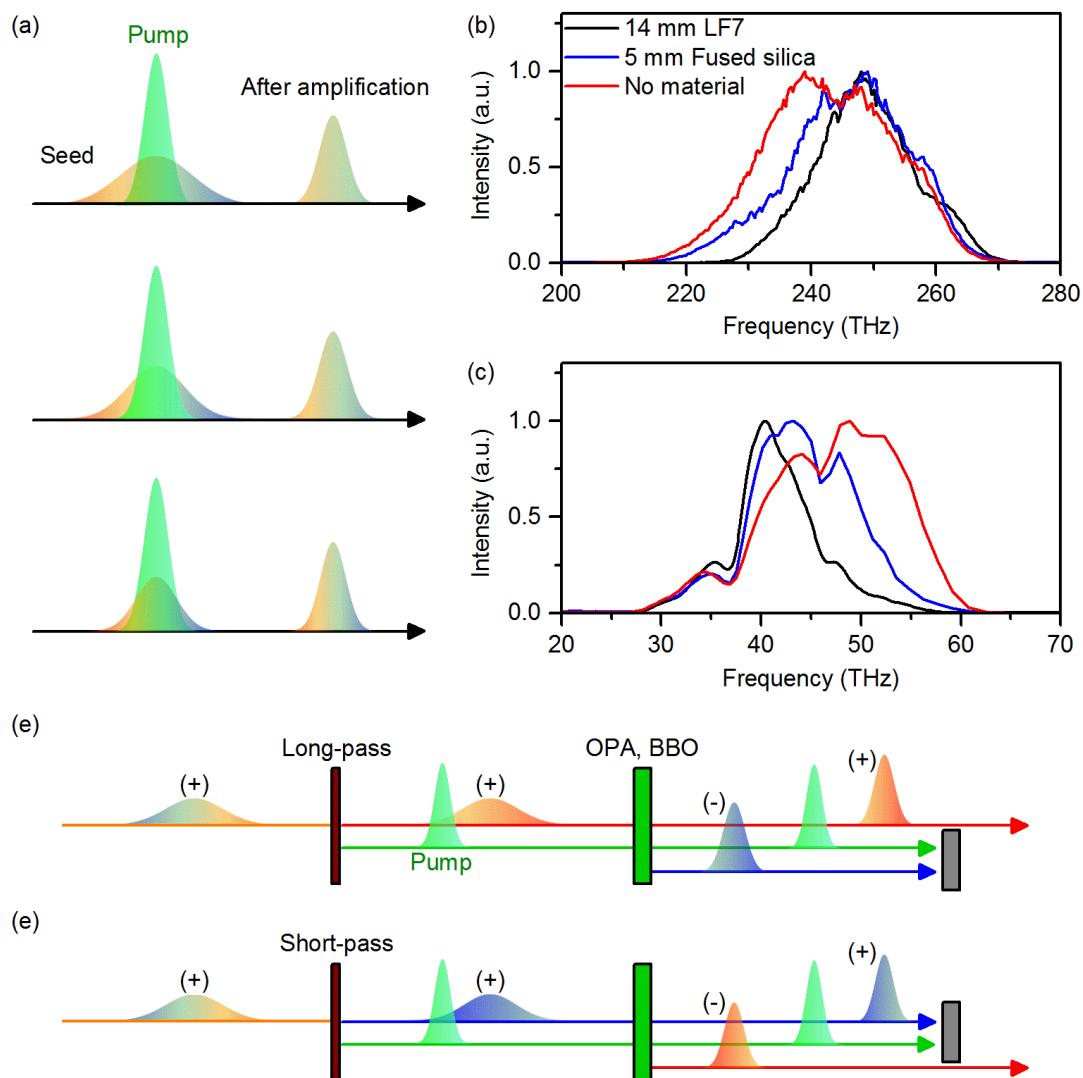


Figure 5.2: Bandwidth and phase control of seed and the generated mid-infrared spectrum. (a) Controlling the amplified bandwidth by managing the dispersion of the seed pulse. The longer the seed pulse is chirped, the less seeding component will be amplified within the finite temporal overlap with the pump pulse. (b) Experimentally measured seed spectrum from the same NOPA described in this chapter. As illustrated in (a), the less dispersing material, the broader the spectrum becomes. (c) The resulting mid-infrared spectrum. The spectrum gets broader towards higher frequency part because the seed spectrum is broader towards lower frequency side, leading to larger frequency difference between the seed and the pump. (d) When amplifying the red part of the seed pulse in the NOPA, the seed pulse remains positively chirped. (e) When amplifying the blue part of the seed pulse, a negatively chirped pulse with a spectrum of the red part would be generated due to the nature of difference frequency generation. A second amplification would be required to amplify this pulse in order to get a negatively dispersed seed pulse.

Octave-spanning single-cycle middle-infrared generation through optical parametric amplification in LiGaS₂

Bo-Han Chen, Emanuel Wittmann, Yuya Morimoto, Peter Baum and
Eberhard Riedle

Abstract: We report the generation of extremely broadband and inherently phase-locked mid-infrared pulses covering the 5 to 11 μm region. The concept is based on two stages of optical parametric amplification starting from a 270-fs Yb:KGW laser source. A continuum seeded, second harmonic pumped pre-amplifier in β -BaB₂O₄ (BBO) produces tailored broadband near infrared pulses which are subsequently mixed with the fundamental pump pulses in LiGaS₂ (LGS) for mid-infrared generation and amplification. The pulse bandwidth and chirp is managed entirely by selected optical filters and bulk material. We find an overall quantum efficiency of 1% and a mid-infrared spectrum smoothly covering 5-11 μm with a pulse energy of 220 nJ at 50 kHz repetition rate. Electro-optic sampling with 12-fs long white-light pulses directly from self-compression in a YAG crystal reveals near-single-cycle mid-infrared pulses (32 fs) with passively stable carrier-envelope phase. Such pulses will be ideal for producing attosecond electron pulses or for advancing molecular fingerprint spectroscopy.

<https://doi.org/10.1364/OE.27.021306>

© 2019 Optical Society of America under the terms of the OSA Open Access Publishing Agreement

5.1 Introduction

Few-cycle, high-field and phase-stable laser pulses in the mid-infrared (MIR) range of the optical spectrum are essential for many applications [159, 52, 160], especially for strong-field physics in solids [30], all-optical electron pulse compression [45] or molecular fingerprint spectroscopy [8, 9, 12, 161]. Direct broadband laser sources are rare in the MIR due to lack of suitable materials. Researchers are therefore invoking nonlinear optical conversions, for example difference frequency generation or optical rectification in nonlinear crystals [101, 107, 110, 119] such as GaSe or AgGaS₂ [100, 93], filaments [96, 105] or plasmas [115]. A quite new material is LiGaS₂ (LGS) [79, 95] which offers a broadband transparency range (0.32 – 11.6 μm) and a large bandgap of ~ 4 eV that leads to very weak two-photon absorption for Ti:sapphire-based (~ 800 nm) or Yb-based (~ 1030 nm) laser pulses. LGS consequently combines a sufficiently large $\chi^{(2)}$ with a comparatively high optical damage threshold, especially at high repetition rates. The proper comparison of the various crystals requires simultaneous consideration of the amplification bandwidth, i.e. the useable crystal thickness, and the effective nonlinearity. This is where LGS performs best.

Historically, the relevant $\chi^{(2)}$ processes are classified as difference frequency generation (DFG), optical parametric amplification (OPA) and optical rectification (OR). In DFG, two waves with a difference of the carrier frequency equal to the desired MIR frequency are overlapped in a suitable nonlinear crystal to generate the MIR. It is often assumed that the photon number of the weaker of the two beams limits the conversion. However, an intense short wavelength pump combined with a weak longer wavelength seed (signal) can lead to a much higher number of difference frequency (idler) photons as signal photons supplied. This is then the regime of OPA: the signal simultaneously gets amplified. In OR, both generating waves are taken out of one common pump beam if the bandwidth of this pulse is broader than the desired MIR frequency.

There are a number of challenges when transferring these DFG/OPA and OR concepts to the MIR. A broad phase matching and a proper temporal overlap of all involved spectral components are needed for efficient conversion. The width and form of the generating spectra and the output spectrum have to be carefully controlled to match the transparency range of the crystal in order to avoid heating and destruction. Such damage was reported in LGS crystals in earlier work [112]. Last but not least one needs to

avoid any other nonlinear effects that inherently occur at the high intensities, e.g., self- or cross-phase modulation and Kerr lensing.

In this work, we report an OPA concept for producing an octave-spanning MIR spectrum and near-single-cycle pulses with high peak power and locked carrier-envelope phase while avoiding all of the above-mentioned problems. The work builds on our earlier reports about a related concept to generate CEP stable few cycle pulses in the 2 to 5 μm range [142,157,162,163]. We combine a noncollinear OPA (NOPA) pumped by the second harmonic of a 1026 nm Yb:KGW-based pump laser with a collinear amplifier pumped by the residual fundamental pulses. The amplified seed pulse minimizes the pump intensity and power needed for the final MIR generation and provides the necessary tailored spectrum needed for optimum efficiency and for avoiding damage. In this way damage of the LGS crystal is avoided. A rather thin crystal allows the use of a fairly small spot on the crystal that avoids issues with crystal inhomogeneity. The chirp is managed entirely with bulk materials and without the need for prism or grating sequences [164].

Our approach combines a set of straightforward and dedicated nonlinear optical frequency conversion stages for a stepwise and flexible control of power, phase, beam profile and stability. As compared to the currently popular spectral broadening of the full pump laser output in various media, we use just a small amount of light to obtain the necessary broadening and frequency shift in a bulk YAG crystal and subsequently add power by a first OPA stage. This concept allows to control and adjust the pulses' spectral and dispersive properties without the need for specially tailored chirped mirrors or luck with the properties of the nonlinear process. By performing the final MIR generation with two well-controlled and clean pulses, we avoid detrimental couplings between bandwidth, efficiency, fluctuations and spatial beam quality and can control the interplay between them for meeting the requirements of the following experiments. With only one more nonlinear conversion step as compared to spectral broadening and OR, the overall energy conversion efficiency is quite competitive.

5.2 Experimental setup

Figure 5.3 depicts the experiment that covers an area of less than 1 m^2 . An Yb:KGW laser system (Pharos PH1-20, Light Conversion) delivers 270-fs pulses at a central wavelength of 1026 nm at a selected repetition rate of 50 kHz. A pulse energy of 187 μJ is

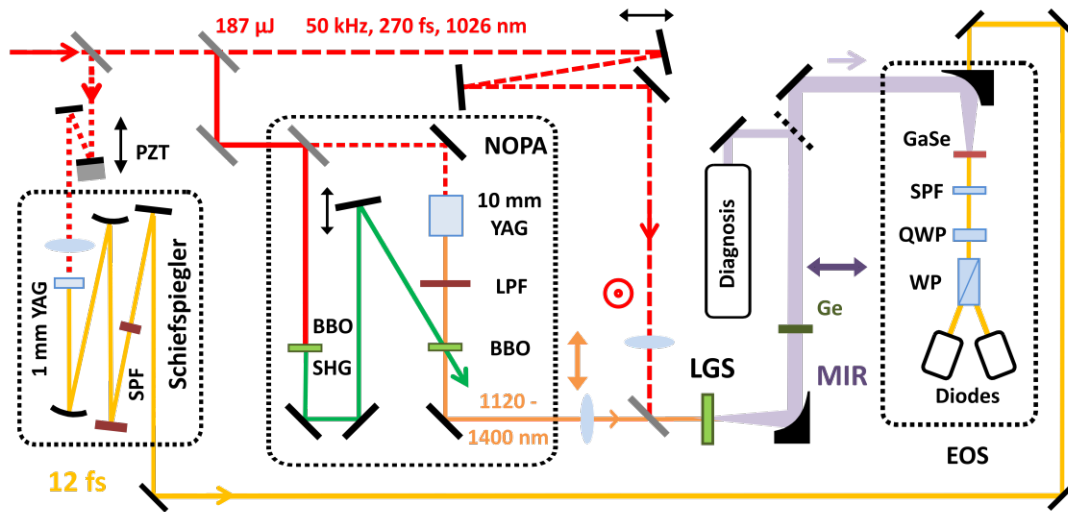


Figure 5.3: Experimental setup. BBO, β -BaB₂O₄ crystal; LGS, LiGaS₂ crystal; YAG, Y₃Al₅O₁₂ crystal; Ge, Germanium plate with 4.5 μ m LP filter coating; SHG, second-harmonic generation; LPF, longpass filter; SPF, shortpass filter; PZT, piezo electric transducer; EOS, electro-optic sampling; QWP, quarter-wave plate; WP, Wollaston prism. Note the absence of any pulse compression except by bulk material. The polarization of the three waves interacting in the LGS crystal is indicated.

used for the reported MIR experiments while the remaining 200 μ J are driving a THz-based electron compressor [45, 39] for other purposes in electron microscopy [64]. The 187 μ J are split into three arms: A first part of 2 μ J (Fig. 5.3, red dotted line) is used to produce ultrashort probe pulses (yellow) for electro-optic sampling (EOS) of the MIR pulses.

The second part with 138 μ J (solid red line) goes into a noncollinear optical parametric amplifier system (NOPA, dotted outline) in which 2 μ J are used for white-light generation [165]; 136 μ J are used for second-harmonic generation (green line) with 30% efficiency. 40 μ J at 513 nm are used to pump the NOPA crystal. A YAG crystal with a thickness of 10 mm is used to generate a broad plateau-like white-light on the near-infrared side of the fundamental. Thinner YAG plates did not provide sufficient broadening towards the NIR. Alternatively we successfully tested an undoped Gadolinium Orthosilicate (GSO) crystal for the NIR continuum generation. It shows a very flat spectrum up to 1700 nm.

The NIR side of the YAG white-light allows direct amplification of the broadband 1200 nm pulses needed for the MIR generation. This approach is found to be superior compared to seeding the amplifier collinearly at 900 nm and using the resulting idler at 1200 nm for the subsequent mixing/amplification. We do not use a collinear geometry because it would require non-trivial dichroic mirrors or filters for the separation of pump, signal and idler after amplification that would likely lead to temporal phase-distortions of the output pulse. The small noncollinearity slightly reduces the amplification bandwidth to a value still broad enough for the present purpose [166]. The NOPA crystal is a 3-mm thick Type I β -BaB₂O₄ crystal (BBO) at a cut angle of 24.5° and a noncollinearity angle of 1-2°. The $1/e^2$ diameters of the seed beam and pump beam are both roughly 400 μm at the BBO. A longpass filter (High Performance longpass 1100 nm, Edmund Optics) blocks white-light wavelengths below 1120 nm in order to filter out the remaining fundamental light and to restrict the final MIR spectrum to below 12 μm where LGS would absorb. Figure 5.4(a) shows the pump laser spectrum (red) in comparison to the NOPA output spectrum (orange), ranging from 1120 nm to 1400 nm. The output pulse energy is 5 μJ . A concave spherical silver mirror ($f = 500$ mm) is used for beam collimation towards the next stage. The output of the NOPA subsystem are broadband, μJ -level pulses around 1200 nm to serve as seed light for the MIR generation.

In the subsequent amplification stage, 47 μJ pulses at 1026 nm are used to collinearly pump a LGS crystal. We use a type I orientation (xz cut) at a nominal cut angle of 47.9°. The various beam polarizations are shown in Fig. 5.3. A crystal thickness of 0.5 mm provides broadband phase matching and keeps the group velocity mismatch between pump and seed pulses sufficiently small (67 fs/mm). The phase matching is extremely broad already for a crystal orientation optimized for the central frequency and becomes even broader with a 0.5° additional tilt (see red and black solid lines in Fig. 5.4(b)). A 4 mm crystal [112] would render a much narrower spectrum (see black dotted line). The use of a 0.5 mm LGS crystal is possible due to the pre-amplification.

This time we employ a collinear geometry in order to avoid angular dispersion in the MIR output. The broadband NOPA beam (Fig. 5.4(a), orange) and the narrowband fundamental beam (Fig. 5.4(a), red) are combined with a dichroic mirror that reflects 1100 - 1320 nm and transmits around 1026 nm. Imperfections of this beam combiner slightly reduce the pump and seed energy before the LGS crystal from 47 μJ and 5 μJ to 37 μJ and 4 μJ . This loss is tolerable in view of the above-mentioned benefits of collinear amplification.

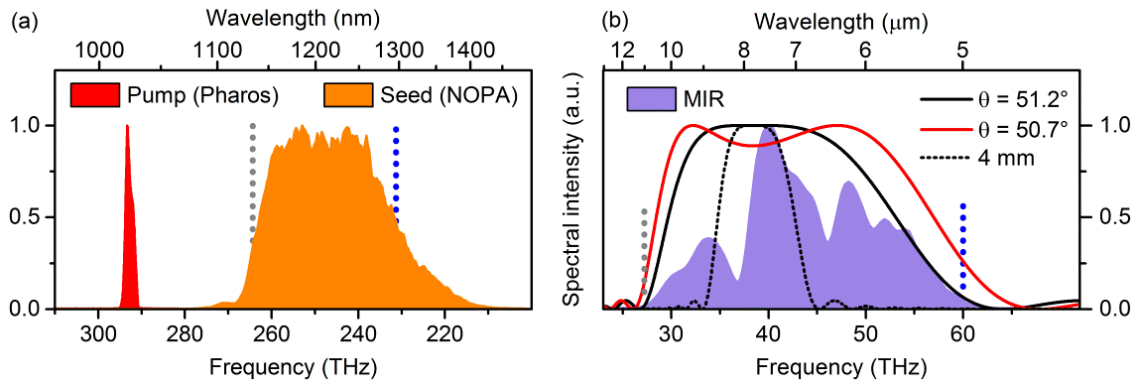


Figure 5.4: Spectra of the three key pulses involved. (a) Narrow spectrum of the laser pulses (red) and broadband spectrum of the NOPA output (orange). The grey and blue dotted line corresponds to frequencies that are needed to generate 11 and 5 μm by DFG. (b) MIR spectrum after OPA in LGS. Phase matching term $\text{sinc}^2(\Delta k \cdot d/2)$ for a 0.5 mm LGS crystal at perfect phase matching (black) and optimized for bandwidth (red). For comparison the sinc^2 curve for a 4 mm crystal is shown (black dotted).

The LGS crystal is placed considerably behind the focal planes to adjust the peak intensity to low enough values. This also helps to decrease the influence of the spherical aberration and compensates for small Kerr lensing effects. The $1/e^2$ beam diameters are 700 μm for the pump beam and 300 μm for the seed beam at the LGS crystal. The peak intensities are 70 GW/cm^2 and 65 GW/cm^2 , respectively. These rather moderate intensities avoid the onset of self-focusing, spectral broadening, cross-polarized wave generation, and thermal lensing effects or crystal damage. The precise values of the spot sized were optimized for MIR output power and bandwidth. For starting values, a desired gain of 3 was used in a plane wave approximation to estimate the needed intensity and thereby the spot size of the pump beam to start with.

After the LGS crystal, a long pass filter coated onto a 1-mm thick Germanium substrate (4.50 μm longpass OD > 3.0, Edmund Optics Inc.) filters out the remaining pump and seed beams. Neither of the pulses is intense enough to induce any nonlinear dynamics. We obtain the MIR spectrum shown in Fig. 5.4(b), measured with a Fourier-transform spectrometer (L-FTS, LASNIX). The spectrum spans the expected wavelength range of 5 - 11 μm with a rather smooth envelope and supports a Fourier limited pulse duration of 30.3 fs (FWHM). Note that the spectrum is shown on a linear scale, contrary to other reports where the spectral power density is shown on a logarithmic

mic scale [105, 79]. The direction of the energy scale in Fig. 5.4(a) is chosen opposite to the one in Fig. 5.4(b) to highlight that in the OPA process the higher-frequency seed photons are linked to the lower-frequency MIR photons. Matching positions are marked by the dotted grey and blue lines, showing the intended correspondence. The dips in the spectrum are attributed to interferences inside the spectrometer, residual reflectivity modulations in the optics and the absorption of air around 6.0 and 6.6 μm . Also the dip in the phase matching efficiency might contribute; see Fig. 5.4(b).

The MIR output power after the longpass Ge filter is 11 mW at a repetition rate of 50 kHz, corresponding to a pulse energy of 220 nJ. The quantum efficiency of the LGS stage, defined as the number of generated MIR photons divided by the number of input seed photons, is 31%. Other optimizations of the setup with a 1-mm thick LGS crystal provided more than two times higher output pulse energies at the cost of some spectral bandwidth.

5.3 Pulse compression and characterization

5.3.1 Dispersion estimation

A central challenge in broadband MIR generation is dispersion management and compression, because chirped mirrors at wavelengths $> 5 \mu\text{m}$ are still inefficient [89]. Alternatives like prism or grating sequences introduce additional higher order phase and are lossy and complicated to align in the MIR. Our setup therefore relies exclusively on bulk material for chirp management and pulse compression. In the collinear LGS amplifier it is necessary to match the two pulse durations to similar values in order to make best use of all the photons [167]. Fortunately, the near-infrared NOPA always produces (at sufficient amplification bandwidth) output pulses that are only slightly shorter than the pump pulse length, independently of the white-light chirp. Without any special effort, we therefore mix in the LGS crystal 170-fs long seed pulses (chirped) with 270-fs long pump pulses from the laser (near Fourier-limited).

In order to implement the envisioned all-bulk compression, we first consider theoretically all group delay contributions and their transfer during the nonlinear processes. The NIR NOPA output builds on the chirp of the white-light caused by the dispersion of YAG. More positive chirp is added by the longpass filter on a 3 mm fused silica

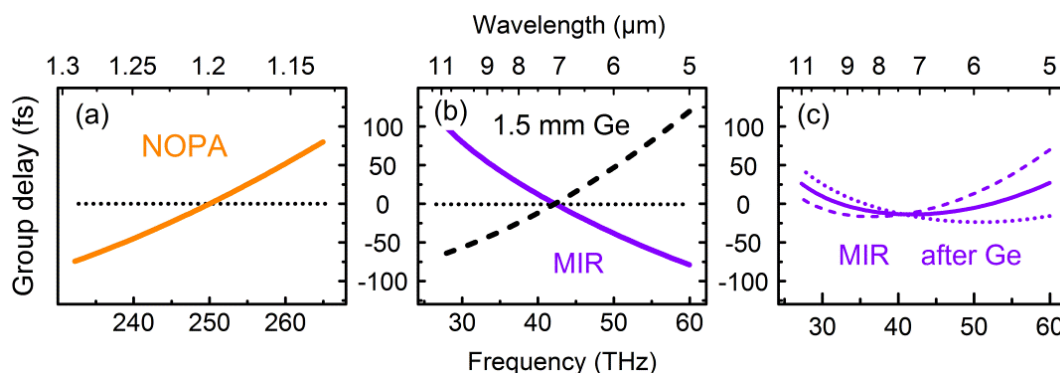


Figure 5.5: Calculated group delay curves of the pulses at the different stages. (a) NOPA seed at 90% of the LGS crystal. (b) MIR pulses directly after generation (purple), in comparison to the group delay of 1.5 mm of Ge (black, dashed). (c) MIR pulses after passing through 1.0 (dotted), 1.5 (solid) and 2.0 mm (dashed) of Ge.

substrate, the 3 mm BBO crystal and the focusing optics. The 1120-1400 nm output spectrum further acquires some positive chirp from roughly 90 % of the 0.5 mm LGS crystal. Considering most of the mixing crystal for the NIR dispersion reflects the fact that the main MIR output is generated at the very end of the crystal (see below). The MIR generation process converts this positive chirp into negatively chirped pulses in the MIR due to difference frequency mixing of the pump and the seed pulse. Some further negative chirp is obtained from roughly the last 10% of the LGS crystal which has negative group delay dispersion in the MIR. The major part of the MIR is indeed generated in the final part of the crystal as with any OPA out of saturation. A small thickness of normally dispersive material in transmission, e.g., Germanium, should therefore be suitable for pulse compression.

Figure 5.5 reports a calculation based on the dispersion curves of all materials, including the air, and shows the estimated group delay (GD) of the pulses at different stages. We see a rather flat group delay dispersion with only a minor degree of higher orders. The result suggests that simply a few mm of Ge material should be suitable for optimal pulse compression. Varying the amount of Ge through tilting of the plate allows to fine tune the compression.

The data in Fig. 5.5(a) reproduces well the measured 170-fs length of the NOPA output. The fact that the NIR seed pulse does not get chirped much in the propagation is due to the fact that the wavelength is quite close to the zero dispersion point of fused

silica and the other optical materials. Beyond the reported calculation we expect some additional GD contributions from the various dielectric filters.

5.3.2 Electro-optic sampling (EOS)

In order to characterize the MIR pulses in the temporal domain, we employ electro-optic sampling [99]. Short probe pulses are obtained from self-compression during continuum generation in a 1-mm YAG crystal. The effective focus inside the YAG is set to produce a single-filament only in the last few μm before the exit surface, in order to minimize dispersion and terminate the filament before group velocity dispersion effects become significant [165, 168].

A Schiefspiegler arrangement (tilted-component telescope) [168] is applied for all-reflective and nonastigmatic beam refocusing of these ultrashort continuum pulses. The $R = 150$ mm concave mirror is placed 127 mm from the YAG plate. The angle of incidence at this mirror is 3.4° . The subsequent convex mirror with $R = +200$ mm is placed at 103 mm distance and at an angle of incidence of 8.9° . The resulting focus is located about 0.5 m after the second mirror and can be fine-tuned by the mirror distances while slightly tweaking the second angle of incidence. A shortpass filter (XIS0780, Asahi Spectra USA Inc.) used in reflection cuts out the chirped high frequency parts of the continuum. Another shortpass filter (High Performance shortpass 950 nm, Edmund Optics, 1 mm substrate thickness) is used to block the residual fundamental light at 1026 nm. Figure 5.6 shows the spectrum and an intensity autocorrelation measurement [169], revealing a 12-fs duration which is sufficient for EOS of the MIR pulses.

The sampling element is a free-standing 20- μm thick GaSe crystal (Eksma) oriented for sum-frequency mixing between the MIR pulses and the white-light probe. A shortpass filter (High Performance shortpass 850 nm, Edmund Optics) removes the non-interacting spectral components in order to reduce the detection noise [170]. A quarter-wave plate and a Wollaston prism guide the two different polarizations onto two matched photodetectors of our own design [171], slightly modified to account for the higher repetition rate of 50 kHz. The shot-noise limit for detection is $2.6 \cdot 10^{-5}$ for a quantum efficiency of 80% of the detector, assuming 0.5 nJ gate pulse energy. The signals of the detectors are digitized continuously with a PicoScope 5000 Series oscilloscope (model 5444A, Pico Technology Ltd.) at 14 bit resolution and with a sampling interval of 100 ns. Typically scan durations are 1 s, amounting to $1 \cdot 10^7$ samples per trace.

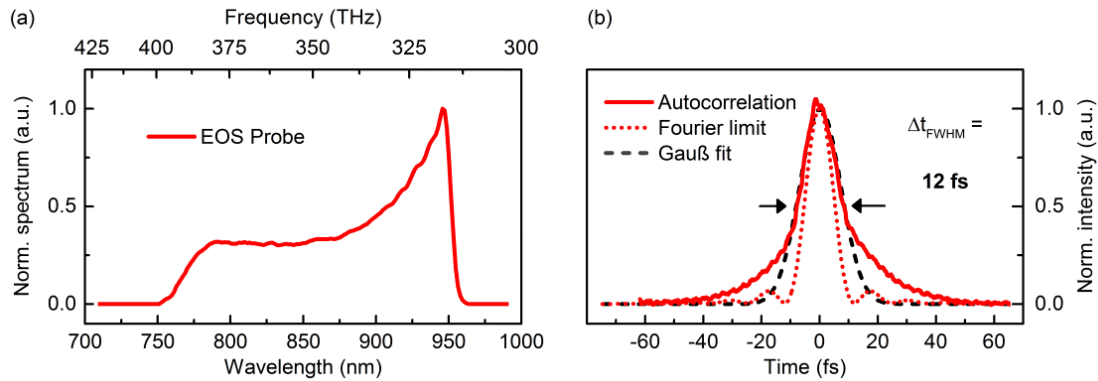


Figure 5.6: Short, weak probe pulses for EOS, obtained directly from white-light generation. (a) Spectrum measured after 2 shortpass filters. (b) Intensity autocorrelation measurement of the probe pulses (red); red dotted curve, Fourier-limited pulse shape of the spectrum shown in Fig. 4(a); black dashed curve, Gauß fit to the autocorrelation trace.

Figure 5.7(a) shows the EOS data for the case of 2 mm of bulk Ge for pulse compression. The blue curve shows the measured raw EOS signal. It is slightly limited on the short-wavelength side ($< 5 \mu\text{m}$) by the finite duration of the probe pulse (12 fs) and on the long-wavelength side ($> 10.5 \mu\text{m}$) by the EOS crystal thickness and its limited phase-matching bandwidth. By considering the measured probe pulse profile (see Fig. 5.6(b)) and the phase matching of GaSe, we obtain the spectral response function of our EOS measurement [86]. The final MIR field (Fig. 5.7(a) as the red curve) is then obtained by Fourier transformation, spectral correction and back-transformation. We see an ultrashort pulse of 32 fs duration (FWHM) at $\sim 7.5 \mu\text{m}$ center wavelength with 1.4 optical cycles in the main lobe. 93% of the energy is contained in the main pulse. The central peak has a 1.3 times stronger electric and magnetic field than the second-strongest field cycle at -23 fs. This ratio would increase to 1.9 in the case of zero carrier-envelope phase. Assuming a focus size with a diameter of two wavelengths, a peak electric field strength of 3 GV/m and a peak magnetic field of 10 T could be achieved.

Figures 5.7(b) and 5.7(c) show a more systematic study of the applied bulk compression concept. The measured group delay dispersion (GDD) and third order dispersion (TOD) of the MIR pulse are plotted as a function of the amount of Ge in the beam path. Linear fits (dashed) reveal $\sim 520 \text{ fs}^2/\text{mm}$ and $\sim 3130 \text{ fs}^3/\text{mm}$, respectively. Figure 5.7(d)

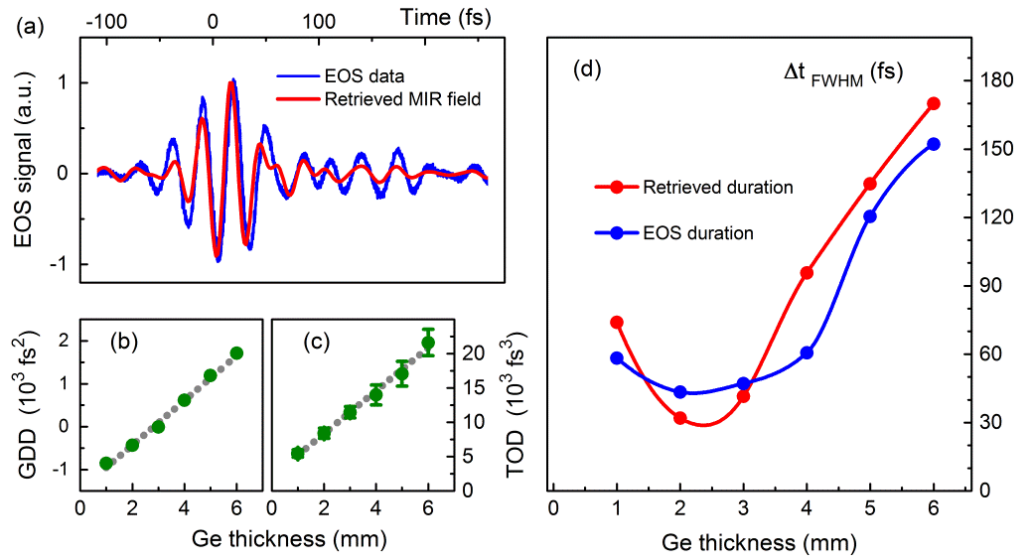


Figure 5.7: Electric field of the MIR pulses and systematic study of pulse compression. (a) EOS data (blue) and retrieved electric field (red). (b) GD dispersion added by Ge. (c) Third order dispersion added. (d) MIR pulse duration as a function of Ge thickness.

shows the measured pulse duration (FWHM) from EOS as a function of the Ge thickness. We see that the shortest pulses are achieved with about 2 mm of additional Ge.

A decisive advantage of our compression concept is that Fourier-limited MIR pulses can be obtained without any chirped mirrors or other special dispersive elements in the MIR. The measured pulse duration of 32 fs compares very well to the Fourier limit of 30.3 fs, showing that not only the linear chirp but also the higher orders are well compensated, as intended (see Fig. 5.5). In contrast to OR approaches, our inter-pulse MIR generation allows to apply available chirped mirrors for the NIR range (NOPA output) to control the MIR output even further. No direct MIR phase control is needed.

5.4 Beam quality

The spatial beam quality of the MIR output is crucial for many applications, especially in electron-pulse compression [39]. Figure 5.8(a) shows the MIR beam profile measured by a broadband pyroelectric array camera (Pyrocam IIIHR, Spiricon, Ophir Photonics). Figure 5.8(b) shows the vertical and horizontal beam caustics, revealing M^2 values of 1.8 and 1.7, respectively. The slight astigmatism comes probably from residual mis-

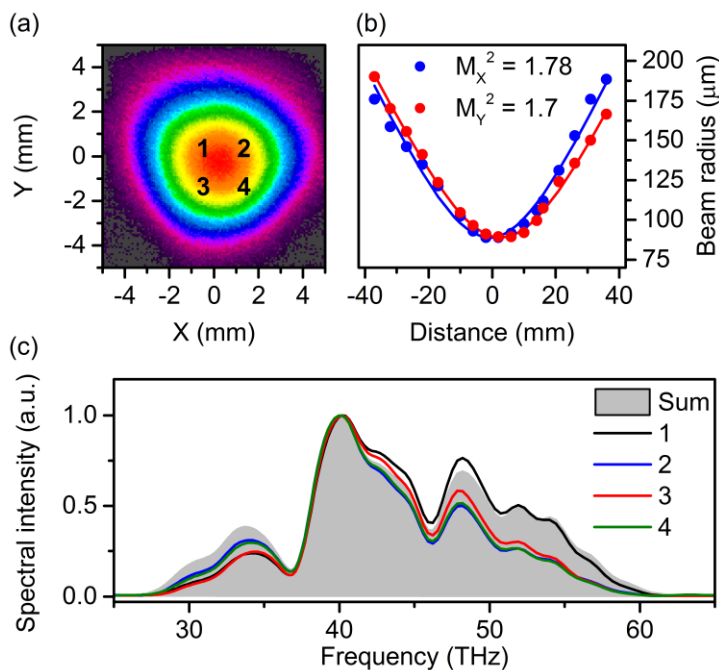


Figure 5.8: Beam quality measurement. (a) MIR beam profile. (b) Beam caustics in the vertical (red, y) and horizontal axis (blue, x). (c) Spectra measured at different position in the MIR beam as indicated in (a) in comparison to the total spectrum (grey).

alignments of the focusing parabola. For the broadband pulses it is decisive to know whether all spectral components propagate collinearly or the beam suffers from angular dispersion or pulse front tilt. No detrimental tilt is expected in our concept because the first noncollinear stage amplifies the seed beam and idler generation is collinear in the second stage. Figure 5.8(c) shows four spectra taken in the far field of the beam at the four positions indicated by 1-4 in Fig. 5.8(a). We see sufficient homogeneity and no indication of spatial chirp.

5.5 Power scalability and stability, CEP stability

In order to demonstrate that we indeed achieve genuine parametric amplification of the MIR pulses and not only see difference frequency radiation, we report in Fig. 5.9 several experiments on power dependencies. Figure 5.9(a) illustrates the quantities involved. Figure 5.9(b) shows the measured scaling of the MIR output energy when changing the

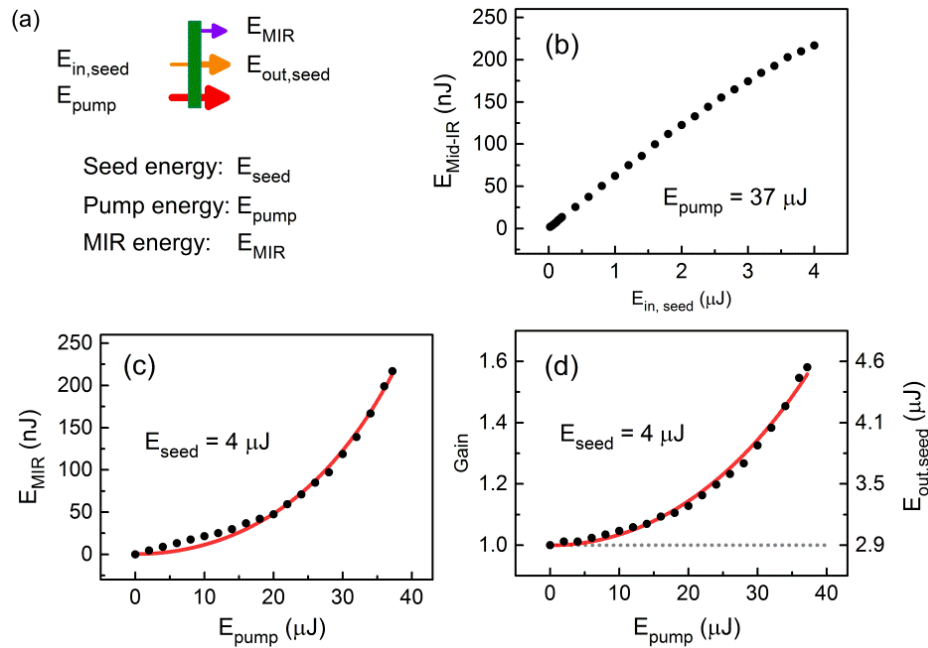


Figure 5.9: Energy dependence of the amplification in LGS. (a) The three interacting beams. (b) Output MIR energy at fixed pump energy as a function of seed energy. (c) Output MIR at fixed seed as a function of pump energy. Red line shows the \sinh^2 fit. (d) Gain measurement at fixed seed and increasing pump energy. Red line shows the \cosh^2 fit.

amount of applied 1120-1400 nm light. We see an almost linear scaling, with only a slight onset of saturation. More seed energy would only partially be beneficial for the present pump energy and beam geometries.

Figure 5.9(c) shows the output pulse energy as a function of the 1026 nm pump pulse energy. Here we observe approximately a \sinh^2 dependence as expected from the coupled wave equations for optical parametric amplification. Further scaling of the amplification efficiency seems possible by increasing the pump power. Our concept is therefore not limited to the reported values and can be scaled up if more fundamental laser light is available.

Figure 5.9(d) shows the gain factor of our 1120-1400 nm amplification. Plotted is the output seed energy (right axis) as a function of the pump pulse energy and the corresponding gain (left axis), defined as the output seed energy divided by the output seed energy with no pump. The measured values are substantially larger than one and therefore show that we are in the regime where MIR radiation is generated and

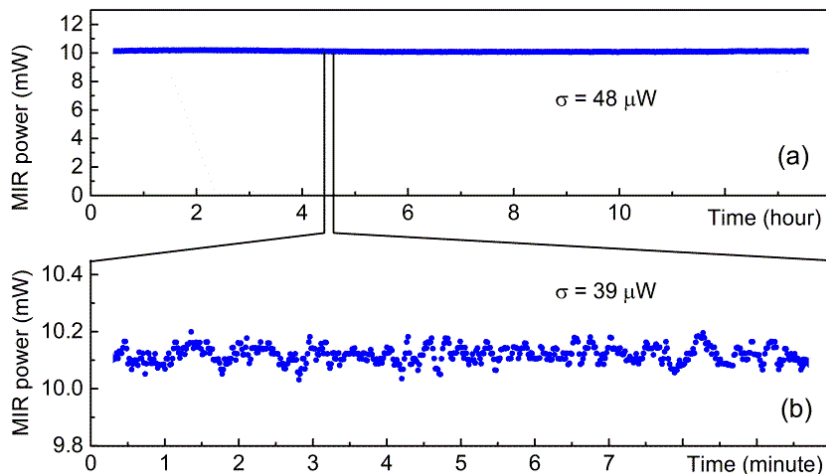


Figure 5.10: Long-term power stability. (a) Mid-infrared power averaged over every minute. (b) Raw measurement with one data point taken every second.

simultaneously amplified in the LGS crystal. This justifies the assumption made above, that switch from NIR NOPA output light to MIR wavelengths effectively happens close to the end of the LGS crystal. While varying the pump or the seed energy, we never observed any significant changes of the spectrum or bandwidth of the MIR output. This result means that we have no secondary or cascaded nonlinear optical processes besides the intended optical parametric amplification. Consequently, the MIR output is very stable.

Figure 5.10(a) shows a long-term scan of the MIR power, measured every second for more than 13 hours. The drifts (averaged over 60 s) amount to less than 0.47% rms. Figure 5.10(b) shows part of the data on shorter time scales (1 s averaging). The fluctuations amount to merely 0.39% rms. The pulse-to-pulse fluctuations are measured over 1000 shots with an amplified photodetector (MCT, Thorlabs) and amount to 0.63% rms. These values demonstrate the high stability of our approach on any time scale that could be relevant for applications.

The MIR output pulses have a stable carrier-envelope phase (CEP) because the seed pulses have the identical phase fluctuations $\Delta\phi$ as the fundamental laser pulses in both amplification stages. Consequently, the idler of the second stage becomes passively phase-locked and the MIR pulses have a stable CEP. Figure 5.11(a) shows a repeated measurement of EOS traces every 7 seconds over one hour. Figure 5.11(b) shows the extracted CEP values, averaged over one minute each. A faster time scale is reported

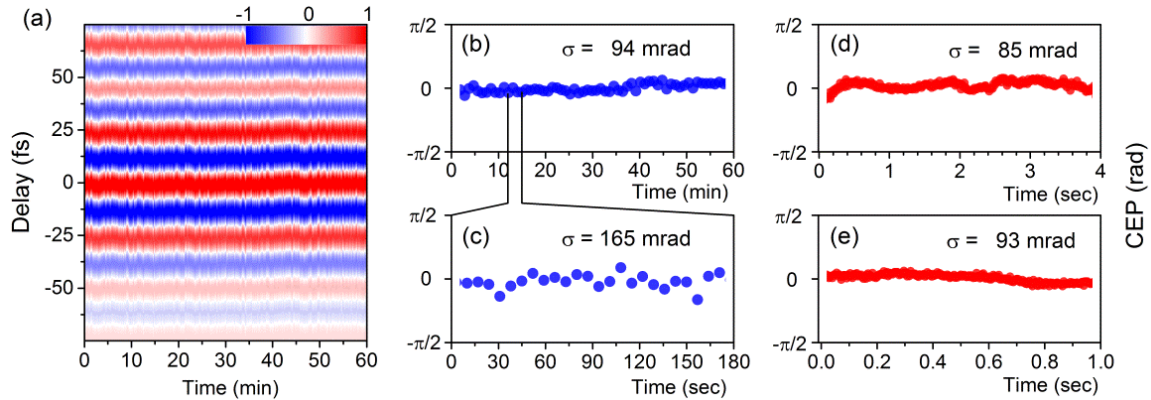


Figure 5.11: Stability of the carrier-envelope phase (CEP). (a) EOS traces measured repetitively over one hour, with data points taken every 7 seconds. (b) Evaluated carrier-envelope phase values. (c) Carrier-envelope phase measured as rapidly as possible in complete electro-optic sampling scans (every 7 seconds). (d) Single-shot CEP stability over 4 seconds (200.000 pulses, every 800th shown). (e) Single-shot CEP stability over 1 sec (50.000 pulses, every 200th shown).

in Fig. 5.11(c). For both time ranges, the CEP fluctuations are less than 0.053π or 165 mrad. For single shot resolution of the CEP fluctuations, the EOS delay is set to the zero crossing with the strongest temporal gradient and the signal is recorded for each laser shot. The slope of the signal change is calibrated and the measurement then directly renders the CEP fluctuation. The result is shown in Fig. 5.11(d) for a 4-second scan, with every 800th point displayed. The resulting rms value, taking into account all of the data, is 85 mrad. The results of a second scan over a window of 1 s are shown in Fig. 5.11(e), resulting in 93 mrad rms fluctuation.

The whole measurement is performed without any active delay stabilization, neither between the two arms of the difference frequency generation nor for the electro-optic sampling. This result demonstrates the passive phase cancellation in our MIR generation and furthermore shows the value of the reported simplifications by a careful design of noncollinear and collinear arrangements, chirp management with bulk materials and application of intensities well below the onset of higher-order nonlinearities. It should be noted that the reported values are strictly speaking upper limits because the additional possible fluctuation of the gate pulses (white-light) and its beam path length are also contributing to the measurement.

5.6 Discussion and future aspects

For our intended use of the MIR pulses in femtosecond electron scattering, there remain only few points of further desire. An optimized beam combiner for pump and seed pulses could support an even broader seed spectrum and consequently we could produce even shorter pulses in the MIR, approaching the sub-cycle regime. The phase matching of LGS supports this. Alternatively GaSe could be used to produce pulses at even longer wavelengths.

At present, the SHG efficiency in the NOPA is 30%, a value that should not be increased significantly in order to avoid temporal and spatial deteriorations of the pulses and beam. The NOPA is running with a 29% quantum efficiency (513 to 1200 nm), again very close to the maximum that avoids back conversion and pulse deterioration. Finally, the MIR mixing works at an amplification of 1.6. This corresponds to a 60% conversion of the 1200 nm seed photons in a DFG picture, close to full conversion. Referenced to the 1026-nm pump, the quantum efficiency is already 5%. A higher output up to 30% could only be achieved with harder pumping at the risk of crystal damage. Unless some added power instabilities, beam deteriorations or CEP fluctuations would be acceptable, we therefore think that the reported system is close to the optimum for most applications.

Higher MIR power could readily be achieved by using one of the available fs pump lasers with tens or even hundreds Watt power. Figures 5.9(b) and 5.9(c) show that both an increased pump intensity and also increased seed levels will lead to more output. An appropriate balance between the respective intensities will avoid the amplification of vacuum fluctuations [172] and issues with crystal damage.

Using a longer LGS crystal, for example 1 mm, is another alternative to increase the output power if the bandwidth of the MIR pulses is not a primary concern. In principle, the system is tunable, by changing the delay and noncollinearity angle in the NOPA and by adjusting the phase-matching conditions at the LGS. Tunable MIR pulses are valuable for spectroscopy, for controlling materials [173] or for light wave synthesis from multiple sources [98]. All of these suggestions can easily be implemented with the presented inter-pulse mixing scheme and its ample possibilities to adjust a certain parameter without changing other ones.

In summary, the reported results show how broadband single-cycle MIR pulses can be generated with simple OPA concepts and all-bulk compression. The 32 fs output pulse length is a shortening of nearly an order of magnitude from the pump pulse length. Two systems related to the reported one are already successfully running in two other

laboratories in collaborative efforts. Our own system will serve for attosecond electron microscopy and diffraction [46] of complex materials under strong-field, single-cycle excitation [143].

Acknowledgment

We thank Christina Hofer and Ioachim Pupeza for their loan of the 20- μm EOS crystal and acknowledge preliminary work together with Rupert Huber and Philipp Merkl.

Chapter 6

Second-harmonic generation and self-phase modulation of few-cycle mid-infrared pulses

So far, we have demonstrated mid-infrared generation via difference frequency generation and successfully generated 1.4 cycle pulses centered at $7.8 \mu\text{m}$ with pulse energy of hundreds of nJ. With such energy, field strength exceeding atomic Coulomb field ($> 1 \text{ GV/m}$) could already be reached, and many high-field phenomena (see also chapter 1 and section 2.1) could therefore be explored. To further boost the pulse energy, we have increased the thickness of the nonlinear crystal (LGS) from 0.5 mm to 1 mm, as suggested in section 5.6. An almost doubled pulse energy of 400 nJ has been obtained, with only a small part of the spectral bandwidth being compromised. The pulse duration merely increased by a negligible amount and the pulses stay in near single-cycle regime.

In this chapter, we implement the first application with the pulses mentioned above. Nonlinear processes such as second harmonic generation (SHG) and self-phase modulation (SPM) have been performed. As described at the beginning of this thesis, one of the essential properties of mid-infrared radiation is their ability to discern different molecules, especially in the molecular fingerprint region ($2 \mu\text{m}$ - $20 \mu\text{m}$). In order to obtain spectrum ranging from $3 \mu\text{m}$ to $5 \mu\text{m}$, spectral broadening in the fibers is usually employed. By pumping the fibers with $\sim 2 \mu\text{m}$ pulses, supercontinuum generation (SG) or Raman-induced soliton self-frequency shifting (SSFS) [63] can be induced, and the spectrum can extend to the desired wavelengths. However, such processes also introduce additional phase noise to the generated pulse. Hence, the CEP of such pulses becomes

less stable, which not only corrupt many CEP-sensitive excitation processes but also hinder the use of time-resolved spectroscopy.

By generating second harmonics from CEP-stable light source at $\sim 8 \mu\text{m}$ [67], broadband, CEP-stable spectrum from $3 \mu\text{m}$ to $5 \mu\text{m}$ can in principle be obtained. Furthermore, if the temporal delay and polarization of the generated second harmonics could be fine-tuned [192], a mid-infrared light field synthesizer can be constructed, and sub-cycle mid-infrared pulses can potentially be generated. By broadening the spectrum through SPM, it is also possible to compress the mid-infrared pulses further and enter sub-cycle regime. Such pulses would, without a doubt, offer a powerful tool for the attosecond science community. The following content (page 85-95) has been published in Optics Letters [68]¹

¹The original idea came from IP and PB. BC conducted all measurements under the supervision of PB. Both CH and BC ran the numerical simulation. All authors discuss and contribute to the writing of the manuscript.

Second-harmonic generation and self-phase modulation of few-cycle mid-infrared pulses

Bo-Han Chen, Christina Hofer, Ioachim Pupeza and Peter Baum

Abstract: Near-single-cycle mid-infrared pulses with a spectrum covering 5.4-11 μm are efficiently frequency-doubled in different GaSe crystals. The second-harmonic spectrum spans 3-4.3 μm at a power conversion efficiency of $>20\%$. We measure an effective nonlinear coefficient of $d_{eff} \approx 35 \text{ pm/V}$. We also report self-phase modulation and spectral broadening of the mid-infrared pulses in various bulk materials and find an increase of 45 % of spectral width for 5 mm of Ge. These results demonstrate that nonlinear optical conversions can efficiently be driven by few-cycle mid-infrared radiation.

<https://doi.org/10.1364/OL.44.004079>

© 2019 Optical Society of America

The outstanding coherence of laser radiation affords an exceptional control over the electric field of light at the level of the optical cycles. Of particular interest are waveform-controlled, few-cycle pulses with field strengths on the order of the atomic Coulomb field, $\sim 0.1 \text{ V/\AA}$. Such pulses enable the study of quasiparticles and nonperturbative nonlinear optics in crystals [150, 174, 175] or gases [176–178], the all-optical control of electron beams [39, 45, 179, 180] or field-resolved spectroscopy of molecular vibrations [79, 181, 182]. However, mid-infrared laser sources often do not operate at appropriate central wavelengths or enough coherent spectral width for such experiments. In particular, realizing waveform-controlled single-cycle pulses with a simultaneous spectral coverage below and above $\sim 5 \mu\text{m}$, the transparency threshold of oxide crystals [148], remains a challenge.

In this Letter, we report efficient second-harmonic generation (SHG) and self-phase modulation (SPM) of few-cycle pulses in the long-wave mid-infrared region of the optical spectrum around 5-11 μm . These results advance earlier findings made with picosecond

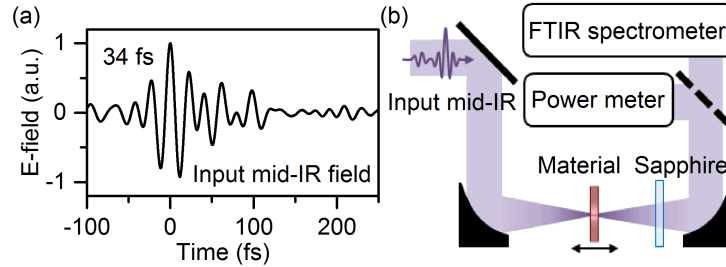


Figure 6.1: Fundamental mid-infrared pulses and experimental setup. (a) Electric field measured with electro-optic sampling and retrieved from deconvolution with the detection’s response function. (b) Experimental setup. FTIR, Fourier-transform infrared spectrometer; dashed line, flip mirror.

pulses from free-electron lasers [183] or CO₂ lasers [184, 185] into the regime of broadband waveform-controlled pulses from femtosecond lasers and demonstrate the feasibility of few-cycle nonlinear optical conversions with mid-infrared radiation. The SPM results expand earlier findings with supercontinuum generation [91, 186] to the regime of simple and direct spectral broadening without filament formation and cascaded nonlinear optics.

The mid-infrared pulses used for our experiments are obtained from a non-collinear optical parametric amplifier comprising white-light seed generation and broadband parametric amplification of the near-IR part around 1200 nm followed by type-I difference frequency mixing with the 1030 nm pulses from the driving laser (Pharos PH1-20, Light Conversion) [67]. The output MIR pulses have a pulse energy of 400 nJ at a repetition rate of 50 kHz and a central wavelength of 7 μm . The spectrum covers 5.4-11 μm (27.3-55.5 THz) at -20 dB intensity and the ultrashort electric-field has a pulse duration of 34 fs or 1.4 optical cycles (intensity full width at half maximum, FWHM). Figure 6.1(a) shows an electro-optic sampling measurement, made with a 20- μm thick GaSe crystal and 12-fs visible probe pulses from a supercontinuum source [67], of the electric field as it enters our optical setup.

Figure 6.1(b) depicts the experiment. The few-cycle mid-infrared pulses are focused and re-collimated by off-axis parabolic mirrors ($f = 50.8$ mm, MPD129-M01, Thorlabs) and then sent to diagnostics. In the focus, we measure a beam diameter of 84 μm ($1/e^2$ of the intensity), measured with a Si microbolometer array (WinCamD-FIR2-16-HR, Dataray). The pulses have therefore a peak intensity of ~ 400 GW/cm² and a peak field strength of ~ 1.7 GV/m or 0.17 V/Å. Output spectra after the nonlinear optical interaction are measured with a Fourier-transform infrared spectrometer (L-

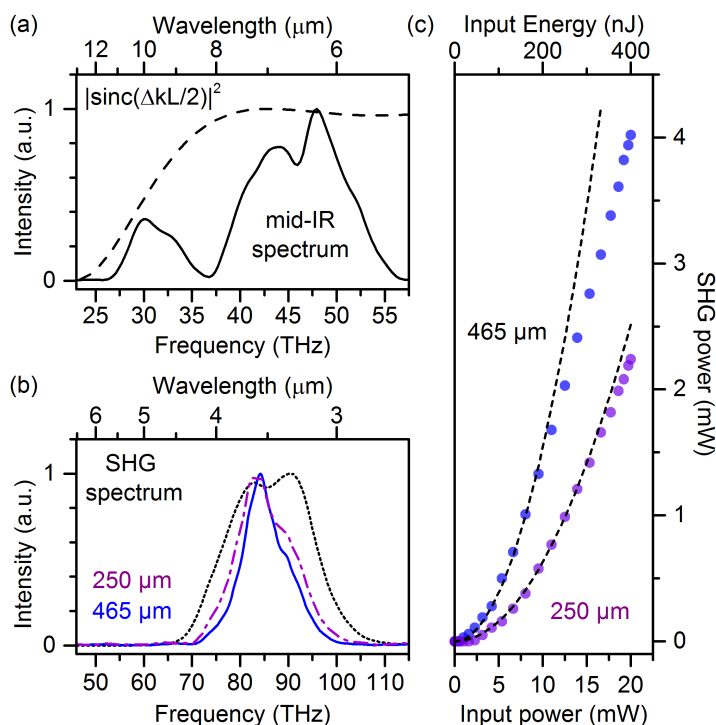


Figure 6.2: Second harmonic generation. (a) Fundamental mid-infrared spectrum (solid) and phase-matching function $|\text{sinc}(\Delta k/2)|^2$ (dashed) of the 250- μm GaSe crystal. (b) Second-harmonic spectrum generated from 250 μm of GaSe (violet, dot-dashed) and 465 μm GaSe (blue, solid). Black-dotted line: simulated second harmonic spectrum according to (a) for the 250- μm crystal. (c) Power dependence measurement. Scattered dots, measured data; dashed lines, quadratic fits.

FTS, LASNIX) and the power is detected with a thermopile absorption sensor (PS19, Coherent). A sapphire filter is used in some of our experiments to filter out unwanted spectral components.

In a first experiment, we report on second harmonic generation. We choose GaSe as the nonlinear crystal because of its rather high optical nonlinearity of ~ 50 pm/V [187] and its broadband transparency range (0.7 μm –18 μm) [188, 189]. We investigate two different crystal thicknesses, 250 μm and 465 μm , measured by optical interferometry and femtosecond group delay measurements. The crystal main axis is tilted by 33° with respect to the optical axis in order to satisfy type-I phase matching at an internal angle of 11° after refraction. In this geometry, the temporal walk-off is 10 fs for the 250- μm GaSe and 20 fs for the 465- μm GaSe, and the spatial walk-off is 54 mrad. The crystal is

moved along the beam propagation direction in order to maximize the second harmonic output power. A 1-mm sapphire plate filters away the remaining input mid-infrared radiation. The second-harmonic pulses are then sent to diagnostics.

Figure 6.2 depicts the results. The input spectrum to be frequency-doubled is shown in Fig. 6.2(a), covering the spectral range between 5.4-11 μm at -20 dB intensity. The dashed line shows the calculated phase-matching function $|\text{sinc}(\Delta k/2)|^2$ for 250 μm of GaSe at the experimental tilt angle. Figure 6.2(b), dotted curve, shows the corresponding second-harmonic spectrum that could be expected from a thin (250- μm) GaSe crystal. However, the electro-optic sampling data of Fig. 6.1(a) reveals some residual second-order dispersion of -100 fs^2 and a substantial third-order dispersion of 15700 fs^3 of the input pulses and therefore a non-Gaussian shape in time. In the frequency domain, components at the wings of the input spectrum are less well compressed than the central part. Pulses with third-order dispersion have therefore a narrower second-harmonic spectrum than expected from the phase-matching limit [164].

The blue solid line shows the measured SHG spectrum for the 465- μm GaSe crystal and the violet dash-dotted line shows the measured spectrum for the 250- μm crystal. Both spectra are indeed somewhat narrower than the expectation for non-chirped input pulses, but the spectral bandwidth at -20 db is still 3-4.3 μm for the 465 μm crystal and 2.8-4.4 μm for the 250 μm crystal. A further improvement is expected from controlling the higher-order dispersion, for example with state-of-the-art infrared multilayer optics [190].

Figure 6.2(c) shows the output power as a function of input power (pulse energy). Both for the 465- μm GaSe crystal (blue dots) and the 250- μm crystal (violet dots) we see a characteristic quadratic increase with pump power. Due to walk-off effects, back-conversion, third-order nonlinearities or multi-photon absorption by impurities or dislocations, saturation effects become observable above 15 mW of pump power for the 465- μm crystal and above 20 mW for the 250- μm crystal. A maximum output power of 4 mW was achieved with the 465- μm crystal after the sapphire filter. This value corresponds to a pulse energy of 80 nJ, a power conversion efficiency of 20 % and a quantum efficiency of 10 %, from before the GaSe to after all filters of the experiment.

In order to determine the absolute conversion efficiency inside the GaSe crystal, we consider the Fresnel losses of the input mid-infrared pulses at the crystal's front surface (reflectivity 21 % at 7 μm wavelength) and the losses of the second-harmonic pulses at the back surface (reflectivity 17 % at 3.5 μm wavelength). The sapphire filter has a total total transmission of 87 % at 3.5 μm wavelength. In principle, all these losses can

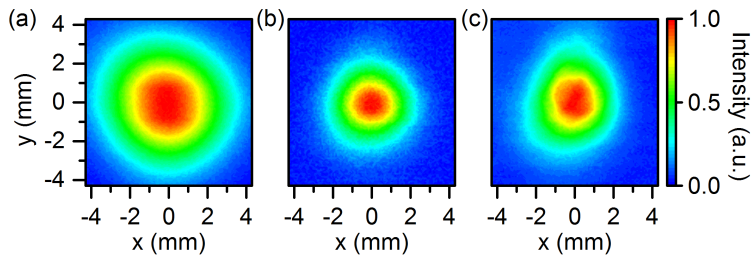


Figure 6.3: Far-field beam profiles. (a) Input mid-infrared beam. (b) Second harmonic beam from $250\ \mu\text{m}$ of GaSe. (c) Second harmonic beam from $465\ \mu\text{m}$ of GaSe.

be avoided by using proper anti-reflection coatings but those were not at our disposal at the time of experiment. If avoiding the interface losses, the second harmonic power with the $465\text{-}\mu\text{m}$ crystal would be $5.5\ \text{mW}$, the power conversion efficiency would be $35\ \%$ and the quantum efficiency would be $18\ \%$. These values allow us to estimate the effective nonlinear coefficient d_{eff} in our experiment. Taking into account the beam size at the focus, the phase-matching condition and the crystal length, we obtain $35\ \text{pm/V}$, with an estimated error of $\pm 20\ \%$. This result is a lower limit due to the potential contributions of temporal and spatial walk-off. The measured d_{eff} compares to previous results obtained with nanosecond [191] and sub-nanosecond [187] lasers and shows that GaSe maintains its beneficial nonlinearity when entering the few-cycle regime of pulses with close to octave-broad spectra.

Figure 6.3(a) shows the far-field beam profile of the incoming mid-infrared pulses, measured with a pyroelectric array camera (Pyrocam IIIHR, Spiricon, Ophir Photonics). Figure 6.3(b) and 6.3(c) show the beam profiles of the second harmonic pulses from the $250\text{-}\mu\text{m}$ and $465\text{-}\mu\text{m}$ GaSe crystals after the sapphire filter and beam collimation. We see that the second harmonic beam sizes are smaller than the input beam size by a factor of about $\sqrt{2}$, as expected. The slight asymmetry in Fig. 6.3(c) is probably caused by spatial walk-off ($54\ \text{mrad}$) or the onset of cascaded processes in the thicker crystal.

The fundamental mid-infrared pulses driving our experiments have a passively stable carrier-envelope phase (CEP) [67] and the second-harmonic pulses should therefore also be CEP-stable. The fundamental and second-harmonic pulses are therefore suitable for coherent short-pulse synthesis [192, 90]. Figure 6.4 shows the calculated Fourier-limited pulse shape and electric field when assuming a combination of the measured fundamental spectrum with the measured SHG output ($465\text{-}\mu\text{m}$ crystal) at the measured power ratio of roughly 5:1. We suppose equal polarization and CEP to produce cosine-like pulses.

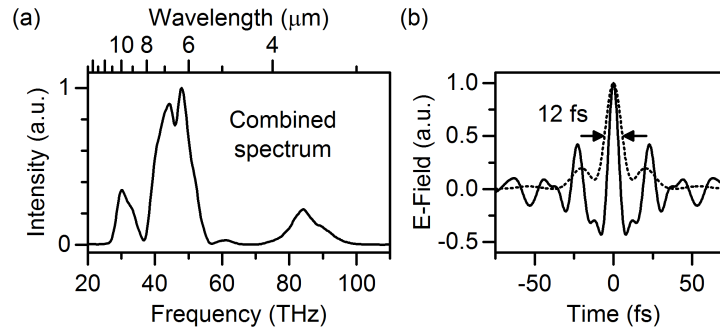


Figure 6.4: Hypothetical waveform synthesizer. (a) Combined spectrum of the fundamental mid-infrared and second harmonic pulses. (b) Fourier-limited pulse shape (dotted) and electric field for a cosine-like pulse (solid).

The relative delay is assumed to be zero [192, 90]. The result, plotted in Fig. 6.4(b) is an electric field with merely 0.7 optical cycles within a FWHM pulse duration of 12 fs. With a hypothetical 2λ focus diameter, the peak electric field could reach >10 GV/m or 1 V/Å. The central peak's electric field is >2.3 times stronger than any neighboring optical cycles. Such an ultrashort synthesized light field, obtainable with one single and simple SHG stage, could probably be useful for high-field physics or ultrabroadband spectroscopy.

In a second experiment, we report self-phase modulation and spectral broadening of our mid-infrared few-cycle pulses in different bulk materials [91, 186]. In contrast to fibers [103], bulk materials are better scalable to higher pulse energies and average powers. The setup is similar as above but now without the sapphire filter. The parabolic mirrors have a slightly longer focal length ($f = 101.6$ mm, MPD149-M01, Thorlabs), producing a focus with a diameter of 175 μm ($1/e^2$ intensity) and a peak intensity of 92 GW/cm^2 . The investigated bulk materials are 5 mm of KCl, 5 mm of CaF₂, 2 mm of KBr, 5 mm of ZnSe and 5 mm of Ge, each placed into the beam under normal incidence.

Figure 6.5 depicts the results. For KCl, CaF₂ and KBr we find no substantial effects at the given peak intensity. Figure 6.5(a) shows the results for ZnSe when moving the crystal through the focus position. Figure 6.5(b) shows the results for Ge. The change of the Fourier-limited pulse duration is plotted for the two crystals in Figs. 6.5(c) and 6.5(d). From the spectra in Fig. 6.5(a) and 6.5(b) we see in both cases first an increase and afterwards a decrease of the broadening when moving the crystal through the focus. Interestingly, the spectral shapes are not symmetric with respect to the focus position

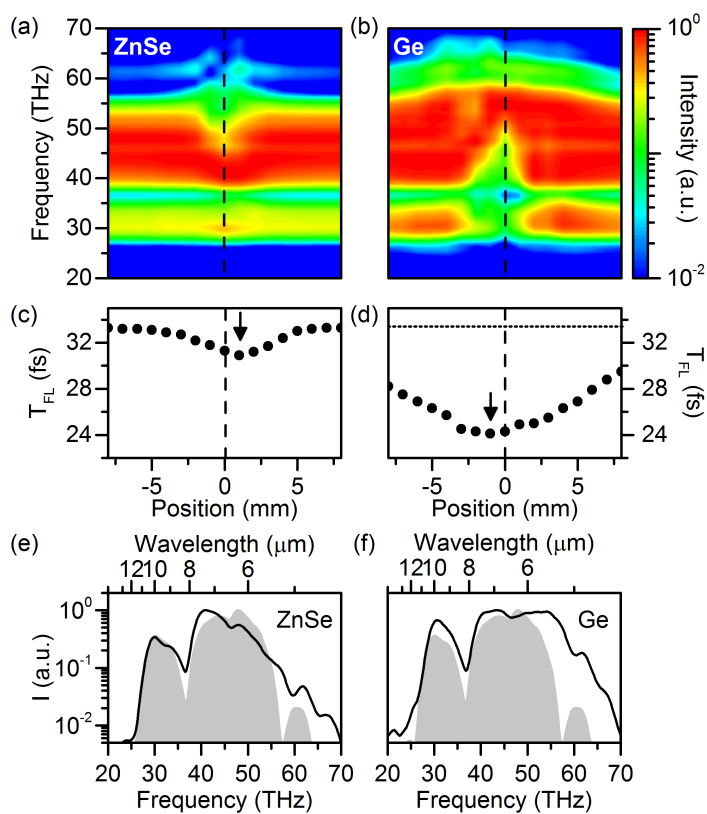


Figure 6.5: Self-phase modulation and spectral broadening. (a) Output spectrum as a function of crystal position for ZnSe. (b) Output spectrum for Ge. (c) Fourier-limited pulse duration TFL for ZnSe as a function of crystal position. (d) Fourier-limited pulse duration TFL for Ge. The arrows mark the best broadening for shortest pulses. (e) Broadest spectrum achieved with ZnSe. (f) Broadest spectrum achieved with Ge. Grey area shows the original mid-infrared spectrum for comparison. I , normalized spectral intensity.

and the most broadband spectrum is seen slightly after the focus for ZnSe and slightly before the focus for Ge. Both crystals are thick enough that spectral broadening, chirp and intensity changes occur simultaneously and affect each other [66]. The fact that the broadest spectrum is observed slightly after the focus for ZnSe and slightly before the focus for Ge is probably related to the different signs of first-order dispersion in these two materials (ZnSe, about -406 fs^2 ; Ge, about $+567 \text{ fs}^2$) [193, 194].

For ZnSe, the best-broadened mid-infrared spectrum, plotted in Fig. 6.5(e), supports a Fourier-limited pulse duration of 30.7 fs. For Ge, the best broadened spectrum is plotted in Fig. 6.5(f) and shows a Fourier limit of 24.8 fs. This value corresponds to a shortening of 27 %. The spectral width at -20 dB intensity increases by 45 % and now covers 27-68 THz in a coherent way. Self-phase modulation causes mostly a smooth, quadratic spectral phase and compression to these Fourier limits should therefore be realistic with bulk materials, for example GaAs [186], or with chirped MIR mirrors [89].

A somewhat detrimental effect of Ge is a substantial drop of the mid-infrared transmission to 11 % at maximum broadening. This loss is probably associated with multiphoton absorption owing to Ge's low bandgap of 0.66 eV [195]. However, no long-term damage was observed and the spectrally broadened output pulses still have 44 nJ of pulse energy and an average power of 2.2 mW, making them useful for spectroscopy or further nonlinear conversions.

In summary, the reported two results on second-harmonic generation and self-phase modulation show that nonlinear optics with driving pulses in the long-wave mid-infrared region of the spectrum is feasible, easy and efficient. The SHG spectrum obtained at the reported conditions covers an interesting spectral region for applications in molecular spectroscopy. In particular, the spectral coverage of high-sensitivity, high-power, field-resolved spectroscopy of biofluids [181] could be extended from the spectral regions of nucleic acids and carbohydrates to those of proteins and lipids [196]. The ability to cover novel spectral ranges in new ways with modern mid-infrared lasers will potentially also open up advanced possibilities in electron-beam control [39, 45, 179, 180], sub-cycle electron microscopy [64] or high-field attosecond science [143, 150, 174–176, 197].

Conclusions and future aspects

In summary, this work has demonstrated the generation of high power, phase-stable, near single-cycle mid-infrared pulses and their application. The mid-infrared pulse energy of 400 nJ, a central wavelength at around $7.5 \mu\text{m}$ and a pulse duration of 34 fs, containing 1.4 light field cycles has been achieved. These pulses indeed do not possess record-breaking power (cf. 2.7(a)). However, this work provides moderate pulse energy while still keeping the pulse duration near Fourier-limit (cf. Fig. 2.7(b)). With proper beam focus, these pulses are capable of offering a peak electric field higher than 10^9 V/m at the mid-infrared range, making them a great source for spectroscopy, excitation of specific molecular and electronic dynamics, particle acceleration, ultrafast electron diffraction and microscopy.

The reported mid-infrared pulses are realized based on two critical factors — first, the choice of generation scheme and second, the dispersion management of the seed pulses. The shift from using a single, bulk-fiber-broadened 30-fs pulse (chapter 3) for intra-pulse difference-frequency generation (IPDFG, chapter 4) to inter-pulse difference-frequency generation (DFG, chapter 5) not only reduces the complexity and size of the experimental setup but also increase the mid-infrared pulse energy by more than an order of magnitude. Notice that in Fig. 2.7(a), the pulse energy of our work surpasses most of the results generated through IPDFG (triangular points), as summarized in table 2.2. The dispersion control of the seed pulse in the non-collinear optical parametric amplifier (NOPA) system plays a critical role in the mid-infrared pulse shortening. By carefully manipulating the phase of the seed pulses, we bypass the need for grating compressors or chirped mirrors for the mid-infrared pulses (section 2.3.2) and enable

direct pulse compression by dispersive bulk materials. The mid-infrared pulse shape or even field transient can be precisely controlled by deliberately designing the phase of the seed pulse with chirped mirrors for near-infrared range or spatial-light modulator (SLM).

Being equipped with such novel pulses, we should ask ourselves — what are the next steps and where can they lead us to. First of all, to improve the overall performance of our work, an optical parametric chirped-pulse amplification (OPCPA) can be employed after the NOPA system. The pulse energy can, in principle, be boosted to μJ energy level. Also, replacing the beam combiner with a broader-bandwidth one which covers the whole seed spectrum can increase the bandwidth of the generated mid-infrared pulses and potentially lead to sub-cycle mid-infrared pulses. Furthermore, a simple model can be established for calculating the corresponding phase of the seed pulse for a particular mid-infrared pulse shape. Combining with an SLM, such programmable mid-infrared pulse shaping could become useful for the mid-infrared pump - mid-infrared probe experiments.

Several exciting experiments can also be carried out with the mid-infrared pulses generated in this work. First, as a follow-up experiment for chapter 6, nonlinear optical processes such as second-harmonic generation or self-phase modulation can, for the first, be observed in the time domain. The study of electric field change during nonlinear optical processes can provide us better understandings and more educational insights into the fundamentals of nonlinear optics. Secondly, because of the ponderomotive energy scaling, it would be interesting to apply these mid-infrared pulses for high-harmonic generation (HHG) [29, 30, 177]. A continuous and broadband spectrum supporting isolated attosecond pulses can be expected.

Lastly, mid-infrared pulses are ideal for electron generation and manipulation. Field emission driven by our 1.4-cycle, $7.5\ \mu\text{m}$ pulses from a metallic nano-tip can be inspected, and highly coherent point electron emission source can be explored [198–200]. Tabletop particle accelerators [37] can also be accomplished and will become more accessible. Moreover, combining with a 1st stage terahertz-based electron pulse compression setup [45], a double-stage, all-optical electron pulse compression setup can be realized, offering a promising way to isolated sub-femtosecond electron pulse generation. With the help of such short electron pulses, ultrafast electron diffraction (UED) and microscopy can be taken to the next level, achieving unprecedented attosecond-angstrom resolution, and allowing us to gain more thorough knowledge about light-matter interaction and the fundamentals of natural materials.

Data archiving

The experimental raw data, evaluation files, and original figures can be found on the Data Archive Server of the Laboratory for Attosecond Physics at the Max Planck Institute of Quantum Optics:

```
/afs/ipp-garching.mpg.de/mpq/lap/publication_archive
```

The main folder **Chen, Bo-Han** (PhD) contains two sub-folders **Data** and **Figure**, which contains all the raw data and figures, one **Redme.txt** file which explains the data information, and a PDF file of this thesis.

The source data of all figures is organized in the **Data** sub-folder, where all of the data is arranged in their corresponding **chapterx** sub-folder. In each sub-folder, a **Readme.txt** file can be found which contains the detailed description of the raw data, and how the figures were obtained.

Bibliography

- [1] I. Newton. *Opticks*. Dover Press, 1704.
- [2] W. Herschel. Experiments on the Refrangibility of the Invisible Rays of the Sun. *Philosophical Transactions of the Royal Society of London*, 90:284–292, 1800.
- [3] G. R. Hunt and J. W. Salisbury. Lunar Surface Features - Mid-infrared Spectral Observations. *Science*, 146(364):641–&, 1964.
- [4] J. R. P. Angel, A. Y. S. Cheng, and N. J. Woolf. A space telescope for infrared spectroscopy of Earth-like planets. *Nature*, 322(6077):341–343, July 1986.
- [5] D. C. Fernandez, R. Bhargava, S. M. Hewitt, and I. W. Levin. Infrared spectroscopic imaging for histopathologic recognition. *Nature Biotechnology*, 23(4):469–474, April 2005.
- [6] S. Junaid, S. Chaitanya Kumar, M. Mathez, M. Hermes, N. Stone, N. Shepherd, M. Ebrahim-Zadeh, P. Tidemand-Lichtenberg, and C. Pedersen. Video-rate, mid-infrared hyperspectral upconversion imaging. *Optica*, 6(6):702–708, June 2019.
- [7] N. M. Israelsen, C. R. Petersen, A. Barh, D. Jain, M. Jensen, G. Hanneschlager, P. Tidemand-Lichtenberg, C. Pedersen, A. Podoleanu, and O. Bang. Real-time high-resolution mid-infrared optical coherence tomography. *Light-science & Applications*, 8:11, January 2019.
- [8] F. Adler, M. J. Thorpe, K. C. Cossel, and J. Ye. Cavity-Enhanced Direct Frequency Comb Spectroscopy: Technology and Applications. *Annual Review of Analytical Chemistry*, 3(1):175–205, 2010.

-
- [9] A. Schliesser, N. Picqué, and T. W. Hänsch. Mid-infrared frequency combs. *Nature Photonics*, 6:440, June 2012.
- [10] J. Haas and B. Mizaikoff. Advances in Mid-Infrared Spectroscopy for Chemical Analysis. *Annual Review of Analytical Chemistry*, 9(1):45–68, 2016.
- [11] O. Kara, L. Maidment, T. Gardiner, P. G. Schunemann, and D. T. Reid. Dual-comb spectroscopy in the spectral fingerprint region using OPGaP optical parametric oscillators. *Optics Express*, 25(26):32713–32721, December 2017.
- [12] H. Timmers, A. Kowligy, A. Lind, F. C. Cruz, N. Nader, M. Silfies, G. Ycas, T. K. Allison, P. G. Schunemann, S. B. Papp, and S. A. Diddams. Molecular fingerprinting with bright, broadband infrared frequency combs. *Optica*, 5(6):727–732, June 2018.
- [13] K. Michel, T. Terhoeven-Urselmans, R. Nitschke, P. Steffan, and B. Ludwig. Use of near- and mid-infrared spectroscopy to distinguish carbon and nitrogen originating from char and forest-floor material in soils. *Journal of Plant Nutrition and Soil Science*, 172(1):63–70, 2009.
- [14] M. E. Fajardo, C. H. Neel, and D. G. Lacina. Using mid-infrared external reflectance spectroscopy to distinguish between different commercially produced Poly[Methyl MethAcrylate] (PMMA) samples - a null result, 2018.
- [15] A. B. Seddon. Mid-infrared photonics for early cancer diagnosis. In *2014 16th International Conference on Transparent Optical Networks (ICTON)*, pages 1–4, 2014.
- [16] M. Kyriakidou, J. Anastassopoulou, A. Tsakiris, M. Kouli, and T. Theophanides. FT-IR Spectroscopy Study in Early Diagnosis of Skin Cancer. *In vivo (Athens, Greece)*, 31(29102935):1131–1137, November 2017.
- [17] T. H. Maiman. Stimulated optical radiation in Ruby. *Nature*, 187(4736):493–494, August 1960.
- [18] O. R. Wood and S. E. Schwarz. Passive mode locking of a CO₂ laser. *Applied Physics Letters*, 12(8):263–&, 1968.

- [19] E. P. Ippen, C. V. Shank, and A. Dienes. Passive mode locking of the cw dye laser. *Applied Physics Letters*, 21(8):348–350, 1972.
- [20] H. Fattahi, H. G. Barros, M. Gorjan, T. Nubbemeyer, B. Alsaif, C. Y. Teisset, M. Schultze, S. Prinz, M. Haefner, M. Ueffing, A. Alismail, L. Vámos, A. Schwarz, O. Pronin, J. Brons, X. T. Geng, G. Arisholm, M. Ciappina, V. S. Yakovlev, D. Kim, A. M. Azzeer, N. Karpowicz, D. Sutter, Z. Major, T. Metzger, and F. Krausz. Third-generation femtosecond technology. *Optica*, 1(1):45–63, July 2014.
- [21] G. Günter, A. A. Anappara, J. Hees, A. Sell, G. Biasiol, L. Sorba, S. De Liberato, C. Ciuti, A. Tredicucci, A. Leitenstorfer, and R. Huber. Sub-cycle switch-on of ultrastrong light-matter interaction. *Nature*, 458:178, March 2009.
- [22] L. B. Madsen and M. Plummer. In intense laser fields: mechanisms for enhanced ionization in the multiphoton regime. *Journal of Physics B: Atomic, Molecular and Optical Physics*, 31(1):87–104, January 1998.
- [23] Vladimir S. Popov. Tunnel and multiphoton ionization of atoms and ions in a strong laser field (Keldysh theory). *Physics-Uspokhi*, 47(9):855–885, September 2004.
- [24] J. Dura, N. Camus, A. Thai, A. Britz, M. Hemmer, M. Baudisch, A. Senftleben, C. D. Schröter, J. Ullrich, R. Moshhammer, and J. Biegert. Ionization with low-frequency fields in the tunneling regime. *Scientific Reports*, 3:2675, September 2013.
- [25] B. Wolter, M. G. Pullen, M. Baudisch, M. Sciafani, M. Hemmer, A. Senftleben, C. D. Schröter, J. Ullrich, R. Moshhammer, and J. Biegert. Strong-field physics with Mid-IR fields. *Physical Review X*, 5(2):021034, June 2015.
- [26] L. V. Keldysh. Ionization in the field of a strong electromagnetic wave. *Soviet Physics - JETP*, 20(5):1307–1314, 1965.
- [27] J. L. Krause, K. J. Schafer, and K. C. Kulander. High-order harmonic generation from atoms and ions in the high intensity regime. *Physical Review Letters*, 68(24):3535–3538, June 1992.

-
- [28] P. B. Corkum. Plasma perspective on strong field multiphoton ionization. *Physical Review Letters*, 71(13):1994–1997, September 1993.
- [29] S. Ghimire, A. D. DiChiara, E. Sistrunk, P. Agostini, L. F. DiMauro, and D. A. Reis. Observation of high-order harmonic generation in a bulk crystal. *Nature Physics*, 7:138, December 2010.
- [30] M. Hohenleutner, F. Langer, O. Schubert, M. Knorr, U. Huttner, S. W. Koch, M. Kira, and R. Huber. Real-time observation of interfering crystal electrons in high-harmonic generation. *Nature*, 523:572, July 2015.
- [31] Ivan P. Christov, Margaret M. Murnane, and Henry C. Kapteyn. High-Harmonic Generation of Attosecond Pulses in the “Single-Cycle” Regime. *Physical Review Letters*, 78(7):1251–1254, February 1997.
- [32] P. M. Paul, E. S. Toma, P. Breger, G. Mullot, F. Augé, Ph. Balcou, H. G. Muller, and P. Agostini. Observation of a Train of Attosecond Pulses from High Harmonic Generation. *Science*, 292(5522):1689, June 2001.
- [33] P. B. Corkum and F. Krausz. Attosecond science. *Nature Physics*, 3:381, June 2007.
- [34] F. Krausz and M. Ivanov. Attosecond physics. *RMP*, 81(1):163–234, February 2009.
- [35] M. Hentschel, R. Kienberger, Ch. Spielmann, G. A. Reider, N. Milosevic, T. Brabec, P. Corkum, U. Heinzmann, M. Drescher, and F. Krausz. Attosecond metrology. *Nature*, 414(6863):509–513, November 2001.
- [36] E. A. Nanni, W. R. Huang, K. Hong, K. Ravi, A. Fallahi, G. Moriena, R. J. Dwayne Miller, and F. Kärtner. Terahertz-driven linear electron acceleration. *Nature Communications*, 6:8486, October 2015.
- [37] D. Woodbury, L. Feder, V. Shumakova, C. Gollner, R. Schwartz, B. Miao, F. Salehi, A. Korolov, A. Pugžlys, A. Baltuška, and H. M. Milchberg. Laser wakefield acceleration with mid-IR laser pulses. *Optics Letters*, 43(5):1131–1134, March 2018.

-
- [38] D. Ehberger, C. Kealhofer, and P. Baum. Electron energy analysis by phase-space shaping with THz field cycles. *Structural dynamics (Melville, N.Y.)*, 5(30221179):044303–044303, August 2018.
- [39] D. Ehberger, A. Ryabov, and P. Baum. Tilted electron pulses. *Physics Review Letters*, 121(9):094801, August 2018.
- [40] Y. Morimoto and P. Baum. Attosecond control of electron beams at dielectric and absorbing membranes. *Physical Review A*, 97(3):033815, March 2018.
- [41] A. H. Zewail. Four-Dimensional electron microscopy. *Science*, 328(5975):187, April 2010.
- [42] A. H. Zewail. 4d ultrafast electron diffraction, crystallography, and microscopy. *Annual Review of Physical Chemistry*, 57(1):65–103, July 2006.
- [43] M. Aidelsburger, F. O. Kirchner, F. Krausz, and P. Baum. Single-electron pulses for ultrafast diffraction. *Proceedings of the National Academy of Sciences of the United States of America*, 107(46):19714, November 2010.
- [44] L. Kasmi, D. Kreier, M. Bradler, E. Riedle, and P. Baum. Femtosecond single-electron pulses generated by two-photon photoemission close to the work function. *New Journal of Physics*, 17(3):033008, March 2015.
- [45] C. Kealhofer, W. Schneider, D. Ehberger, A. Ryabov, F. Krausz, and P. Baum. All-optical control and metrology of electron pulses. *Science*, 352(6284):429, April 2016.
- [46] Y. Morimoto and P. Baum. Diffraction and microscopy with attosecond electron pulse trains. *Nature Physics*, 14(3):252–256, March 2018.
- [47] D. Ehberger, K. J. Mohler, T. Vasileiadis, R. Ernstorfer, L. Waldecker, and P. Baum. Terahertz Compression of Electron Pulses at a Planar Mirror Membrane. *Physical Review Applied*, 11(2):024034, February 2019.
- [48] P. Baum and F. Krausz. Capturing atomic-scale carrier dynamics with electrons. *Chemical Physics Letters*, 683:57–61, September 2017.

-
- [49] M. Kozák, J. McNeur, K. J. Leedle, H. Deng, N. Schönenberger, A. Ruehl, I. Hartl, J. S. Harris, R. L. Byer, and P. Hommelhoff. Optical gating and streaking of free electrons with sub-optical cycle precision. *Nature Communications*, 8:14342, January 2017.
- [50] K. E. Priebe, C. Rathje, S. V. Yalunin, T. Hohage, A. Feist, S. Schäfer, and C. Ropers. Attosecond electron pulse trains and quantum state reconstruction in ultrafast transmission electron microscopy. *Nature Photonics*, 11(12):793–797, December 2017.
- [51] M. Kozák, N. Schönenberger, and P. Hommelhoff. Ponderomotive generation and detection of attosecond free-electron pulse trains. *Physical Review Letters*, 120(10):103203, March 2018.
- [52] H. Pires, M. Baudisch, D. Sanchez, M. Hemmer, and J. Biegert. Ultrashort pulse generation in the mid-IR. *Progress in Quantum Electronics*, 43:1–30, September 2015.
- [53] P. B. Corkum. High-power, subpicosecond 10- μ m pulse generation. *Optics Letters*, 8(10):514–516, October 1983.
- [54] P. Corkum. Amplification of picosecond 10 μ m pulses in multiatmosphere CO₂ lasers. *IEEE Journal of Quantum Electronics*, 21(3):216–232, 1985.
- [55] J. Faist, F. Capasso, D. L. Sivco, C. Sirtori, A. L. Hutchinson, and A. Y. Cho. Quantum cascade laser. *Science*, 264(5158):553, April 1994.
- [56] Yargo Bonetti and Jérôme Faist. Entering the mid-infrared. *Nature Photonics*, 3:32, January 2009.
- [57] Y. Yao, A. J. Hoffman, and C. F. Gmachl. Mid-infrared quantum cascade lasers. *Nature Photonics*, 6:432, June 2012.
- [58] D. Oepf, A. F. G. van der Meer, and P. W. van Amersfoort. The free-electron-laser user facility FELIX. *Infrared Physics & Technology*, 36(1):297–308, January 1995.

- [59] T. Kawasaki, T. Yaji, T. Ohta, and K. Tsukiyama. Application of mid-infrared free-electron laser tuned to amide bands for dissociation of aggregate structure of protein. *Journal of Synchrotron Radiation*, 23(1):152–157, 2016.
- [60] J. Zhang, K. F. Mak, and O. Pronin. Kerr-lens mode-locked 2- μ m thin-disk lasers. *IEEE Journal of Selected Topics in Quantum Electronics*, 24(5):1–11, 2018.
- [61] J. Zhang, F. Schulze, K. F. Mak, V. Pervak, D. Bauer, D. Sutter, and O. Pronin. High-power, high-efficiency Tm:YAG and Ho:YAG thin-disk lasers. *Laser & Photonics Reviews*, 12(3):1700273, 2018.
- [62] NoSoung Myoung, Dmitri V. Martyshkin, Vladimir V. Fedorov, and Sergey B. Mirov. Energy scaling of 4.3 μ m room temperature Fe:ZnSe laser. *Optics Letters*, 36(1):94–96, January 2011.
- [63] N. Nagl, K. F. Mak, Q. Wang, V. Pervak, F. Krausz, and O. Pronin. Efficient femtosecond mid-infrared generation based on a Cr:ZnS oscillator and step-index fluoride fibers. *Optics Letters*, 44(10):2390–2393, May 2019.
- [64] A. Ryabov and P. Baum. Electron microscopy of electromagnetic waveforms. *Science*, 353(6297):374, July 2016.
- [65] B.-H. Chen, M. Kretschmar, D. Ehberger, A. Blumenstein, P. Simon, P. Baum, and T. Nagy. Compression of picosecond pulses from a thin-disk laser to 30 fs at 4W average power. *Optics Express*, 26(4):3861–3869, February 2018.
- [66] B.-H. Chen, T. Nagy, and P. Baum. Efficient middle-infrared generation in LiGaS₂ by simultaneous spectral broadening and difference-frequency generation. *Optics Letters*, 43(12):2876–2876, June 2018.
- [67] B.-H. Chen, E. Wittmann, Y. Morimoto, P. Baum, and E. Riedle. Octave-spanning single-cycle middle-infrared generation through optical parametric amplification in LiGaS₂. *Optics Express*, 27(15):21306–21318, July 2019.
- [68] B.-H. Chen, C. Hofer, I. Pupeza, and P. Baum. Second-harmonic generation and self-phase modulation of few-cycle mid-infrared pulses. *Optics Letters*, 44(16):4079–4082, August 2019.

- [69] M. Rini, R. Tobey, N. Dean, J. Itatani, Y. Tomioka, Y. Tokura, R. W. Schoenlein, and A. Cavalleri. Control of the electronic phase of a manganite by mode-selective vibrational excitation. *Nature*, 449:72, September 2007.
- [70] W. Hu, S. Kaiser, D. Nicoletti, C. R. Hunt, I. Gierz, M. C. Hoffmann, M. Le Tacon, T. Loew, B. Keimer, and A. Cavalleri. Optically enhanced coherent transport in $\text{YBa}_2\text{Cu}_3\text{O}_{6.5}$ by ultrafast redistribution of interlayer coupling. *Nature Materials*, 13:705, May 2014.
- [71] S. Kaiser, C. R. Hunt, D. Nicoletti, W. Hu, I. Gierz, H. Y. Liu, M. Le Tacon, T. Loew, D. Haug, B. Keimer, and A. Cavalleri. Optically induced coherent transport far above T_c in underdoped $\text{YBa}_2\text{Cu}_3\text{O}_{6+\delta}$. *Physical Review A*, 89(18):184516, May 2014.
- [72] A. Gliserin, A. Apolonski, F. Krausz, and P. Baum. Compression of single-electron pulses with a microwave cavity. *New Journal of Physics*, 14(7):073055, July 2012.
- [73] A. Gliserin, M. Walbran, F. Krausz, and P. Baum. Sub-phonon-period compression of electron pulses for atomic diffraction. *Nature Communications*, 6:8723, October 2015.
- [74] M. Walbran, A. Gliserin, K. Jung, J. Kim, and P. Baum. 5-femtosecond laser-electron synchronization for pump-probe crystallography and diffraction. *Physical Review Applied*, 4(4):044013, October 2015.
- [75] P. A. Franken, A. E. Hill, C. W. Peters, and G. Weinreich. Generation of optical harmonics. *Physical Review Letters*, 7(4):118–119, August 1961.
- [76] Robert W. Boyd. *Nonlinear Optics, Third Edition*. Academic Press, Inc., 2008.
- [77] A. Baltuška, T. Fuji, and T. Kobayashi. Controlling the carrier-envelope phase of ultrashort light pulses with optical parametric amplifiers. *Physical Review Letters*, 88(13):133901, March 2002.
- [78] K. Kaneshima, N. Ishii, K. Takeuchi, and J. Itatani. Generation of carrier-envelope phase-stable mid-infrared pulses via dual-wavelength optical parametric amplification. *Optics Express*, 24(8):8660–8665, April 2016.

- [79] I. Pupeza, D. Sánchez, J. Zhang, N. Lilienfein, M. Seidel, N. Karpowicz, T. Paasch-Colberg, I. Znakovskaya, M. Pescher, W. Schweinberger, V. Pervak, E. Fill, O. Pronin, Z. Wei, F. Krausz, A. Apolonski, and J. Biegert. High-power sub-two-cycle mid-infrared pulses at 100MHz repetition rate. *Nature Photonics*, 9:721, September 2015.
- [80] T. P. Butler, D. Gerz, C. Hofer, J. Xu, C. Gaida, T. Heuermann, M. Gebhardt, L. Vamos, W. Schweinberger, J. A. Gessner, T. Siefke, M. Heusinger, U. Zeitner, A. Apolonski, N. Karpowicz, J. Limpert, F. Krausz, and I. Pupeza. Watt-scale 50-MHz source of single-cycle waveform-stable pulses in the molecular fingerprint region. *Optics Letters*, 44(7):1730–1733, April 2019.
- [81] I. N. Ross, P. Matousek, G. H. C. New, and K. Osvay. Analysis and optimization of optical parametric chirped pulse amplification. *Journal of the Optical Society of America B*, 19(12):2945–2956, December 2002.
- [82] A. Rogalski. HgCdTe infrared detector material: history, status and outlook. *Reports on Progress in Physics*, 68(10):2267–2336, August 2005.
- [83] M. J. E. Golay. A pneumatic infra-red detector. *Review of Scientific Instruments*, 18(5):357–362, August 1947.
- [84] D. Klocke, A. Schmitz, H. Soltner, H. Bousack, and H. Schmitz. Infrared receptors in pyrophilous (“fire loving”) insects as model for new un-cooled infrared sensors. *Beilstein Journal of Nanotechnology*, 2:186–197, 2011.
- [85] S. B. Lang. Pyroelectricity: From ancient curiosity to modern imaging tool. *Physics Today*, 58(8):31–36, August 2005.
- [86] M. Knorr, P. Steinleitner, J. Raab, I. Gronwald, P. Merkl, C. Lange, and R. Huber. Ultrabroadband etalon-free detection of infrared transients by van-der-Waals contacted sub-10- μ m gase detectors. *Optics Express*, 26(15):19059–19066, July 2018.
- [87] Q. Wu and X.-C. Zhang. Free-space electro-optic sampling of terahertz beams. *Applied Physics Letters*, 67(24):3523–3525, August 2019.

- [88] H. T. Lin, Z. Q. Luo, T. Gu, L. C. Kimerling, K. Wada, A. Agarwal, and J. J. Hu. Mid-infrared integrated photonics on silicon: a perspective. *Nanophotonics*, 7(2):393–420, February 2018.
- [89] F. Habel and V. Pervak. Dispersive mirror for the mid-infrared spectral range of 9–11.5 μ m. *Applied Optics*, 56(4):C71–C74, February 2017.
- [90] J. Bühler, J. Allerbeck, G. Fitzky, D. Brida, and A. Leitenstorfer. Terahertz shock-waves generated by a precise subcycle cut of the electric field. *Optica*, 5(7):821–824, July 2018.
- [91] A. A. Lanin, A. A. Voronin, E. A. Stepanov, A. B. Fedotov, and A. M. Zheltikov. Frequency-tunable sub-two-cycle 60-MW-peak-power free-space waveforms in the mid-infrared. *Optics Letters*, 39(22):6430–6433, November 2014.
- [92] S. Dai, Y. Wang, X. Peng, P. Zhang, X. Wang, and Y. Xu. A review of mid-infrared supercontinuum generation in Chalcogenide glass fibers, 2018.
- [93] K. Reimann, R. P. Smith, A. M. Weiner, T. Elsaesser, and M. Woerner. Direct field-resolved detection of terahertz transients with amplitudes of megavolts per centimeter. *Optics Letters*, 28(6):471–473, March 2003.
- [94] F. Junginger, A. Sell, O. Schubert, B. Mayer, D. Brida, M. Marangoni, G. Cerullo, A. Leitenstorfer, and R. Huber. Single-cycle multiterahertz transients with peak fields above 10 MV/cm. *optics Letters*, 35(15):2645–2647, August 2010.
- [95] M. Knorr, J. Raab, M. Tauer, P. Merkl, D. Peller, E. Wittmann, E. Riedle, C. Lange, and R. Huber. Phase-locked multi-terahertz electric fields exceeding 13 MV/cm at a 190 kHz repetition rate. *Optics Letters*, 42(21):4367–4370, November 2017.
- [96] Y. Nomura, H. Shirai, K. Ishii, N. Tsurumachi, A. A. Voronin, A. M. Zheltikov, and T. Fuji. Phase-stable sub-cycle mid-infrared conical emission from filamentation in gases. *Optics Express*, 20(22):24741–24747, October 2012.
- [97] E. A. Stepanov, A. A. Lanin, A. A. Voronin, A. B. Fedotov, and A. M. Zheltikov. Solid-state source of subcycle pulses in the midinfrared. *Physical Review Letter*, 117(4):043901, July 2016.

- [98] H. Liang, P. Krogen, Z. Wang, H. Park, T. Kroh, K. Zawilski, P. Schunemann, J. Moses, L. F. DiMauro, F. X. Kärtner, and K.-H. Hong. High-energy mid-infrared sub-cycle pulse synthesis from a parametric amplifier. *Nature Communications*, 8(1):141, July 2017.
- [99] C. Kübler, R. Huber, S. Tübel, and A. Leitenstorfer. Ultrabroadband detection of multi-terahertz field transients with GaSe electro-optic sensors: Approaching the near infrared. *Applied Physics Letters*, 85(16):3360–3362, October 2004.
- [100] A. Sell, A. Leitenstorfer, and R. Huber. Phase-locked generation and field-resolved detection of widely tunable terahertz pulses with amplitudes exceeding 100 MV/cm. *Optics Letters*, 33(23):2767–2769, December 2008.
- [101] G. Andriukaitis, T. Balčiūnas, S. Ališauskas, A. Pugžlys, A. Baltuška, T. Popmintchev, M. Chen, M. M. Murnane, and H. C. Kapteyn. 90 GW peak power few-cycle mid-infrared pulses from an optical parametric amplifier. *Optics Letters*, 36(15):2755–2757, August 2011.
- [102] B. Mayer, C. Schmidt, J. Bühler, D. V. Seletskiy, D. Brida, A. Pashkin, and A. Leitenstorfer. Sub-cycle slicing of phase-locked and intense mid-infrared transients. *New Journal of Physics*, 16(6):063033, June 2014.
- [103] C. R. Petersen, U. Møller, I. Kubat, B. Zhou, S. Dupont, J. Ramsay, T. Benson, S. Sujecki, N. Abdel-Moneim, Z. Tang, D. Furniss, A. Seddon, and O. Bang. Mid-infrared supercontinuum covering the 1.4-13.3 μ m molecular fingerprint region using ultra-high NA chalcogenide step-index fibre. *Nature Photonics*, 8:830, September 2014.
- [104] D. Sanchez, M. Hemmer, M. Baudisch, S. L. Cousin, K. Zawilski, P. Schunemann, O. Chalus, C. Simon-Boisson, and J. Biegert. 7 μ m, ultrafast, sub-millijoule-level mid-infrared optical parametric chirped pulse amplifier pumped at 2 μ m. *Optica*, 3(2):147–150, February 2016.
- [105] A. V. Mitrofanov, A. A. Voronin, D. A. Sidorov-Biryukov, S. I. Mitryukovsky, A. B. Fedotov, E. E. Serebryannikov, D. V. Meshchankin, V. Shumakova, S. Ališauskas, A. Pugžlys, V. Ya. Panchenko, A. Baltuška, and A. M. Zheltikov. Subterawatt few-cycle mid-infrared pulses from a single filament. *Optica*, 3(3):299–302, March 2016.

- [106] T. Morimoto, N. Sono, T. Miyamoto, N. Kida, and H. Okamoto. Generation of a carrier-envelope-phase-stable femtosecond pulse at 10 μm by direct down-conversion from a Ti:sapphire laser pulse. *Applied Physics Express*, 10(12):122701, November 2017.
- [107] U. Elu, M. Baudisch, H. Pires, F. Tani, M. H. Frosz, F. Köttig, A. Ermolov, P. St.J. Russell, and J. Biegert. High average power and single-cycle pulses from a mid-IR optical parametric chirped pulse amplifier. *Optica*, 4(9):1024–1029, September 2017.
- [108] Y. V. Aulin, A. Tuladhar, and E. Borguet. Ultrabroadband mid-infrared non-collinear difference frequency generation in a silver thiogallate crystal. *Optics Letters*, 43(18):4402–4405, September 2018.
- [109] J. Zhang, K. Mak, N. Nagl, M. Seidel, D. Bauer, D. Sutter, V. Pervak, F. Krausz, and O. Pronin. Multi-mw, few-cycle mid-infrared continuum spanning from 500 to 2250 cm^{-1} . *Light: Science & Applications*, 7:17180, February 2018.
- [110] O. Novák, P. R. Krogen, T. Kroh, T. Mocek, F. X. Kärtner, and K.-H. Hong. Femtosecond 8.5 μm source based on intrapulse difference-frequency generation of 2.1 μm pulses. *Optics Letters*, 43(6):1335–1338, March 2018.
- [111] M. Seidel, X. Xiao, S. A. Hussain, G. Arisholm, A. Hartung, K. T. Zawilski, P. G. Schunemann, F. Habel, M. Trubetskov, V. Pervak, O. Pronin, and F. Krausz. Multi-watt, multi-octave, mid-infrared femtosecond source. *Science Advances*, 4(4):eaq1526, April 2018.
- [112] S. B. Penwell, L. Whaley-Mayda, and A. Tokmakoff. Single-stage MHz mid-IR OPA using ligas_2 and a fiber laser pump source. *Optics Letters*, 43(6):1363–1366, March 2018.
- [113] N. Bigler, J. Pupeikis, S. Hrisafov, L. Gallmann, C. R. Phillips, and U. Keller. High-power OPCPA generating 1.7 cycle pulses at 2.5 μm . *Optics Express*, 26(20):26750–26757, October 2018.
- [114] P. Wang, Y. Li, W. Li, H. Su, B. Shao, S. Li, C. Wang, D. Wang, R. Zhao, Y. Peng, Y. Leng, R. Li, and Z. Xu. 2.6mJ/100Hz CEP-stable near-single-cycle

- 4 μm laser based on OPCPA and hollow-core fiber compression. *Optics Letters*, 43(9):2197–2200, May 2018.
- [115] Z. Nie, C.-H. Pai, J. Hua, C. Zhang, Y. Wu, Y. Wan, F. Li, J. Zhang, Z. Cheng, Q. Su, S. Liu, Y. Ma, X. Ning, Y. He, W. Lu, H.-H. Chu, J. Wang, W. B. Mori, and C. Joshi. Relativistic single-cycle tunable infrared pulses generated from a tailored plasma density structure. *Nature Photonics*, 12(8):489–494, August 2018.
- [116] Q. Wang, J. Zhang, A. Kessel, N. Nagl, V. Pervak, O. Pronin, and K. F. Mak. Broadband mid-infrared coverage (2–17 μm) with few-cycle pulses via cascaded parametric processes. *Optics Letters*, 44(10):2566–2569, May 2019.
- [117] C. Gaida, M. Gebhardt, T. Heuermann, F. Stutzki, C. Jauregui, J. Antonio-Lopez, A. Schülzgen, R. Amezcua-Correa, A. Tünnermann, I. Pupeza, and J. Limpert. Watt-scale super-octave mid-infrared intrapulse difference frequency generation. *Light: Science & Applications*, 7(1):94, November 2018.
- [118] J. Zhang, K. Fritsch, Q. Wang, F. Krausz, K. F. Mak, and O. Pronin. Intra-pulse difference-frequency generation of mid-infrared (2.7–20 μm) by random quasi-phase-matching. *Optics Letters*, 44(12):2986–2989, June 2019.
- [119] S. Vasilyev, I. S. Moskalev, V. O. Smolski, J. M. Peppers, M. Mirov, A. V. Muraviev, K. Zawilski, P. G. Schunemann, S. B. Mirov, K. L. Vodopyanov, and V. P. Gapontsev. Super-octave longwave mid-infrared coherent transients produced by optical rectification of few-cycle 2.5- μm pulses. *Optica*, 6(1):111–114, January 2019.
- [120] Kun Liu, Houkun Liang, Lifeng Wang, Shizhen Qu, Tino Lang, Hao Li, Qi Jie Wang, and Ying Zhang. Multimicrojoule GaSe-based midinfrared optical parametric amplifier with an ultrabroad idler spectrum covering 4.2–16 μm . *Optics Letters*, 44(4):1003–1006, February 2019.
- [121] S. Qu, H. Liang, K. Liu, X. Zou, W. Li, Q. J. Wang, and Y. Zhang. 9 μm few-cycle optical parametric chirped-pulse amplifier based on LiGaS₂. *Optics Letters*, 44(10):2422–2425, May 2019.
- [122] M. V. Tsarev, D. Ehberger, and P. Baum. High-average-power, intense THz pulses from a LiNbO₃ slab with silicon output coupler. *Applied Physics B*, 122(2):30, January 2016.

- [123] K. Fritsch, M. Poetzlberger, V. Pervak, J. Brons, and O. Pronin. All-solid-state multipass spectral broadening to sub-20fs. *Optics Letters*, 43(19):4643–4646, October 2018.
- [124] S. Hädrich, A. Klenke, A. Hoffmann, T. Eidam, T. Gottschall, J. Rothhardt, J. Limpert, and A. Tünnermann. Nonlinear compression to sub-30-fs, 0.5 mJ pulses at 135 W of average power. *Optics Letters*, 38(19):3866–3869, October 2013.
- [125] C. P. Hauri, W. Kornelis, F. W. Helbing, A. Heinrich, A. Couairon, A. Mysyrowicz, J. Biegert, and U. Keller. Generation of intense, carrier-envelope phase-locked few-cycle laser pulses through filamentation. *Applied Physics B*, 79(6):673–677, October 2004.
- [126] C.-H. Lu, Y.-J. Tsou, H.-Y. Chen, B.-H. Chen, Y.-C. Cheng, S.-D. Yang, M.-C. Chen, C.-C. Hsu, and A. H. Kung. Generation of intense supercontinuum in condensed media. *Optica*, 1(6):400–406, December 2014.
- [127] S. Hädrich, M. Kienel, M. Müller, A. Klenke, J. Rothhardt, R. Klas, T. Gottschall, T. Eidam, A. Drozdy, P. Jójárt, Z. Várallyay, E. Cormier, K. Osvay, A. Tünnermann, and J. Limpert. Energetic sub-2-cycle laser with 216W average power. *Optics Letters*, 41(18):4332–4335, September 2016.
- [128] A. Giesen, H. Hugel, A. Voss, K. Wittig, U. Brauch, and H. Opower. Scalable concept for diode-pumped high-power solid-state lasers. *Applied Physics B-lasers and Optics*, 58(5):365–372, May 1994.
- [129] J.-P. Negel, A. Voss, M. A. Ahmed, D. Bauer, D. Sutter, A. Killi, and T. Graf. 1.1kW average output power from a thin-disk multipass amplifier for ultrashort laser pulses. *Optics Letters*, 38(24):5442–5445, December 2013.
- [130] P. Russbueldt, T. Mans, G. Rotarius, J. Weitenberg, H. D. Hoffmann, and R. Poprawe. 400 W Yb:YAG Innoslab fs-amplifier. *Optics Express*, 17(15):12230–12245, July 2009.
- [131] P. Russbueldt, T. Mans, J. Weitenberg, H. D. Hoffmann, and R. Poprawe. Compact diode-pumped 1.1 kW Yb:YAG Innoslab femtosecond amplifier. *Optics Letters*, 35(24):4169–4171, December 2010.

- [132] T. Eidam, S. Hanf, E. Seise, T. V. Andersen, T. Gabler, C. Wirth, T. Schreiber, J. Limpert, and A. Tünnermann. Femtosecond fiber CPA system emitting 830 W average output power. *Optics Letters*, 35(2):94–96, January 2010.
- [133] S. Backus, . Kirchner, R. Lemons, D. Schmidt, C. Durfee, M. Murnane, and H. Kapteyn. Direct diode pumped Ti:sapphire ultrafast regenerative amplifier system. *Optics Express*, 25(4):3666–3674, February 2017.
- [134] J. Rothhardt, S. Hadrich, J. C. Delagnes, E. Cormier, and J. Limpert. High average power near-infrared few-cycle lasers. *Laser & Photonics Reviews*, 11(4):1700043, July 2017.
- [135] J. Rothhardt, S. Hädrich, H. Carstens, N. Herrick, S. Demmler, J. Limpert, and A. Tünnermann. 1 MHz repetition rate hollow fiber pulse compression to sub-100-fs duration at 100 W average power. *Optics Letters*, 36(23):4605–4607, December 2011.
- [136] J. Rothhardt, S. Hädrich, A. Klenke, S. Demmler, A. Hoffmann, T. Gotschall, T. Eidam, M. Krebs, J. Limpert, and A. Tünnermann. 53 w average power few-cycle fiber laser system generating soft x rays up to the water window. *Optics Letters*, 39(17):5224–5227, September 2014.
- [137] N. V. Didenko, A. V. Konyashchenko, P. V. Kostyukov, L. L. Losev, V. S. Pazyuk, S. Yu Tenyakov, and V. V. Bryukhanov. Temporal compression of pulses from a 100-KHz-repetition-rate femtosecond ytterbium laser. *Quantum Electronics*, 46(8):675–678, August 2016.
- [138] L. Lavenu, M. Natile, F. Guichard, Y. Zaouter, M. Hanna, E. Mottay, and P. Georges. High-energy few-cycle Yb-doped fiber amplifier source based on a single nonlinear compression stage. *Optics Express*, 25(7):7530–7537, April 2017.
- [139] K. F. Mak, M. Seidel, O. Pronin, M. H. Frosz, A. Abdolvand, V. Pervak, A. Apolonski, F. Krausz, J. C. Travers, and P. St. J. Russell. Compressing μ j-level pulses from 250 fs to sub-10 fs at 38-MHz repetition rate using two gas-filled hollow-core photonic crystal fiber stages. *Optics Letters*, 40(7):1238–1241, April 2015.

- [140] T. Nagy, M. Forster, and P. Simon. Flexible hollow fiber for pulse compressors. *Applied Optics*, 47(18):3264–3268, June 2008.
- [141] T. Nagy, V. Pervak, and P. Simon. Optimal pulse compression in long hollow fibers. *Optics Letters*, 36(22):4422–4424, November 2011.
- [142] M. Bradler, C. Homann, and E. Riedle. Broadband difference frequency mixing between visible and near-infrared pulses for few-cycle pulse generation with stable carrier-envelope phase. *Applied Physics B-lasers and Optics*, 113(1):19–25, October 2013.
- [143] V. S. Yakovlev, M. I. Stockman, F. Krausz, and P. Baum. Atomic-scale diffractive imaging of sub-cycle electron dynamics in condensed matter. *Scientific Reports*, 5:14581, September 2015.
- [144] W. Schneider, A. Ryabov, Cs. Lombosi, T. Metzger, Zs. Major, J. A. Fülöp, and P. Baum. 800-fs, 330- μ J pulses from a 100-W regenerative Yb:YAG thin-disk amplifier at 300 kHz and THz generation in LiNbO₃. *Optics Letters*, 39(23):6604–6607, December 2014.
- [145] B. Schenkel, J. Biegert, U. Keller, C. Vozzi, M. Nisoli, G. Sansone, S. Stagira, S. De Silvestri, and O. Svelto. Generation of 3.8-fs pulses from adaptive compression of a cascaded hollow fiber supercontinuum. *Optics Letters*, 28(20):1987–1989, October 2003.
- [146] R. DeSalvo, D. J. Hagan, M. Sheik-Bahae, G. Stegeman, E. W. Van Stryland, and H. Vanherzeele. Self-focusing and self-defocusing by cascaded second-order effects in KTP. *Optics Letters*, 17(1):28–30, January 1992.
- [147] X. Liu, L. Qian, and F. Wise. High-energy pulse compression by use of negative phase shifts produced by the cascade $\chi^{(2)}:\chi^{(2)}$ nonlinearity. *Optics Letters*, 24(23):1777–1779, December 1999.
- [148] V. Petrov. Parametric down-conversion devices: The coverage of the mid-infrared spectral range by solid-state laser sources. *Optical Materials*, 34(3):536–554, January 2012.
- [149] C. Y. Wang, T. Herr, P. Del’Haye, A. Schliesser, J. Hofer, R. Holzwarth, T. W. Hänsch, N. Picqué, and T. J. Kippenberg. Mid-infrared optical frequency combs

- at 2.5 μ m based on crystalline microresonators. *Nature Communications*, 4:1345, January 2013.
- [150] O. Schubert, M. Hohenleutner, F. Langer, B. Urbanek, C. Lange, U. Huttner, D. Golde, T. Meier, M. Kira, S. W. Koch, and R. Huber. Sub-cycle control of terahertz high-harmonic generation by dynamical Bloch oscillations. *Nature Photonics*, 8(2):119–123, February 2014.
- [151] M. Seidel, J. Brons, G. Arisholm, K. Fritsch, V. Pervak, and O. Pronin. Efficient high-power ultrashort pulse compression in self-defocusing bulk media. *Scientific Reports*, 7(1):1410, May 2017.
- [152] R. Šuminas, G. Tamošauskas, V. Jukna, A. Couairon, and A. Dubietis. Second-order cascading-assisted filamentation and controllable supercontinuum generation in birefringent crystals. *Optics Express*, 25(6):6746–6756, March 2017.
- [153] A. M. Weiner, J. P. Heritage, and R. H. Stolen. Self-phase modulation and optical pulse compression influenced by stimulated Raman scattering in fibers. *Journal of the Optical Society of America B.*, 5(2):364–372, February 1988.
- [154] Q. Z. Wang, Q. D. Liu, Disa Liu, P. P. Ho, and R. R. Alfano. High-resolution spectra of self-phase modulation in optical fibers. *Journal of the Optical Society of America B.*, 11(6):1084–1089, June 1994.
- [155] D.-P. Wei, T. V. Galstian, I. V. Smolnikov, V. G. Plotnichenko, and A. Zohrabyan. Spectral broadening of femtosecond pulses in a single-mode As-S glass fiber. *Optics Express*, 13(7):2439–2443, April 2005.
- [156] C. Manzoni, G. Cerullo, and S. De Silvestri. Ultrabroadband self-phase-stabilized pulses by difference-frequency generation. *Optics Letters*, 29(22):2668–2670, November 2004.
- [157] C. Homann, M. Bradler, M. Förster, P. Hommelhoff, and E. Riedle. Carrier-envelope phase stable sub-two-cycle pulses tunable around 1.8 μ m at 100 khz. *Optics Letters*, 37(10):1673–1675, May 2012.
- [158] H. Fattahi, A. Schwarz, S. Keiber, and N. Karpowicz. Efficient, octave-spanning difference-frequency generation using few-cycle pulses in simple collinear geometry. *Optics Letters*, 38(20):4216–4219, October 2013.

- [159] R. A. Kaindl, M. Wurm, K. Reimann, P. Hamm, A. M. Weiner, and M. Woerner. Generation, shaping, and characterization of intense femtosecond pulses tunable from 3 to 20 μm . *Journal of the Optical Society of America B*, 17(12):2086–2094, December 2000.
- [160] V. Petrov. Frequency down-conversion of solid-state laser sources to the mid-infrared spectral range using non-oxide nonlinear crystals. *Progress in Quantum Electronics*, 42:1–106, July 2015.
- [161] M. Bradler, J. C. Werhahn, D. Hutzler, S. Fuhrmann, R. Heider, E. Riedle, H. Iglev, and R. Kienberger. A novel setup for femtosecond pump-repump-probe IR spectroscopy with few cycle CEP stable pulses. *Optics Express*, 21(17):20145–20158, August 2013.
- [162] M. Bradler, C. Homann, and E. Riedle. Mid-IR femtosecond pulse generation on the microjoule level up to 5 μm at high repetition rates. *Optics Letters*, 36(21):4212–4214, November 2011.
- [163] M. Neuhaus, H. Fuest, M. Seeger, J. Schötz, M. Trubetskov, P. Russbuedt, H. D. Hoffmann, E. Riedle, Zs. Major, V. Pervak, M. F. Kling, and P. Wnuk. 10 W CEP-stable few-cycle source at 2 μm with 100 kHz repetition rate. *Optics Express*, 26(13):16074–16085, June 2018.
- [164] P. Baum, S. Lochbrunner, and E. Riedle. Generation of tunable 7-fs ultraviolet pulses: achromatic phase matching and chirp management. *Applied Physics B*, 79(8):1027–1032, December 2004.
- [165] M. Bradler, P. Baum, and E. Riedle. Femtosecond continuum generation in bulk laser host materials with sub- μJ pump pulses. *Applied Physics B*, 97(3):561, August 2009.
- [166] J. Piel, M. Beutter, and E. Riedle. 20-50-fs pulses tunable across the near infrared from a blue-pumped noncollinear parametric amplifier. *Optics Letters*, 25(3):180–182, February 2000.
- [167] I. Z. Kozma, P. Baum, S. Lochbrunner, and E. Riedle. Widely tunable sub-30 fs ultraviolet pulses by chirped sum frequency mixing. *Optics Express*, 11(23):3110–3115, November 2003.

- [168] E. Wittmann, M. Bradler, and E. Riedle. Direct generation of 7 fs whitelight pulses from bulk sapphire. In *19th International Conference on Ultrafast Phenomena*, OSA Technical Digest (online), page 07.Mon.P1.56, Okinawa, July 2014. Optical Society of America.
- [169] I. Z. Kozma, P. Baum, U. Schmidhammer, S. Lochbrunner, and E. Riedle. Compact autocorrelator for the online measurement of tunable 10 femtosecond pulses. *Review of Scientific Instruments*, 75(7):2323–2327, July 2004.
- [170] M. Porer, J.-M. Ménard, and R. Huber. Shot noise reduced terahertz detection via spectrally postfiltered electro-optic sampling. *Optics Letters*, 39(8):2435–2438, April 2014.
- [171] C. Schriever, S. Lochbrunner, E. Riedle, and D. J. Nesbitt. Ultrasensitive ultraviolet-visible 20 fs absorption spectroscopy of low vapor pressure molecules in the gas phase. *Review of Scientific Instruments*, 79(1):013107, January 2008.
- [172] C. Homann and E. Riedle. Direct measurement of the effective input noise power of an optical parametric amplifier. *Laser & Photonics Reviews*, 7(4):580–588, 2013.
- [173] A. von Hoegen, R. Mankowsky, M. Fechner, M. Först, and A. Cavalleri. Probing the interatomic potential of solids with strong-field nonlinear phononics. *Nature*, 555:79, February 2018.
- [174] F. Langer, M. Hohenleutner, C. P. Schmid, C. Poellmann, P. Nagler, T. Korn, C. Schüller, M. S. Sherwin, U. Huttner, J. T. Steiner, S. W. Koch, M. Kira, and R. Huber. Lightwave-driven quasiparticle collisions on a subcycle timescale. *Nature*, 533:225, May 2016.
- [175] M. Th. Hassan, T. T. Luu, A. Moulet, O. Raskazovskaya, P. Zhokhov, M. Garg, N. Karpowicz, A. M. Zheltikov, V. Pervak, F. Krausz, and E. Goulielmakis. Optical attosecond pulses and tracking the nonlinear response of bound electrons. *Nature*, 530:66, February 2016.
- [176] T. Popmintchev, M. Chen, D. Popmintchev, P. Arpin, S. Brown, S. Ališauskas, G. Andriukaitis, T. Balčiūnas, O. D. Mücke, A. Pugzlys, A. Baltuška, B. Shim,

- S. E. Schrauth, A. Gaeta, C. Hernández-García, L. Plaja, A. Becker, A. Jaron-Becker, M. M. Murnane, and H. C. Kapteyn. Bright coherent ultrahigh harmonics in the keV X-ray regime from mid-infrared femtosecond lasers. *Science*, 336(6086):1287, June 2012.
- [177] B. Bergues, D. E. Rivas, M. Weidman, A. A. Muschet, W. Helml, A. Guggenmos, V. Pervak, U. Kleineberg, G. Marcus, R. Kienberger, D. Charalambidis, P. Tzallas, H. Schröder, F. Krausz, and L. Veisz. Tabletop nonlinear optics in the 100-eV spectral region. *Optica*, 5(3):237–242, March 2018.
- [178] D. J. Wilson, A. M. Summers, S. Zigo, B. Davis, S.-J. Robotjazi, J. A. Powell, D. Rolles, A. Rudenko, and C. A. Trallero-Herrero. An intense, few-cycle source in the long-wave infrared. *Scientific Reports*, 9(1):6002, April 2019.
- [179] D. Zhang, A. Fallahi, M. Hemmer, X. Wu, M. Fakhari, Y. Hua, H. Cankaya, A.-L. Calendron, L. E. Zapata, N. H. Matlis, and F. X. Kärtner. Segmented terahertz electron accelerator and manipulator (STEAM). *Nature Photonics*, 12(6):336–342, June 2018.
- [180] P. Yousefi, N. Schönenberger, J. Mcneur, M. Kozák, U. Niedermayer, and P. Hommelhoff. Dielectric laser electron acceleration in a dual pillar grating with a distributed Bragg reflector. *Optics Letters*, 44(6):1520–1523, March 2019.
- [181] I. Pupeza, M. Hubert, W. Schweinberger, M. Trubetskov, S. A. Hussain, L. Vamos, O. Pronin, F. Habel, V. Pervak, N. Karpowicz, E. Fill, A. Apolonski, M. Zigman, A. M. Azzeer, and F. Krausz. Field-resolved spectroscopy in the molecular fingerprint region. In *2017 Conference on Lasers and Electro-Optics Europe & European Quantum Electronics Conference (CLEO/Europe-EQEC)*, pages 1–1, 2017.
- [182] A. S. Kowligy, H. Timmers, A. J. Lind, U. Elu, F. C. Cruz, P. G. Schunemann, J. Biegert, and S. A. Diddams. Infrared electric field sampled frequency comb spectroscopy. *Science Advances*, 5(6):eaaw8794, June 2019.
- [183] J. M. Auerhammer and E. R. Eliel. Frequency doubling of mid-infrared radiation in gallium selenide. *Optics Letters*, 21(11):773–775, June 1996.
- [184] P. B. Corkum, P. P. Ho, R. R. Alfano, and J. T. Manassah. Generation of infrared supercontinuum covering 3-14 μ m in dielectrics and semiconductors. *Optics Letters*, 10(12):624–626, December 1985.

- [185] J. J. Pigeon, S. Ya. Tochitsky, C. Gong, and C. Joshi. Supercontinuum generation from 2 to 20 μ m in GaAs pumped by picosecond CO₂ laser pulses. *Optics Letters*, 39(11):3246–3249, June 2014.
- [186] A. A. Lanin, A. A. Voronin, E. A. Stepanov, A. B. Fedotov, and A. M. Zheltikov. Multioctave, 3-18 μ m sub-two-cycle supercontinua from self-compressing, self-focusing soliton transients in a solid. *Optics Letters*, 40(6):974–977, March 2015.
- [187] K. L. Vodopyanov. Parametric generation of tunable infrared radiation in ZnGeP₂ and GaSe pumped at 3 μ m. *Journal of the Optical Society of America B*, 10(9):1723–1729, September 1993.
- [188] K. R. Allakhverdiev, M. Ö. Yetis, S. Özbek, T. K. Baykara, and E. Yu. Salaev. Effective nonlinear GaSe crystal. Optical properties and applications. *Laser Physics*, 19(5):1092–1104, May 2009.
- [189] J. Guo, J.-J. Xie, D.-J. Li, G.-L. Yang, F. Chen, C.-R. Wang, L.-M. Zhang, Y. M. Andreev, K. A. Kokh, G. V. Lanskii, and V. A. Svetlichnyi. Doped GaSe crystals for laser frequency conversion. *Light: Science & Applications*, 4:e362, December 2015.
- [190] Florian Habel, Michael Trubetskov, and Vladimir Pervak. Group delay dispersion measurements in the mid-infrared spectral range of 2-20 μ m. *Optics Express*, 24(15):16705–16710, July 2016.
- [191] N. B. Singh, D. R. Suhre, V. Balakrishna, M. Marable, R. Meyer, N. Fernelius, F. K. Hopkins, and D. Zelmon. Far-infrared conversion materials: Gallium selenide for far-infrared conversion applications. *Progress in Crystal Growth and Characterization of Materials*, 37(1):47–102, January 1998.
- [192] C. Schmidt, J. Bühler, B. Mayer, A. Pashkin, A. Leitenstorfer, and D. V. Seletskiy. Controlled polar asymmetry of few-cycle and intense mid-infrared pulses. *Journal of Optics*, 18(5):05LT01, April 2016.
- [193] H. W. Icenogle, Ben C. Platt, and William L. Wolfe. Refractive indexes and temperature coefficients of germanium and silicon. *Applied Optics*, 15(10):2348–2351, October 1976.

- [194] B. Tatian. Fitting refractive-index data with the Sellmeier dispersion formula. *Applied Optics*, 23(24):4477–4485, December 1984.
- [195] P. J. Collings. Simple measurement of the band-gap in silicon and germanium. *American Journal of Physics*, 48(3):197–199, 1980.
- [196] M. J. Baker, J. Trevisan, P. Bassan, R. Bhargava, H. J. Butler, K. M. Dorling, P. R. Fielden, S. W. Fogarty, N. J. Fullwood, K. A. Heys, C. Hughes, P. Lasch, P. L. Martin-Hirsch, B. Obinaju, G. D. Sockalingum, J. Sulé-Suso, R. J. Strong, M. J. Walsh, B. R. Wood, P. Gardner, and F. L. Martin. Using Fourier transform IR spectroscopy to analyze biological materials. *Nature Protocols*, 9:1771, July 2014.
- [197] G. J. Stein, P. D. Keathley, P. Krogen, H. K. Liang, J. P. Siqueira, C. L. Chang, C. J. Lai, K. H. Hong, G. M. Laurent, and F. X. Kartner. Water-window soft x-ray high-harmonic generation up to the nitrogen K-edge driven by a kHz, 2.1 μm OPCPA source. *Journal of Physics B-atomic Molecular and Optical Physics*, 49(15):155601, August 2016.
- [198] P. Hommelhoff, Y. Sortais, A. Aghajani-Talesh, and M. A. Kasevich. Field emission tip as a nanometer source of free electron femtosecond pulses. *Physical Review Letters*, 96(7):077401, February 2006.
- [199] M. Krüger, M. Schenk, and P. Hommelhoff. Attosecond control of electrons emitted from a nanoscale metal tip. *Nature*, 475:78, July 2011.
- [200] S. Li and R. R. Jones. High-energy electron emission from metallic nano-tips driven by intense single-cycle terahertz pulses. *Nature Communications*, 7:13405, November 2016.

Acknowledgements

One thing for sure about this work is that it could hardly be done without many people's help. So I would like to express my gratitude at this point.

First of all, I would like to thank Prof. Dr. Ferenc Krausz for providing me the opportunity to join him and his world-leading research group on many advanced scientific topics. It is really a pleasure to work with so many talented scientists from different fields, which makes these four years of stay a remarkable and unforgettable experience in my life. I would also like to thank Prof. Dr. Thomas Udem for offering to review this thesis and my works.

I think words would never be enough for me to express my gratitude to my immediate advisor Prof. Dr. Peter Baum. I was really lucky to be part of Peter's group. His enthusiasm toward science and fundamental physics seems to fill him with full energy, which I believe affects all the UED group members. Also, his incredible patience and careful guidance truly play an important role in my research as a PhD. I would also like to give Dr. Alexander Gliserin a big "thank you". Without his unselfish help, I might be still looking for a place to live in Munich. And without him being the "master of LabVIEW", many of my experiments and measurements will not be done.

Many Thanks to Dr. Dominik Ehberger, who helped me with almost all the administration things on my first day of arrival. Also, just three days afterward, he helped me get acquainted with the lab, and work with me on the fiber broadening experiment right away. Even at the last stage of my PhD, he is always there and ready to offer help with my thesis.

I thank Dr. Andrey Ryabov for helping me literally everything with the computer and I thank Dr. Maxim Tsarev for sharing his experience with THz generation and

helped me with the mid-infrared project. I would also like to thank Dr. Yuya Morimoto, who always has great ideas for the experiments and share the same contempt for German food. I am also grateful for all the other UED group members, and I am really pleased to work with you all: Kathrin Mohler, Sonja Tauchert, Johannes Thurner, Dr. Mikhail Volkov, David Nabben, Ann-Kathrin Raab and Eruthuparna Ramachandran.

I would like to thank Mr. Öhm and his workshop team for always providing us fast and yet high-quality mechanical pieces for all of our experiments, and also thank Dr. Volodymyr Pervak for always being able to produce optics with coatings that are commercially unavailable but are extremely helpful for the laser setup.

I would also like to thank my collaborators. I am glad to have the chance to work with Tamas Nagy, who supported me with all the fiber experiments and helped me solve all kinds of fiber-problems. I also want to thank Prof. Dr. Eberhard Riedle and Dr. Emanuel Wittmann for their design and sharing their experience and knowledge on building the NOPA system.

Last but not least, I want to thank my family, for always being there with me. It was a tough decision to make because it was my first time to go abroad all by myself, and I knew my mother would worry a lot. Thank you for supporting my decision and helping me throughout my PhD with no complaint. I love you all.

爸媽、老弟我愛你們。